UNIKASSEL
VERSITÄT
University of Kassel

INA
Institut für Nanostrukturtechnologie
und Analytik

Highly Sensitive Sensor Based On Intracavity Laser Absorption Spectroscopy By Means Of Relative Intensity Noise

Dissertation

Doctor in Natural Sciences (Dr. rer. nat.)

by

Mahmoud Mohamed Mahmoud Ahmad

Institute of Nanostructure Technologies and Analytics (INA)
Department of Electrical Engineering/Informatics
University of Kassel
Germany

Kassel, December 2010

Hoch empfindlicher Sensor Auf Basis der Intracavity Laser Absorption Spectroscopy mit Hilfe von Relative Intensity Noise

Dissertation

zur Erlangung des akademischen Grades eines
Doktors der Naturwissenschaften (Dr. rer. nat.)
Im Fachbereich Elektrotechnik / Informatik
Der Universität Kassel

Vorgelegt von
Mahmoud Mohamed Mahmoud Ahmad

Kassel, December 2010

Erklärung

Hiermit versichere ich, dass ich die vorliegenda Dissertation selbständig und ohne unerlaubte Hilfe angefertigt und andere als die in der Dissertation angegebenen Hilfsmittel nicht benutzt habe. Alle Stellen, die wörtlich oder sinngemäß aus veröffentlichten oder unveröffentlichten Schriften entnommen sind, habe ich als solche kenntlich gemacht. Kein Teil dieser Arbeit ist in einem anderen Promotions- oder Habilitationsverfahren verwendet worden.

M.Sc./ Mahmoud Mohamed Mahmoud Ahmad
Unterschrift/ Datum/

Betreuer (Supervisor): Prof. Dr. Hartmut Hillmer

Prüfungskommission(Board of Examiners):

1. Prof. Dr. Hartmut Hillmer (1. Gutachter)
2. Prof. Dr. Bernd Witzigmann (2. Gutachter)
3. Prof. Dr. Peter Lehmann (Beisitzer)
4. Prof. Dr. Axel Bangert (Beisitzer)

Tag der mündlichen Prüfungn (Day of oral examination): 20.12.2010

Abstract

This thesis concerns with the main aspects of medical trace molecules detection by means of intracavity laser absorption spectroscopy (ICLAS), namely with the requirements for highly sensitive, highly selective, low price, and compact size sensor.

A novel two modes semiconductor laser sensor is demonstrated. Its operation principle is based on the competition between these two modes. The sensor sensitivity is improved when the sample is placed inside the two modes laser cavity, and the competition between the two modes exists. The effects of the mode competition in ICLAS are discussed theoretically and experimentally.

The sensor selectivity is enhanced using external cavity diode laser (ECDL) configuration, where the tuning range only depends on the external cavity configuration.

In order to considerably reduce the sensor cost, relative intensity noise (RIN) is chosen for monitoring the intensity ratio of the two modes. RIN is found to be an excellent indicator for the two modes intensity ratio variations which strongly supports the sensor methodology. On the other hand, it has been found that, wavelength tuning has no effect on the RIN spectrum which is very beneficial for the proposed detection principle.

In order to use the sensor for medical applications, the absorption line of an anesthetic sample, propofol, is measured. Propofol has been dissolved in various solvents. RIN has been chosen to monitor the sensor response. From the measured spectra, the sensor sensitivity enhancement factor is found to be of the order of 10^3 times of the conventional laser spectroscopy.

Zusammenfassung

Diese Arbeit befasst sich mit dem Hauptaspekt der Detektion von medizinischen Spurenmolekülen mit Hilfe der *Intracavity Laser Absorption Spectroscopy* (ICLAS). Die Anforderungen an den Sensor sind hochempfindlich und hochselektiv zu sein, sowie ein geringer Preis und eine kompakte Größe. Ein neuer zweimodiger Dioden-Laser-Sensor wurde demonstriert. Die Konkurrenz zwischen den zwei Moden ist das Hauptziel des Detektionsprinzips. Die Empfindlichkeit des Sensors konnte verbessert werden, indem eine Probe in die Kavität des zweimodigen Lasers eingebracht wurde, und eine Konkurrenz zwischen den beiden Moden besteht. Dieser Effekt der Modenkonkurrenz wurde theoretisch und experimentell diskutiert. Die Selektivität des Sensors wurde durch die Benutzung der Konfiguration eines Dioden-Lasers mit einer externen Kavität (ECDL) erhöht, wobei der Abstimmbereich nur von der Konfiguration der externen Kavität abhängig ist. Um die Kosten des Sensors weiter zu reduzieren, wurde die relative Rauschintensität (RIN) für die Beobachtung des Intensitätsverhältnisses der beiden Moden gewählt. Dabei hat sich herausgestellt, dass das RIN ein hervorragender Indikator für die Variationen des Intensitätsverhältnisses der beiden Moden ist, die nachhaltig die Sensormethodik unterstützt. Wiederum wurde herausgefunden, dass die Wellenlängen-Abstimmung keinen Effekt auf das RIN Spektrum hat, welche sehr nützlich für das vorgeschlagene Detektionsprinzip ist. Um den Sensor für medizinische Anwendungen zu benutzen, wurde die Absorptionslinie des Betäubungsmittels Propofol gemessen. Propofol wurde in verschiedenen Lösungsmitteln gelöst. RIN wurde ausgewählt, um die Sensor *Response* zu überprüfen. Aus den gemessenen Spektren wurde für die Sensitivität des Sensors ein Vergrößerungsfaktor, der in der Größenordnung 10^3-mal größer ist als für konventionelle Laser Spektroskopie, gefunden.

Contents

Chapter 1

Introduction

The modern breath analysis started with the discovery made by Pauling in 1971 when he found that hundreds of volatile organic compounds (VOCs) are present in the normal human breath [1]. This discovery has regenerated much emphasis in research that focuses on sensing various molecules for noninvasive disease diagnostics. Generally, breath analysis can be classified into two types. The first is the analysis of breath metabolites after administration or injection of a drug. The second is the analysis of breath compounds produced endogenously due to a particular physiological status.

To date, some VOCs have been established as bio-markers for specific diseases. For instance, alkanes are present in the case of lung cancer and formaldehyde in the case of breast cancer [2]. Such knowledge suggests that breath analysis is useful for human diseases diagnosis and monitoring. However due to the low concentrations and large quantity of trace compounds in exhaled breath, breath analysis requires highly sensitive and highly selective sensor in order to identify and determine concentrations of specific bio-markers.

1.1 Breath Analysis Techniques

Breath analysis techniques are categorized to three major types. These techniques are mass spectroscopy based sensor, electrical sensor, and laser spectroscopy based sensor.

The primarily major mass spectroscopy based techniques employed for breath analysis are gas chromatography-mass spectroscopy (GC-MS) [3, 4, 5], proton transfer reaction-mass spectroscopy (PTR-MS)[6, 7], ion mobility-mass spectroscopy (IM-MS) [8, 9] and selected ion flow tube mass spectroscopy (SIFT-MS) [10, 11]. These techniques have detection sensitivity in the range of part per billion (ppb) to part per trillion (ppt) and can analyze multiple compounds simultaneously. However current mass spectroscopy based techniques require complicated procedures for sample collection and pre-concentration, also these techniques are still limited to laboratory research as well as they are expensive and bulky sensors .

Electrical sensors are inexpensive and smaller in comparison with MS-based techniques. However they have limited selectivity and they require frequent calibration [12, 13].

Laser spectroscopy based technique has begun to draw increasing attention during the last years since new lasers have made it possible to develop a portable sensor for on line monitoring and analysis of human breath with high accuracy.

Laser absorption spectroscopy operates on the principle that the amount of light absorbed by a sample is related to the concentration of the target species in the sample. Light of known intensity is directed through a gas sample cell and the amount of light transmitted through the sample cell is measured by a detector. This shows that the ability of a laser absorption spectroscopy based sensor to detect a specific concentration depends on the path length through the absorbing medium. Therefore the sensitivity of laser absorption spectroscopy is proportional to the effective absorption path length that account for the physical absorption path and its enhancement from multiple reflections inside the cell. Various approaches have been implemented in order to considerably increase the effective absorption path length [14, 15]. The basic principle of these approaches are described below.

- Cavity ring down spectroscopy (CRDS) obtains high sensitivity due to multipass of the optical absorption pass inside the external resonator [16, 17, 18]. However the finite reflectivity of the resonators's mirrors used in CRDS results in the loss of the laser intensity and increases the system noise.

- Photoacoustic absorption spectroscopy (PAS) differs from (CRDS) by using a microphone to sense acoustic waves lunched by the absorption of pulsed light. The sensitivity of PAS approach is limited by the microphone sensitivity, laser power, cell constant, and the absorption path length [19].

- Tunable diode laser absorption spectroscopy (TDLAS) is a technique combining the conventional absorption spectral method with advanced tunable diode laser. In TDLAS method a sample gas is contained in a gas cell and a detector records the transmitted laser intensity as the laser wavelength is repetitively scanned through the central frequency of the absorption line of the gas. The detection limit of TDLAS can be given in terms of the minimum absorbance, which is determined by the minimum detectable fractional change of the laser intensity. The minimum absorbance is in the range of $10^{-2} - 10^{-4}$. This detection limit is limited by the stability of the light source, the electronic noise of the detector, the path length, and the signal to noise ratio [20].

- One of the most established approaches for increasing the path length and thereby increasing the sensitivity of the sensor without changing the laser intensity is the intracavity laser absorption spectroscopy (ICLAS) method. ICLAS depends on placing the sample of interest inside the laser cavity. Transition of a weak absorber is amplified by the multiple pass and appear superimposed on the broad spectrum of the laser. The sensitivity of ICLAS is given in terms of the effective path length and it is reported in the range of 70.000 km with dye laser [21]. Diode lasers are also capable of ICLAS, but they exhibit a maximum effective path length of about 2.5 km. However diode lasers are much more cost effective compared to dye lasers and they enable implementation in compact commercial devices [22].

1.2 Sensor Requirements

The analysis of breath metabolites after administration or injection of an anesthetic drug is the main goal of the current project. The present thesis deals with the main aspects of medical trace molecules detection using two modes ICLAS,

namely with the requirements for highly sensitive, highly selective, low price, and compact size sensor.

- **Sensitivity:** The sensitivity of a sensor marks the smallest concentration of a sample under consideration that can be detected. Highly sensitive sensors require a well designed setup which depends on highly sensitive spectroscopic method. In order to achieve highly sensitive sensor, ICLAS is the best choice to satisfy this purpose, where the cell is placed inside the laser cavity which exhibit multi reflections and the transition of a weak absorption line will be amplified by the multiple pass, which appears superimposed in the output spectrum. In addition, the sensor sensitivity will be increased when mode competition between laser modes exists.

- **Selectivity:** In order to achieve a highly selective sensor which has a stable tuning range, an external cavity laser diode configuration with two fiber Bragg gratings (FBGs) has been implemented. The fiber Bragg gratings work as wavelength selective elements and the laser diode with anti reflection coating facets serves as a gain media. The tuning process has been achieved by stretching the fiber Bragg gratings using thermal and strain effects.

- **Cost:** In order to reduce the sensor price, relative intensity noise (RIN) based measurements have been chosen as an indicator for the two modes variations. RIN method depends on converting the optical signals to an electrical signals using a photodiode. In comparison with the optical based measurements which mostly require an expensive optical spectrum analyzer (OSA), RIN based measurements enable low cost sensor fabrication.

- **Compact size:** Portable sensors require the instrument to be extremely compact and can be miniaturized. Therefore, fiber based setup that consists of nanotechnology based devices, which allow to be miniaturized, has been chosen.

1.3 Thesis Outline

The structure of the thesis is as follows:

- **Chapter 1** is this chapter, which serves as an introduction to the scientific objectives of the current project.
- **Chapter 2** gives the reader an introduction about the basis of semiconductor diode laser. It concerns with the basic characteristic of the external cavity diode laser (ECDL) and its applications in the scope of laser absorption spectroscopy. Finally, the intensity noise characteristics of diode laser are introduced and followed by a brief discussion of mode partition noise and mode competition noise which takes places in the working principle.
- **Chapter 3** introduces theoretical discussion of the mode competition and its effects in ICLAS. In order to describe these effects, a simple analytical model introduced by [23] has been considered.
- **Chapter 4** demonstrates the two modes fiber based ICLAS setup. In the frame of the demonstration purpose, a short overview of the passive and the active components, which are used to implement the setup, have been introduced. Also an overview about the different development steps is given.
- **Chapter 5** introduces the experimental measurements of the two modes sensor by means of RIN. In this experimental study, there are two main objectives. The first objective is to study the RIN spectrum behavior with the variation of the two modes intensities. The second objective is to study the RIN spectrum behavior with the variation of the two modes wavelength differences or the modes positions.
- **Chapter 6** focus on the measurements of propofol. The two modes ICLAS sensor is used to measure the absorption line of propofol. RIN has been chosen to monitor the sensor response. Propofol has been dissolved in different solvents and in cells of various sizes. The sensitivity enhancement factor has been extracted and calculated from the measured spectrum.

- **Chapter 7** concludes the results of the present thesis and gives outlook for the future work.

Chapter 2

Basics of Semiconductor Diode Lasers

In this chapter the basis of a semiconductor diode laser are introduced. Therefore, the operation principle of the diode laser are discussed in detail. Also the basic characteristics of the diode laser such as threshold condition and the output power are explored. Meanwhile ECDL, whose configurations constitute the system output is introduced. Different configurations of ECDL are introduced and highlighted. Many of these configurations exhibit a feedback from external reflectors such as mirrors or gratings, so this urges us to discuss the feedback effects in ECDL in detail. One of the most important applications of the external cavity semiconductor diode laser are found in the scope of absorption spectroscopy. Thus fundamentals of the absorption spectroscopy are introduced and discussed. The discussion is followed by an overview of a highly sensitive absorption spectroscopic method namely ICLAS. The sensitivity of ICLAS method depends on different effects. Competition among the modes is one of these effects and it plays an important role in the sensor sensitivity. Obviously mode competition depends on the mode numbers, therefore influence of the mode numbers on ICLAS is introduced. Relative intensity noise (RIN) is chosen to indicate the sensor response. Therefore noise characteristics of diode laser are introduced. This introduction is followed by a brief discussion of mode partition noise and mode competition noise which takes places in the working principle.

2.1 Principle of Diode Laser Operation

The development of semiconductor laser diode traces its origins to the beginning of 1960s after other lasers invention. Since semiconductor diode laser was invented in 1961, it has been the most important of all lasers [24]. Semiconductor diode lasers have many well-known features: high reliability, miniature in size, lower power consumption, wide tuneability, high efficiency, and excellent direct modulation capability. Therefore they used in a wide variety of applications ranging from readout devices in compact disk players to transmitters in optical fiber communication system. In the following subsection the fundamentals of light absorption, spontaneous emission, and stimulated emission induced in a two-level system in a single atom or molecule with a monochromatic electromagnetic wave are introduced. The necessary conditions for laser operation in a semiconductor diode lasers are also highlighted.

2.1.1 Absorption, Spontaneous Emission, and Stimulated Emission

The stationary states of an electron in an atom or molecule has its own stable orbit, in which atom has a specific energy level as shown in Fig. 2.1. When an electron is excited from its stationary state to another, it emits photon. Using Bohr's principle, the radiation frequency is related to the energies of the orbits by;

$$\nu \equiv \frac{E_f - E_i}{h}, \tag{2.1}$$

where E_f, E_i are the energy levels of final and initial states in an atom or molecule respectively, and h is Planck's constant. When light interacts with an atom, there are three different types of electronic transitions. These transition processes are shown in Fig. 2.2.

- Fig. 2.2(a) shows the first type of these transitions and it is called "resonant absorption". If we assume an electron initially residing in the ground state with energy E_i, the atom stays in the ground state until light with frequency $\nu = \nu_0$ is applied, where ν_0 is the transition frequency between two energy levels. The resonant absorption process happens when there is a probability

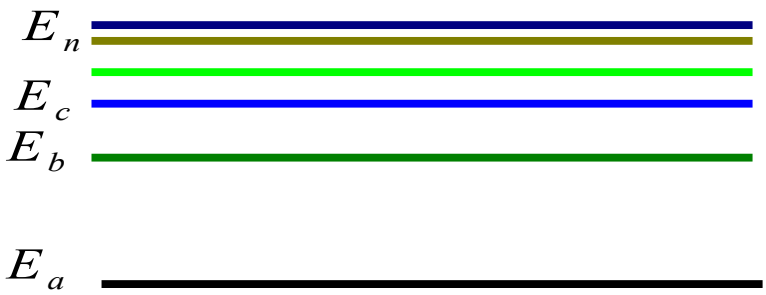

Figure 2.1: Energy levels diagram.

for an atom to make transition from lower E_i to the higher level E_f by absorption of a quanta of light.

- Fig. 2.2(b) illustrates the second type of the transition processes and it is referred as "spontaneous emission". When an electron absorbs light, it is excited to the higher energy level. The excited electron has a tendency to decay to the lower stable level with a definite lifetime in the final level, the corresponding energy difference E_f-E_i must be therefore released by spontaneously emitting a quanta of light. Light is emitted in all direction at an arbitrary phase, where electron makes independent transition. This incoherent emission is defined as spontaneous emission process.

- The third kind of transition processes is shown in Fig. 2.2(c). Now, assume that an electron is initially found in the final state and light with frequency $\nu = \nu_0$ is incident to the atom , the incident light will enforce the electron to undergo transition from the final state E_f to the initial state E_i. In such a way, a new photon is generated in addition to the incident photon, this phenomenon is called stimulated emission. The generated light has the same phase and direction as that of incident light, such stimulated light is known as coherent light.

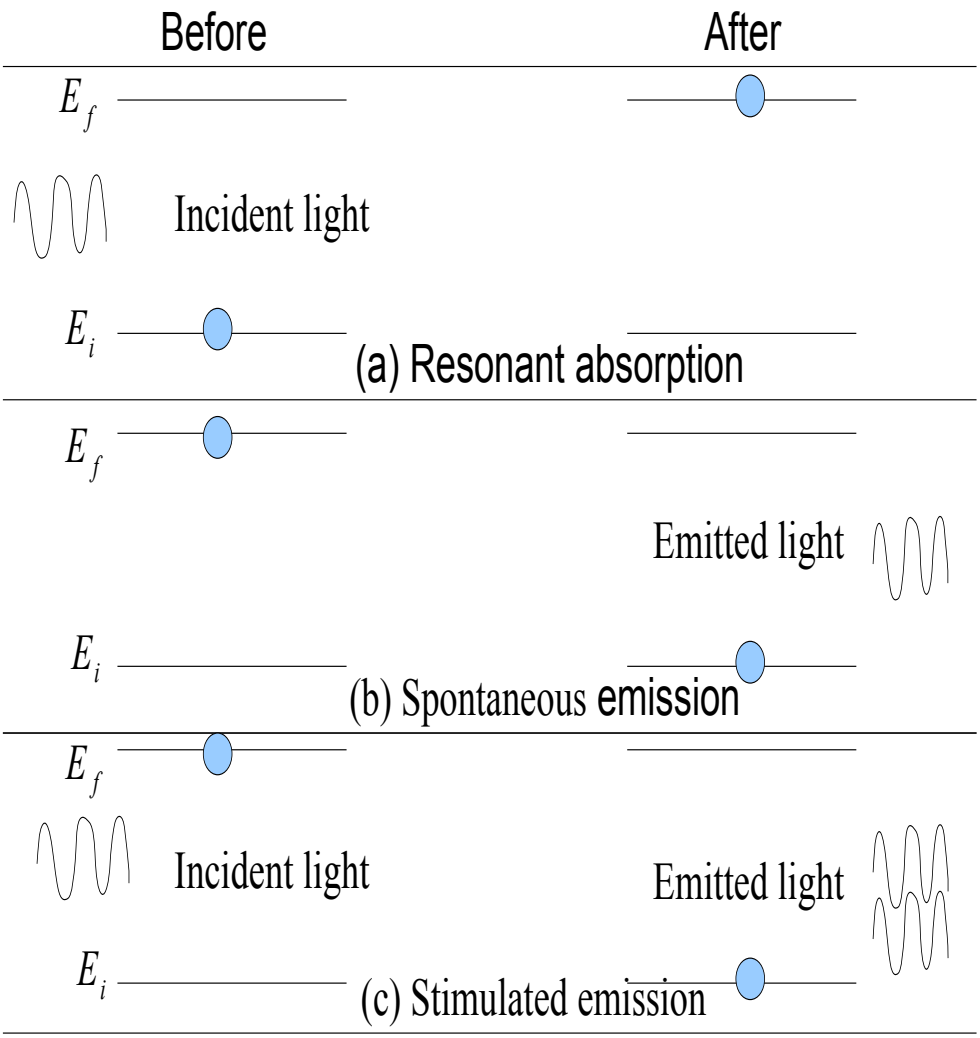

Figure 2.2: Three fundamental radiation processes associated with the interaction of light with an atom or molecule. (a) resonant absorption, (b) spontaneous emission, and (c) stimulated emission.

2.1.2 Lasing Conditions

To achieve lasing in a semiconductor diode laser, two conditions must be fulfilled.

1. There must be a population inversion, where the number of electrons in the excited states is higher than in the lower state. However usually the atom has more population in lower energy level than in the higher levels because population obeys Boltzmann thermal distribution law. Therefore, external pumping of atoms to higher states is required to accomplish population inversion.

2. The second important condition is that there must be more stimulated emissions than spontaneous ones in an active medium (sufficient condition for lasing). Therefore, an optical resonator must be used to feedback newly generated coherent light into the medium.

Therefore, the most important components in a laser are thus the active medium and the optical resonator [25].

2.2 Characteristics of Semiconductor Diode Lasers

This section deals with the threshold condition of Fabry-Perot diode laser and some elementary properties of diode laser characteristic such as threshold condition, output power and spectral contents.

2.2.1 Threshold Condition

The most important parameter for semiconductor diode laser is the threshold current. To emphasize the threshold condition, a Fabry-Perot diode laser is used and modeled as a resonator containing plane optical waves traveling back and forth along the length of the diode laser.

Fig. 2.3 shows a schematic diagram of a Fabry-Perot laser diode and the light propagation inside the laser cavity. Now, consider a semiconductor laser cavity of length d and a plane wave of complex propagation constant $k = \beta + j(g - \alpha)$, as shown in Fig. 2.3, where α is internal attenuation per unit length, β is propagation

coefficient, g is gain per unit length, that is produced by the stimulated effect, n is the refractive index of cavity material and λ is the wavelength of the wave in free-space.

The amplitude of the wave E_i is incident on the left hand side of the cavity, the ratio of transmitted light is t_1, the ratio of transmitted to incident light fields at the right is taken as t_2, the ratio of reflected to incident fields with the optical cavity is $r_1 e^{j\theta_1}$ at the left hand mirror and $r_2 e^{j\theta_2}$ at the right hand mirror.

For a low loss medium, phase shifts θ_1 and θ_2 are small and are generally neglected. The plane wave electric field independent of time is expressed as $E_i e^{-jkz}$. At the first transition boundary, the light field E_i which enters the cavity transmits the first mirror and the field just inside left boundary becomes $t_1 E_i$. The electrical field then proceeds the laser cavity, in which the wave is reflected

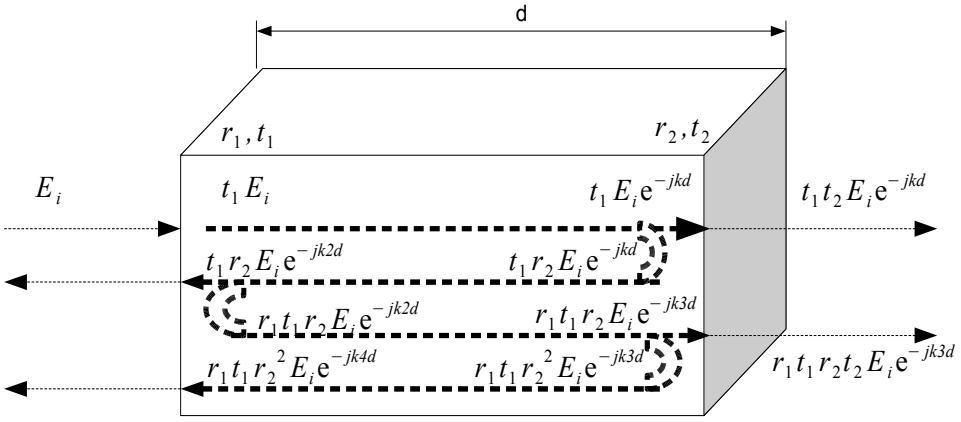

Figure 2.3: Schematic diagram of optical field propagation inside a Fabry-Perot diode laser cavity.

successively from one mirror to the other. The laser first arrives at the right boundary with filed $t_1 E_i e^{-jkd}$. The first portion of the field transmitted output at the right boundary is $t_1 t_2 E_i e^{-jkd}$, and a portion $t_1 r_2 E_i e^{-jkd}$ is reflected back into the cavity towards to the left boundary. The next portion of the transmitted light becomes $t_1 t_2 r_1 r_2 E_i e^{-3jkd}$ and so on. Adding up all the successive contributions,

the output E_o is given:

$$E_o = t_1 t_2 e^{-jkd}(1 + r_1 r_2 e^{-j2kd} + (r_1 r_2)2e^{-j4kd} + ...), \tag{2.2}$$

The sum is a geometric progression which permits Eq. 2.2 to be written as:

$$E_o = E_i[\frac{t_1 t_2 e^{-jkd}}{1 - r_1 r_2 e^{-j2kd}}]. \tag{2.3}$$

When the denominator of Eq. 2.3 tends to zero, the condition of a finite transmitted wave E_o with zero E_i is obtained, which is the conditions for oscillation. Therefore the oscillation condition is reached when

$$r_1 r_2 e^{-j2kd} = 1. \tag{2.4}$$

Then the resonance condition turns out to be

$$r_1 r_2 e^{-2jd\beta} e^{2d(g-\alpha)} = 1. \tag{2.5}$$

The condition for oscillation represents a wave making a round trip $2d$ inside the cavity to the starting plane with the same amplitude and phase, within an integer multiple of 2π, the general amplitude condition is:

$$r_1 r_2 e^{2(\Gamma g - \alpha)d} = 1, \tag{2.6}$$

where Γ is the confinement factor inside the cavity. Eq. 2.6 is generally written as

$$\Gamma g_{th} = \alpha + \frac{1}{2d} ln \frac{1}{r_1 r_2} = \alpha + \alpha_m. \tag{2.7}$$

This is the condition for threshold, where α_m is mirror loss. The gain coefficient per unit length strongly depends on the emission energy, the operation conditions, and light intensity in an active layer. If one replaces the r_1 and r_2 with power reflectivities R_1 and R_2, respectively. Eq. 2.7 can be rewritten as

$$\Gamma g_{th} = \alpha + \frac{1}{2d} ln \frac{1}{\sqrt{R_1 R_2}}. \tag{2.8}$$

From Eq. 2.5, the phase condition is found to be:

$$2d\beta = 2q\pi, \tag{2.9}$$

which satisfies

$$q = 2nd/\lambda, \tag{2.10}$$

where q is an integer, a resonance occurs when an integer number of half wavelength λ fits into the cavity.

2.2.2 Output Power

Another important parameter characterize the laser diode is the output power. Fig. 2.4 shows a typical plot of output power versus injection current (L-I curve)

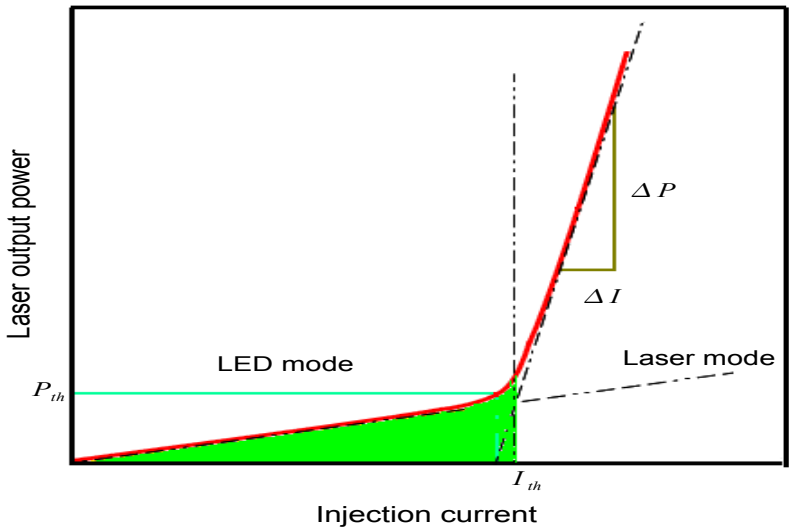

Figure 2.4: Typical plot of output power versus injection current (L-I curve) of cw laser diode.

of cw laser diode. When the forward bias current is low, the laser diode operates like a light-emitting diodes (LEDs) where the carrier density in the active layer is not high enough for population inversion, and spontaneous emission process is dominated in this region. As the bias current increases, population inversion occurs, and thus stimulated emission becomes dominant at a certain bias current. The current at this point is called threshold current. The injection current above the threshold induces the abrupt onset of laser action and coherent light is emitted.

The laser threshold current is evaluated by extrapolating the linear part of the characteristic to zero output power. The slope of the increase in the lasing region is proportional to the differential external quantum efficiency. Lasing occurs for all modes that satisfy Eq. 2.10. The longitudinal mode separation is given by

differentiating Eq. 2.10. Thus

$$\Delta\lambda_q = -\frac{\lambda^2}{2n_{eff}d}, \tag{2.11}$$

where n_{eff} is an effective refractive index. The optical power emitted by stimulated emission inside the cavity is:

$$P_{in} = \eta_{in}\frac{h\nu}{e}(I - I_{th}) \tag{2.12}$$

where η_{in} is the internal quantum efficiency, $h\nu$ is a photon energy, e is the electron charge and I_{th} is threshold injection current. The output power emitted from each end mirror of the laser cavity is written as:

$$P_{out} = \eta_{in}\frac{h\nu}{e}(I - I_{th})\frac{\alpha_m}{\alpha_{tot}} \tag{2.13}$$

where $\alpha_{tot} = \alpha + \alpha_m$ is the total loss of the laser.

2.3 External Cavity Diode Lasers

The tuning of the semiconductor diode laser output to one or more specific wavelengths with a variety of spectral characteristics is required for many applications such as high resolution spectroscopy and wide bandwidth communication networks [26].

In order to achieve a single frequency operation, a special wavelength selection mechanism has to be implement into the laser diode. Such mechanism may be either based on exploiting a wavelength selective loss which would be lowest for the selected wavelength or some kind of frequency selective elements.

Distributed feedback (DFB) lasers, distributed Bragg reflector (DBR) lasers as well as vertical cavity surface emitting lasers (VCSEL), represent an example of this group of lasers. Such lasers can be tuned over only a limited spectral range by changing temperature or the current of the laser diode.

The tuning range may also have gaps in it. Specially, tuning range of the VCSELs is limited by built-in wavelength resonant structures. The easiest way to obtain a really widely-tunable laser is to make a DFB array, however a trade-off between the tuning range and output power is occurred. This trade-off results

due to the increasing losses in the coupler as the number of lasers is increased [27].

Other monolithic solutions like a grating assisted co-directional coupler with rear sampled grating reflector (GCSR) have been demonstrated and implemented [28]. But they suffer from complicated tuning mechanism which requires the control of three or more currents.

However, the laser system can also be forced to operate in a single longitudinal mode by placing the diode laser in an external resonant cavity including a wavelength selector. Through insertion of the wavelength selective elements in the system, the external cavity configuration permits operation in a single mode with a line-width which is considerably less than that of a solitary laser diode. Moreover, selection and tuneability of the emitted wavelength by external control can be executed without the complications associated with variation of the temperature or pumping level of the laser diode.

The purpose of this subsection is to summarize some topics related to the semiconductor lasers that use a waveguide resonant cavity extended beyond the solitary laser diode. Such laser systems are called "external cavity lasers" or sometimes "extended cavity lasers" depending on elusive differences in the structure and operation. Fig. 2.5 shows schematic diagrams of different known configurations of the ECDLs. Fig. 2.5(a) shows a simple elementary external cavity laser. It consists of a semiconductor optical amplifier (SOA), a lens, and a reflector. The output from the SOA is collimated and redirected backwards. The SOA function usually performs a diode laser chip in which the rear and front facets have been coated with high and very low reflectivity films, respectively. The intracavity lens is a critical element in the cavity design. In order to collect most of the divergent light emitted from the SOA, large aperture lens is required. The reflector should provide optical feedback to satisfy lasing condition in the cavity. Changing position of the reflector will perturb the frequency and spectrum of the emission. In general, reflectivity of the reflector must be wavelength dependent to enforce single frequency operation of the system. It may be termed as "a wavelength selector".

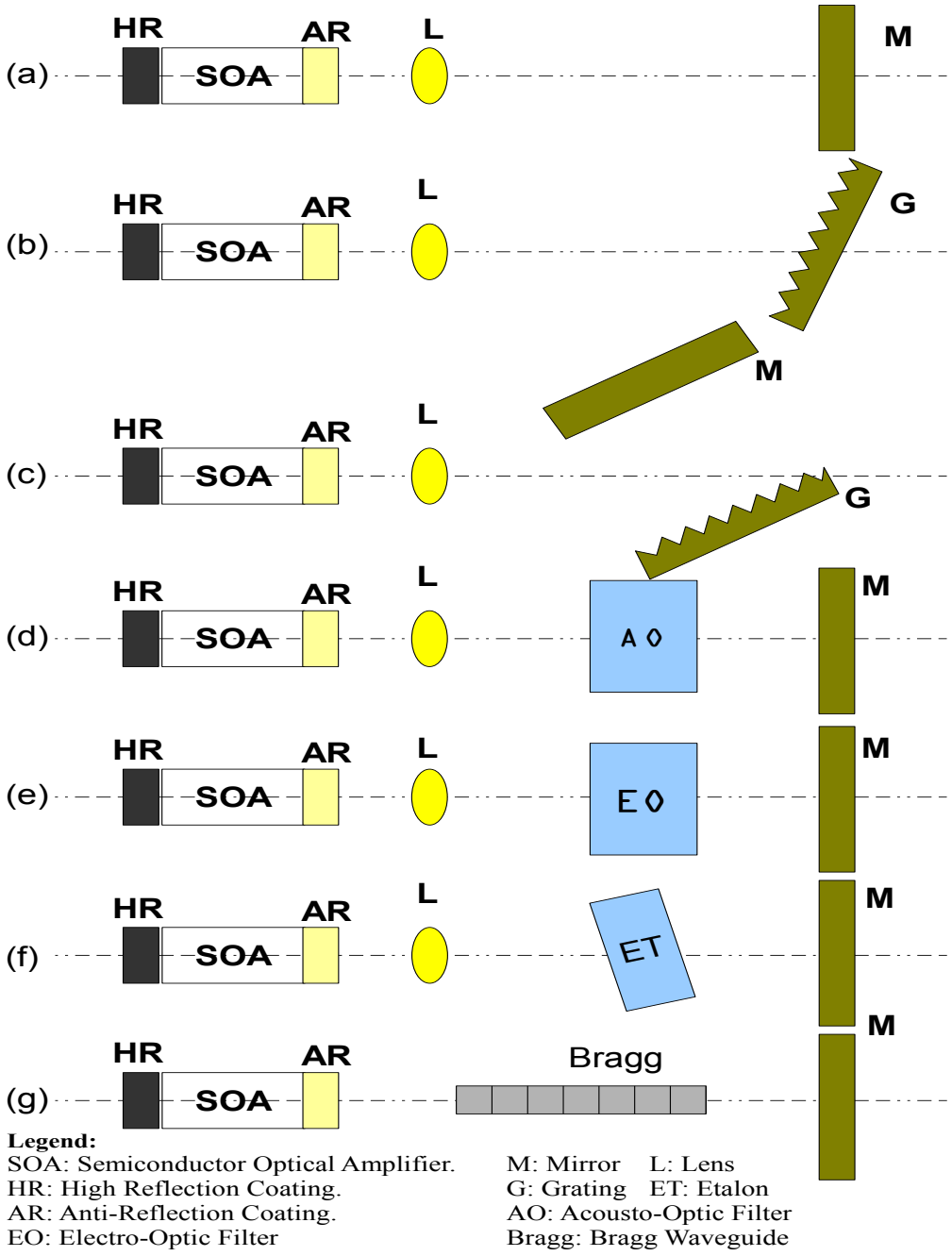

Figure 2.5: Schematic diagrams of different configurations of ECDLs.

2.4 Optical Feedback Effects in External Cavity Diode Lasers

As mentioned in the previous section, ECDL consists of a laser diode and an external reflector such as a mirror or a grating. This kind of configuration exhibits an optical feedback from the external reflector to the laser diode. The operating characteristics of the diode laser is affected by the optical feedback and it depends on several parameters including the level of the feedback in comparison to the diode laser output power, the relative phase of this feedback, the length of the external cavity, and the injection current of the diode laser. [29] found that there are five famous regimes that are defined by the level of the feedback power ratio. Fig. 2.6 shows these regimes and its related frequency spectrum.

Generally, many parameters restrain the regimes boundaries. These parameters are the linewidth enhancement factor, the diode dimensions and the facet coatings. The regimes features are summarized below. While the laser diode behavior in the presence of the optical feedback is more sophisticated than presented here, it is a good guide for most systems and is benefit for categorizing and comparing results.

1. Regime I:
   In this regime, the feedback level is very low (less than $10^{-7}\%$). Such a level has the effect of either narrowing or broadening the spectral linewidth depending on the phase of the feedback [30]. In-phase feedback decreases the linewidth, while out-of phase feedback increases the linewidth [31]. Also the phase of the feedback within this regime has an effect on the lasing frequency and the threshold gain. The advantage of this regime lies not in the manipulation of linewidths achievable but because these effects may happen in systems due to unwanted reflections, minor perturbations, and misalignments.

2. Regime II:
   The transition between regime I and regime II is represented by the observed line broadening (for out of phase feedback) which changes to splitting view of the emission line. This splitting, from a single laser diode mode to a dual

mode, is accompanied by a considerable increase in phase noise and intensity noise arising from the different threshold gain associated with each of the two modes. The two modes observed in this regime do not simultaneously exist; the system lases alternately at each one. As the feedback is increased towards regime III the mode hopping frequency and the mode splitting frequency increases.

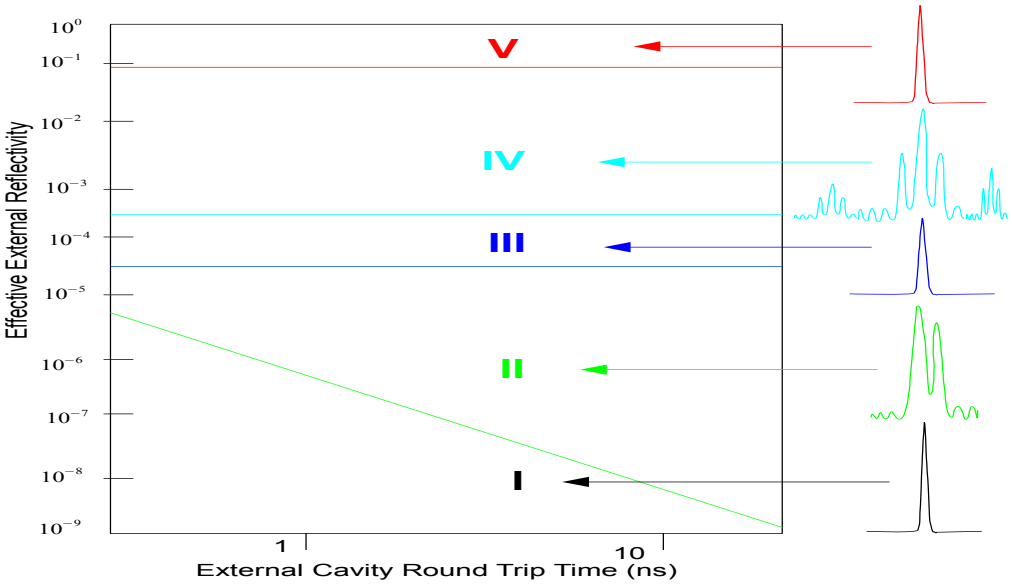

Figure 2.6: Typical regimes of optical feedback, occurring for different values of the external reflectivity and the external cavity length. Also a typical output optical frequency spectrum for each regime is illustrated.

3. Regime III:
   In this regime, stable single mode operation is observed. The stability arises due to the feedback phase and due to the fact that the mode with the minimum linewidth is the dominant lasing mode. The minimum linewidth mode has the best phase stability [32]. This regime exists only within a very small value of feedback power ratios, i.e. 0.01- 0.1%. Due to this small range, the laser is very sensitive to other reflections of minor or comparable

magnitudes, and may jump to the other relatively unstable regimes II or IV. For this reason regime III is inappropriate for most applications.

4. Regime IV:
   When the feedback level reaches a certain value i.e 1-10%, the system transits to regime IV. Typically, this transition passes through a series of bifurcations to a dynamically unstable state. This regime is known as coherence collapse, and it is characterized by a laser linewidth that is broadened by several orders of magnitude (as large as 50 GHz). The system operates on multiple laser diode longitudinal modes, and a broadband intensity noise spectrum occurs [33, 34]. Laser systems operating in this regime have demonstrated that the coherence length of the laser decreases dramatically, by as much as a factor of 1000 times; this results in coherence lengths less than 10 mm [35]. Due to its large broadband output, this regime is useless for coherent communications. However, it is useful for applications such as imaging or secure data transmission which require highly incoherent sources.

5. Regime V:
   This regime is characterized by very narrow linewidth stable single-mode low intensity noise [34] operation. It corresponds to feedback power ratios greater than 10 %. In this regime the properties of the external cavity system are generally assumed to be determined by the external cavity rather than by the laser diode; it operates as a long cavity laser with a short active region. In order to reach this regime, anti-reflection coat of the laser diode front facet is is required. Due to the strong feedback in this regime the system is also much less sensitive to additional reflections. The system operating in this regime is often referred as an ECDL system.

2.5 Fundamentals of Absorption Spectroscopy

Absorption spectroscopic detection is a method which allows the detection of the concentration of a known molecule, or molecules, from a measured optical absorption spectrum of the mixture of molecules. A good quantitative knowledge of the molecule's absorption characteristics is required. This knowledge is the realm of molecular spectroscopy, a complex and highly developed subject. A few fundamental spectroscopic concepts and formulas that are directly applicable to molecule detection are summarized in this section.

Each atom or molecule, small or large, is uniquely characterized by a set of energy levels. Transitions between levels by absorption or emission of electromagnetic radiation result in highly specific spectroscopic features. These features allow both the identification and quantification of the molecular species, such as atmospheric trace gases.

Molecules may undergo transitions between electronic, vibrational and rotational states when exposed to electromagnetic radiation, resulting in absorption spectra. These spectra consist of a number of discrete absorption lines. Each line has a certain linewidth and shape that depends on temperature and what surrounds the molecule. The lines may in some cases be resolved and in other cases the line density may be too high to be spectrally resolved.

Transitions between molecular rotational-vibrational ("ro-vibrational") states occur in the infrared "fingerprint" region of the electromagnetic spectrum, approximately between the wavelengths of 2.5 - 25 μm. Also, overtone and combination-overtone ro-vibrational lines are possible with significantly lower intensities as compared to those for fundamental vibrational bands and the corresponding wavelengths are in the 0.8-2.5 μm spectral region [36]. Transitions between electronic states of atoms and molecules occur in the ultraviolet and visible spectral region. All polyatomic molecules, with the exception of homo-nuclear diatomic molecules (e.g. N_2), absorb infrared radiation. The absorption changes the state of molecular rotation and vibration. An absorption spectrum therefore depends on the physical properties of the molecule such as size and shape and hence each molecule is characterized by a unique spectral "signature".

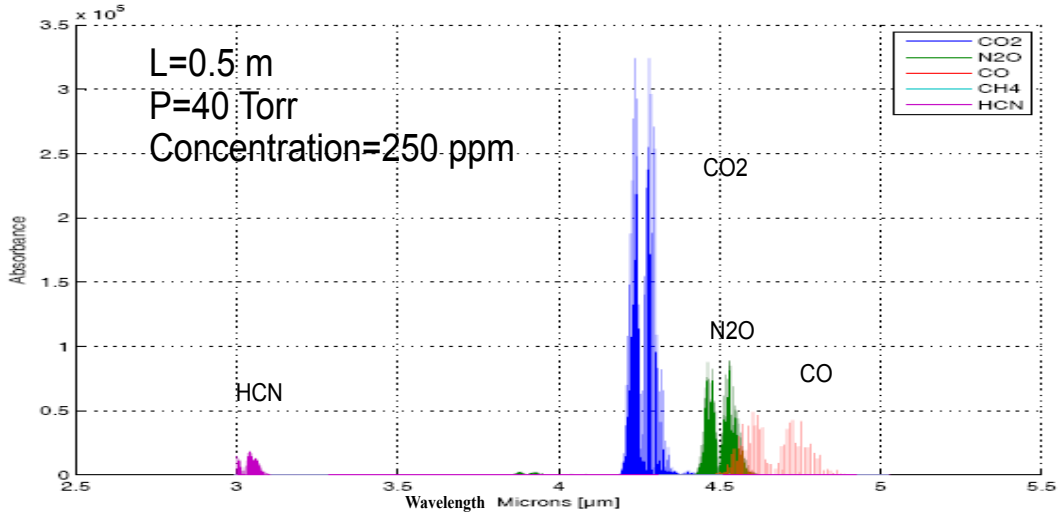

Figure 2.7: HITRAN simulation of absorption bands of various molecules in the 2.5 to 5.5 μm spectral region. All species are plotted with identical relative concentration. Spectral overlap limits the choices of interference free absorption lines

Spectra of linear and some nonlinear polyatomic molecules consist of an array of individual or small groups of lines. In the case of large polyatomic molecules (e.g. benzene, C_6H_6) at atmospheric pressure, many lines overlap each other, resulting in broad spectral features with some occasional peaks.

Direct absorption spectroscopy of gases based on the Beer- Lambert absorption law is often used for quantitative measurements. In the absence of optical saturation and particulate-related scattering, the intensity of light $I(x)$ propagating in a homogeneous gas of sample length L follows the Beer-Lambert law:

$$I(x) = I_o exp[-\sigma(\nu)NL], \tag{2.14}$$

where N represents the molecular concentration and $\sigma(\nu)$ the absorption cross-section. The molecular absorption cross-section depends on frequency and has units of $cm^2 cm^{-1}$ per molecule when integrated over the absorption line, and units of cm^2 per molecule at the line center. For simplicity we assume only one absorbing species. The peak absorption cross-section at line center ν_o is related to the integrated line strength through a line shape function $\Gamma(\nu)$. This function

has the same analytical form for all transitions. In mid-infrared range, the broadening of an individual transition due to finite upper-level lifetime is insignificant compared to broadening by the thermal motion and molecular collisions. Their individual and combined effects on a molecular transition at a frequency ν_n are expressed as follows:
Thermal motion (Gaussian):

$$\Gamma_D(\nu) = \frac{1}{\gamma_D}\sqrt{\frac{\ln 2}{\pi}}e^{(\frac{\nu-\nu_D}{\gamma_D})^2 \ln 2}; \qquad \gamma_D = 3.58 \times 10^{-7}\nu_o\sqrt{\frac{T}{M}}. \tag{2.15}$$

Molecular collisions (Lorentzian):

$$\Gamma_L(\nu) = \frac{1}{\pi}\frac{\gamma_L}{(\nu_o - \nu)^2 + (\gamma_L)^2}; \qquad \gamma_L = \gamma_L^0 p_r\sqrt{\frac{T}{T_o}}. \tag{2.16}$$

Combined broadening (Voigt):

$$\Gamma(\nu) = \kappa_D(\nu_o)\frac{y}{\pi}\int \frac{e^{-t^2}}{y^2 + (x-t)^2}dt; \qquad \kappa_D(\nu_o) = \frac{\int \sigma(\nu)d\nu}{\gamma_D}\sqrt{\frac{\ln 2}{\pi}}, \tag{2.17}$$

with,

$$x = \frac{(\nu - \nu_o)}{\gamma_D}\sqrt{\ln 2}; \qquad y = \frac{\gamma_L}{\gamma_D}\sqrt{\ln 2}; \qquad t = \frac{\delta}{\gamma_D}\sqrt{ln2},$$

where T is the gas temperature in K, M is the molecular weight, p_r is the gas pressure (atm), γ_L^o is the coefficient of pressure broadening $(cm^{-1}atm^{-1})$, $\kappa_D(\nu_o)$ is the peak Doppler cross-section, and δ is the parameter of integration.

The quantities γ_D and γ_L are referred as the Doppler- and pressure-broadened half width at half maximum $(HWHM)$ linewidths respectively. The line shape that results from the combined effect of Doppler- and pressure-broadening is a convolution of the two respective line shapes, and it is known as the Voigt profile. The physical significance of the convolution is that the Voigt profile has different asymptotic shapes for very low and very high gas pressures.

The line intensity is proportional to the lower-state population density of a transition and thus depends on the temperature. These parameters have been measured and calculated for many lightweight gas molecules in the mid-infrared spectrum, and compiled into extensive databases such as HITRAN [37], GEISA

[38], NIST, and PNNL. Numerically accurate absorption spectra can be computed based on these data, not only for single gas species but also for gas mixtures.

Eq. 2.18 is an analytical formula applied for multi-component gas mixtures. The total absorption cross-section $\sigma(\nu)$ is then a weighted average of absorption cross-sections of individual species, with the mole fraction C_m of each species used as the weight coefficient:

$$\sigma(\nu) = \sum C_m \sigma_m(\nu); \sum C : m = 1. \tag{2.18}$$

For each of the m species, the pressure broadening coefficients γ_L^o generally depend on the transition. It also depends on the type of molecule with which the collisions occur. In general, partial pressures in conjunction with the appropriate pressure-broadening coefficients should be used to compute the overall pressure broadening from all gases present in the background (this includes self-broadening). Air-broadening coefficients are useful in calculations, and are listed in spectroscopic databases HITRAN [37], and GEISA [38]. In trace gas sensing applications, however, the species of interest are often present in very low concentrations, so that self-broadening and broadening against other trace gases can be neglected in calculations, and air-broadening alone will suffice. For the condition

Gas	Absorption line Wavelength nm	Line strength $cm^{-2}\ atm^{-1}$ 10^{-12}	Absorption Coeff. at line center $cm^{-1}\ atm^{-1}$
Acetylene C_2H_2	1532.83	20	0.725
Hydrogen iodide HI	1541,00	0.77	0.028
Ammonia NH_3	1544,00	0,92	0.0335
OH radical	1557,30	13	....
Carbon monoxide CO	1567,00	0,057	0.002
Carbon dioxide CO_2	1572,66	0,048	0.0017
Hydrogen sulphide H_2S	1578,00	0,325	0.012

Table 2.1: Gas absorption lines that fall within the SOA gain curve used in this work.

of atmospheric pressure broadening, $\gamma_L^o >> \gamma_D$, the Doppler contribution to the overall linewidth can often be neglected, and the line shape can be treated as pure Lorentzian. Likewise, at pressures low enough to ensure $\gamma_L^o << \gamma_D$, the line shape can be treated as pure Gaussian. In either case, calculation of the line profile is simplified considerably. At intermediate total pressures, $\gamma_L^o \approx \gamma_D$, for which most lightweight gases range from 5 to 100 Torr, calculation of the Voigt profile is necessary to obtain numerically accurate absorption spectra.

Methods for approximate calculation of the Voigt profile, and the related plasma dispersion function, are now a well-developed subject. The approximations published in [39] are particularly useful. Table 2.1 shows the gas absorption lines that fall within the SOA gain curve used in this work.

2.6 Intracavity Laser Absorption Spectroscopy

One of the most established techniques to study the structure of atoms and molecules is the absorption spectroscopic method. Absorption spectroscopy is governed by Beer-Lambert law in Eq. 2.14. The sensitivity of an absorption technique can be increased by increasing the path length or decreasing the noise of the setup without any abrupt change in the laser intensity.

Long effective absorption path length could be achieved by using multi pass cell like White cells. However due to multi reflections by the cell mirrors, which do not have 100 % reflectivities, results the loss of the laser intensity and the enhancement in the pathlength dose not exceed few hundred meters. To increase the path lengths without increasing the noise and loss in the laser intensity, ICLAS method is the best choice for this goal. In ICLAS, the sample of interest is placed inside the laser cavity. This method is boosted the detection sensitivity. Fig. 2.8 shows schematic diagrams of the two absorption spectroscopic methods, when the sample of interest is placed outside and inside the cavity.

In Fig. 2.8(b), light from a laser can reflect back and forth through the sample many times. Transitions of a weak absorber will be amplified by the multiple passes and will appear superimposed on the broad spectrum of the laser. ICLAS is a high resolution, and high sensitive method capable of measuring spectroscopic

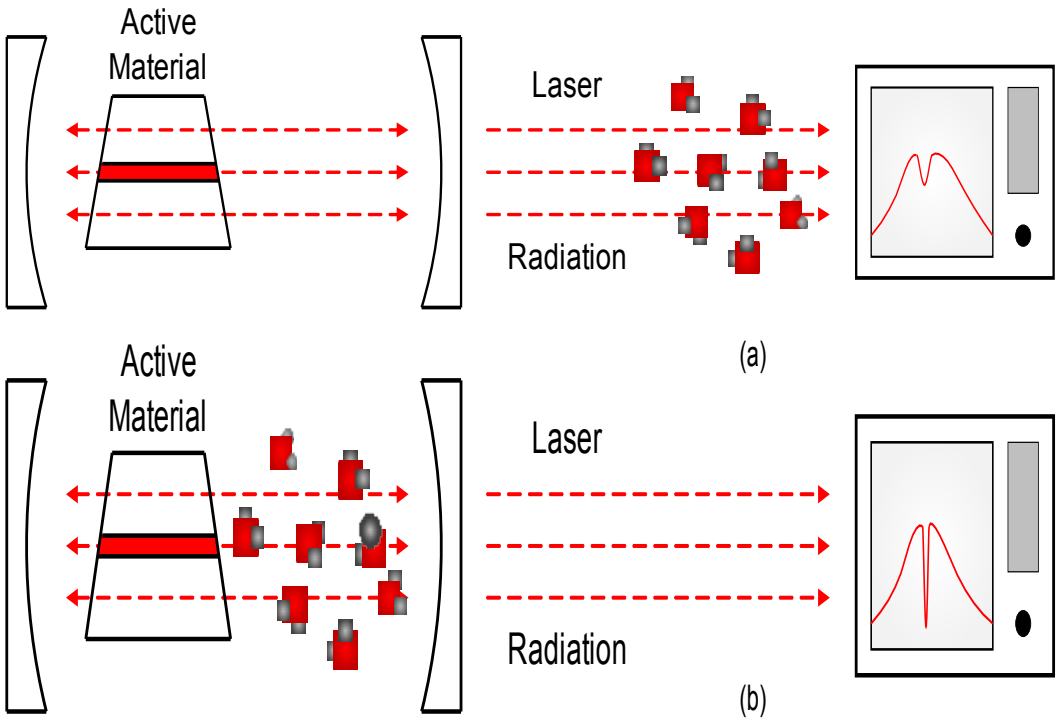

Figure 2.8: (a) Schematic setup of a conventional absorption experiment. A laser is used as light source and its emission subjected to absorption outside of the resonator after amplification. (b) Schematic setup of an ICLAS setup. High sensitivity is achieved by placing the absorber inside the resonator.

line positions, linewidth, lineshapes, and absolute line intensities with a sensitivity exceeds the traditional multi pass absorption cell.

The operation principle of ICLAS depends on that, the laser's gain compensates any broadband or narrow band intracavity losses. In the case of multimode ICLAS, the compensation happens for the absorption lines that are narrow than the gain bandwidth. While in the case of single mode ICLAS, the compensation happens for the absorption lines that narrower than the laser mode bandwidth. The laser works like a multiple pass cell without reflection losses. Very weak absorption lines of the absorber inside the laser cavity will modify the laser spectrum and appear superimposed on the laser spectrum. The sensitivity of ICLAS is exceeding the conventional spectroscopic methods of order of 10^{+5}. The reasons for the enhancement in the sensitivity are:

- The resonator effect i.e. multi pass effect through the absorption cell.
- The threshold character of the laser.
- The competition among the laser modes.

Therefore, maximum detection sensitivity will be observed when the mode competition mechanism is present and the mode coexistence, which reduces the effects of mode competition, is absent.

2.6.1 Multimode Operation

The influence of the mode number on ICLAS plays an important role in term of the sensitivity. The sensitivity in multimode ICLAS is much larger than in single mode ICLAS due to the mode competition effect. Although the sensitivity of single mode ICLAS still exceeds the sensitivity of conventional absorption spectroscopy [40]. Fig. 2.9 shows schematic diagram of the gain spectrum and its related population inversion in two different cases of operation. The first is that when small numbers of oscillating modes are considered Fig. 2.9(a). The second is that when large numbers of modes are considered Fig. 2.9(b).

In the first case when smaller numbers of laser modes are considered, the population inversion distribution along the laser cavity is more inhomogeneous.

In this case the gain saturation is stronger for the stronger oscillating modes, while it becomes weaker for weak modes and a small absorption line of intracavity absorption can be observed in the emission spectrum.

In the second case the population inversion becomes more homogeneous along the laser cavity for the larger number of oscillating modes. In other words the inhomogeneity of the population inversion is gradually smoothed with the increase of the number of lasing modes. In this case, the competition between the lasing modes increases. As a consequence, the emission spectrum condenses stronger and the absorption dip in the spectrum becomes larger [41]. In order to increase

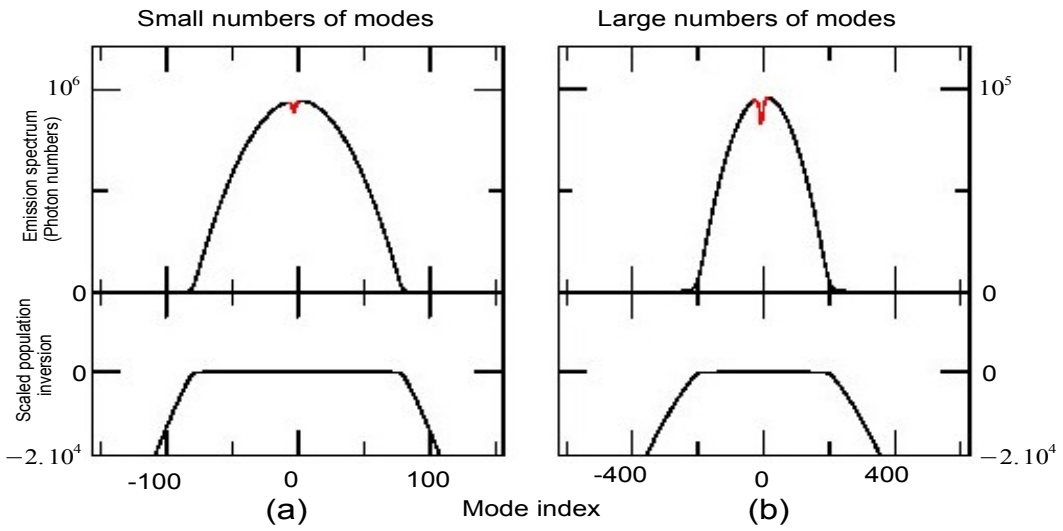

Figure 2.9: Schematic diagram of the gain spectrum and its related population inversion in two different cases of operation. (a) when small numbers of oscillating modes are considered. (b) when large numbers of mode are considered.

the sensitivity resulting from the mode competition effect, more than one mode must be existed [42]. However, this does not mean an increase to large numbers of oscillating modes. [43] investigates that two modes is enough for ICLAS operation. From this point of view ICLAS can be designed with two modes only.

Fig. 2.10 shows schematic diagram of multimode and single mode ICLAS configurations. In Fig. 2.10(a) multimode ICLAS configuration is shown, where the broadband gain provides amplification for all modes supported by the resonator.

The absorber inside the cavity suppresses those modes which coincide with its absorption features. From this point of view of precision and sensitivity, multimode operation is very attractive. Due to the mode competition, the multimode configuration is extremely sensitive and has great advantage of providing the full absorption spectrum of an absorber parallel in one single measurement [44]. Very attractive lasers for this purpose are dye lasers [44, 21] or fiber lasers [45], as they provide very flat gain over a large wavelength range. However, the disadvantages of such a system come at the price and size. The setup shown in Fig. 2.10(a)

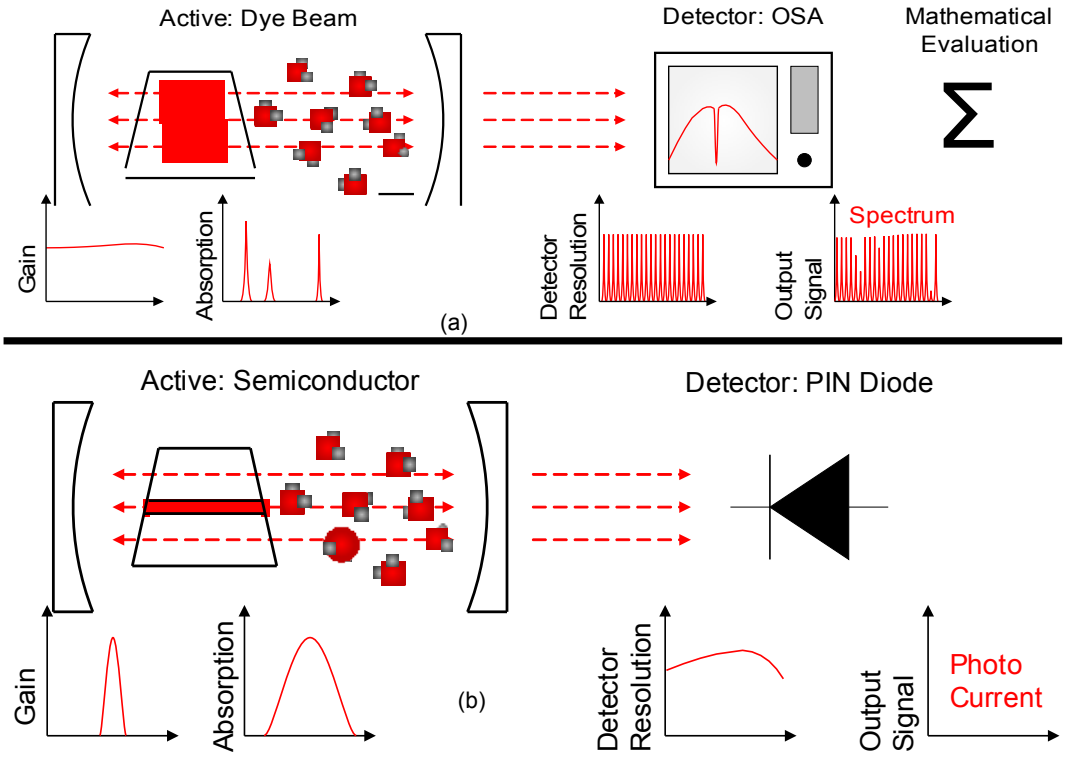

Figure 2.10: Schematic diagram of multimode and single mode ICLAS configurations. (a) In the highly sensitive multimode case complex and expensive dye or fiber laser and high resolution measurement equipment is required. (b) In the single mode case much more cost efficient devices like diode lasers and photo detectors can be applied, but sensitivity is significantly lower.

involves several expensive components. The first is the flat broadband gain which requires either a dye laser system or fiber laser system pumped by a large array

of tailored high intensity pump diodes. Both systems are quite costly. The dye laser system is additionally very delicate in setup and maintenance. To evaluate the optical output of a multimode system, an optical spectrum analyzer (OSA) is required. OSA itself is expensive and bulky instrument. For the introduction of an ICLAS based sensor into the mass market miniaturization is a key factor, as smaller devices have much greater possibilities of implementation. For the system shown in Fig. 2.10(a) miniaturization is highly limited by complexity of the setup and the requirements of the active material. Hence, multimode ICLAS system is rather limited to applications where size, complexity and cost are critical.

2.6.2 Single Mode Operation

In single mode ICLAS, only one mode is used for the detection the absorption features of an absorber inside the cavity. Single mode ICLAS is generally less sensitive than multimode ICLAS due to the absence of mode competition. However, single mode ICLAS system shown schematically in Fig. 2.10(b) is less complex than the multimode ICLAS system described above.

The greatest simplification compared to multimode system is the optical data evaluation where, OSA can be replaced by a photo-detector. The photo-detector output is proportional to the total optical power. Also, single mode ICLAS setup is much simple compared to multimode ICLAS, where single mode ICLAS setup can easily miniaturized by integration in semiconductor material. Tunable semiconductor laser diodes and photo-detectors are available in a vast wavelength range, as semiconductor band gap can be tailored by material composition [46]. The limiting factor for miniaturization is the sample chamber, which has to be designed in regard to the absorption characteristics of the absorber targeted. The cost of such an integrated device is much cheaper than expensive system like the multimode ICLAS setup described above and hence much more suitable for the mass market. However, the great reduction of complexity also leaves its marks in the performance of a device. In the case of the single mode ICLAS setup this means reduction of sensitivity as a result of the absence of mode competition and the limitation to a rather narrow wavelength range.

2.6.3 Two Modes Operation

To gain the advantages of single and multimode ICLAS, patent DE102004037519B4 introduced by Prof. Hillmer is considered [47], where two modes are used in a particular configuration. When one of the two modes is suppressed by an absorption line, the other mode increases due to the mode competition effect. Due to the reduction of mode numbers to two only, data evaluation is significantly simpler.

In the case of two modes ICLAS, the optical data evaluation is the same as in the case of single mode ICAS, where a photodetector can be used for the data evaluation. Because of photodetector is not capable of wavelength selective measurements, a novel measurement method is proposed. This method analyzes the noise of the photo current in the frequency domain, which is very characteristic for the single or two modes states. The frequency spectra obtained in this manner are called RIN and directly correlate with the relative optical intensity of the two modes of the ICLAS system.

As a result, the two modes system is claimed to combine the advantages of multimode and single mode ICLAS systems. It is sensitive as multimode ICLAS system and offers a much less complex setup that is significantly easier to integrate into a miniaturized device. Hence, it is a promising approach to bring ICLAS to a wide range of commercial applications outside of laboratories.

2.7 Noise Characteristics of Laser Diode

Because of the quantum nature of the light, lasers are intrinsically noisy devices. The output power of laser exhibits fluctuations in the phase and intensity, even when the laser is biased at a constant current. The two main mechanisms responsible for this noise are spontaneous emission and electron hole recombination, which is known as "shot noise". The phase fluctuation of output power leads to a finite spectral linewidth when semiconductor lasers are operated continuously at a constant current. However intensity fluctuations are characterized by RIN and they lead to a limited signal to noise ratio (SNR) [48]. These fluctuations can

affect the performance of any system under consideration, however it can also be used as an indicator for mode intensity variation.

2.7.1 Relative Intensity Noise Definition

RIN can be precisely calculated from the autocorrelation integral of optical power fluctuations divided by total power squared. These temporal fluctuations can also expressed in terms of their spectral density via the Fourier transform of the autocorrelation integral. An optical source of output power $P(t)$ and fluctuation $\delta P(t)$ has a total relative intensity noise, RIN_T, given by the ratio of the mean square of the fluctuation to the average power,

$$RIN_T = \frac{< \delta P(t)^2 >}{< P(t) >^2}, \tag{2.19}$$

where the time average $< \delta P(t)^2 >$ arises from the autocorrelation function,

$$\rho(\tau) =< \delta P(t)\delta P(t+\tau) >, \tag{2.20}$$

evaluated at time $\tau = 0$, and the symbol $<>$ denotes either the ensemble or the time average. RIN_T, which is dimensionless, can be represented in the frequency domain by defining RIN spectral density, $R(\nu)$. Where RIN is the integral of the $R(\nu)$ over all frequencies. This implies to

$$RIN = \int_0^\infty R(\nu)d\nu, \tag{2.21}$$

where ν is the linear optical frequency. The spectral density of the RIN, $R(\nu)$ is derived by application of Wiener-Khintchine theorem [49] to the autocorrelation function $\rho(\tau)$. More details of RIN procedure and characteristic can be found in appendix A.

2.7.2 Mode Partition Noise

The intensity noise of the total light output of laser diodes is relatively low, however the partition of the different lasing modes in the total light output fluctuates considerably, yielding the so-called “mode partition noise”. The mode partition

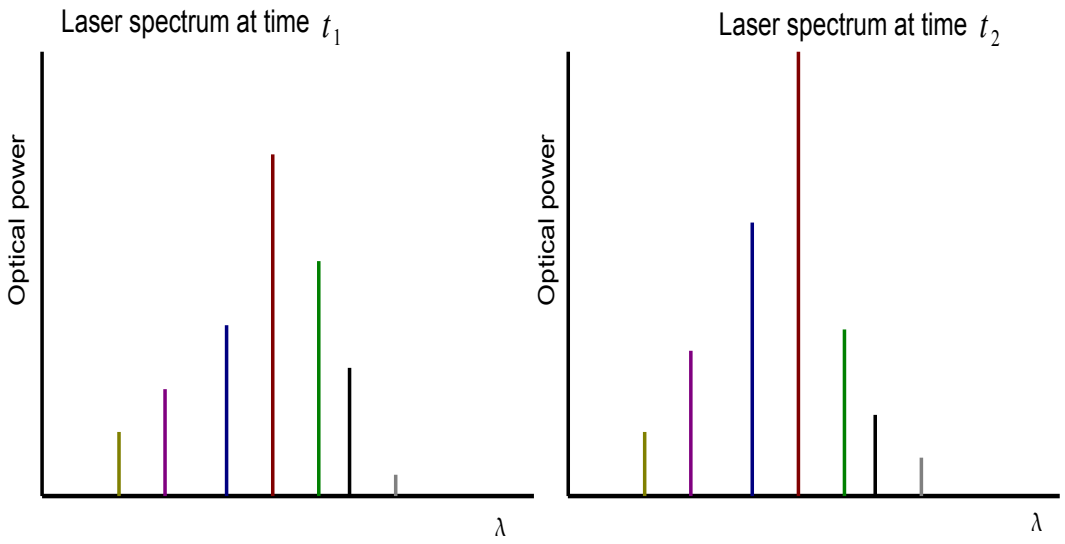

Figure 2.11: Schematic diagram of random spectra at different times t_1 and t_2.

noise is illustrated in Fig. 2.11 which shows the laser spectrum at a random time t_1 and t_2. The total light output power remains constant, but the relative portion of the modal power fluctuates. To understand the mode partition noise we consider that any lasing mode is driven by its spontaneous emission, therefore it represents, at least to some extent, just the amplified spontaneous emission noise. If the photon number is raised, more carriers are consumed yielding a reduction of the gain and thus stabilization of the photon number. This stabilization process is effective only for the total photon number, yielding a low RIN, if the total light output is detected.

The qualitative dependence of mode partition noise on mode spectra is sketched in Fig. 2.12. If the laser diode emits in a single longitudinal mode, it is evident that there is no mode partition noise at all and the RIN is high value Fig. 2.12(a). With increasing the number of modes, the mode partition noise increases, subsequently the mode partition noise is maximum. This can be observed if the laser is enforced to emit in a two or three modes. Fig. 2.12(b) sketches this case. With further increasing of the mode number, a multimode emission occurs and the mode partition noise is low again Fig. 2.12(c).

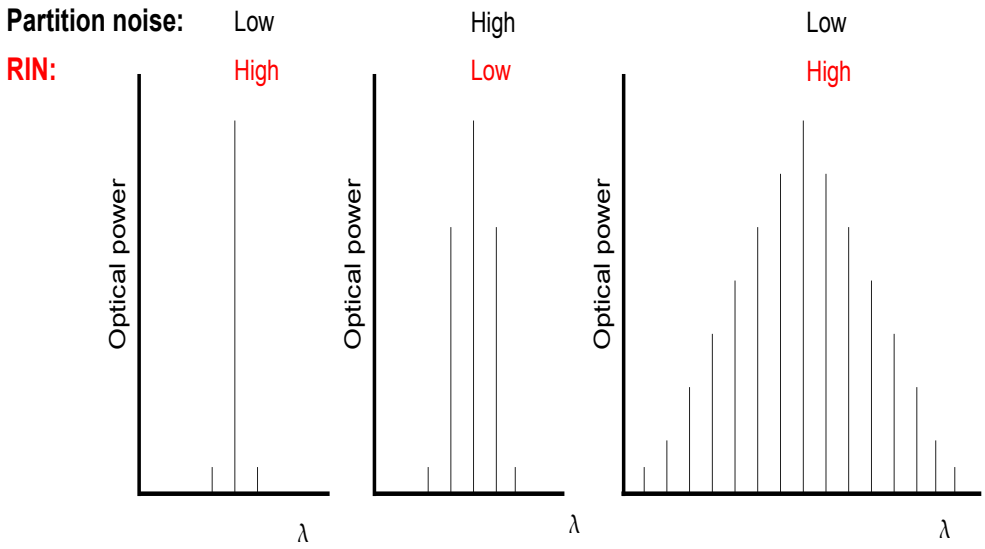

Figure 2.12: Schematic diagram of the relation between number of lasing modes and the mode partition noise

To understand this behavior, the different lasing modes may still be considered as amplified spontaneous emission noise, exhibiting an rms-fluctuation which is roughly equal to their mean values. If the spectral noise density is considered, it is obtained a decreasing of spectral noise density with increasing number of lasing modes, because the coherence is reduced and the noise spreads over a larger bandwidth. Therefore, for very wide multimode spectra the mode partition noise is relatively low again [49].

In the present work, the mode partition noise effect takes place when the two modes are operated at the same wavelength. In this case the output of the laser is very similar to the typical single mode laser operation, where the two modes of identical FWHM and reflectivity are overlapped perfectly. In chapter 5, the experimental measurements of the two modes fiber based laser system and the effect of the mode partition noise are shown.

2.7.3 Mode Competition Noise

Semiconductor lasers happen to show the so called mode hopping noise, which accompanies unstable hopping or jumping among the oscillation modes. This noise tends to be induced by re-injection of the optical output or by changing laser temperature. Excess noise in semiconductor injection lasers which accompanies the competition effect among lasing modes is theoretically analyzed by [50].

In a multimode laser, mode competition takes place among all longitudinal modes, depending on the resonator properties. The existed setup allows the lasing of two modes only. Therefore, mode competition is restricted to these modes. Variation of the intensity of one of them can only happen at the other's one expense. More details of mode hopping noise and its effect on the stability of the semiconductor laser is found in [49].

Chapter 3

Mode Competition Effects in Intracavity Laser Absorption Spectroscopy

In this chapter, theoretical discussion of the mode competition effects in ICLAS is introduced. In order to describe this effects, a simple analytical model introduced by [23] is considered. In typical mode selection procedure, mode selection can be achieved using a grating inside a multimode laser cavity. The selected mode oscillates without competition with other non-selected modes. However, when an intracavity absorption cell is placed inside the laser cavity, which has an absorption line (loss) that matches the selected mode, the selected mode suffers an additional loss and the non-selected modes begins to compete the selected mode. The aim of this chapter is to study the intensity behavior of the selected mode when competition between the selected mode and other modes occurs. Particular coupled rate equations are implemented, which fulfills mode competition condition. From these rate equations the strength of the mode competition is defined. The solutions of these rate equations exhibit two regimes. In the first regime, no mode-competition occurs where the selected mode oscillates alone. While in the second regime, mode-competition occurs, where the non-selected modes begin to compete with the selected mode. The simulated results show abrupt change in the slope of the selected mode intensity, which occurs due to the mode competition effect. From this abrupt change in the slope, the sensitivity

enhancement factor can be extracted and calculated. On the other hand, the experimental measurements show the same behavior when the selected mode suffer from absorption line matching the selected mode directly. In the present case the sensitivity enhancement factor reaches order of 10^3 times the conventional laser spectroscopy

3.1 Mode Competition Definition

The frequency spectrum of multimode lasers is strongly affected by the gain saturation of homogeneous and inhomogeneous transitions. This could be understood from the following arguments:

- If a laser transition with a purely homogeneous line profile is considered. When the pump power exceeds the threshold, the resonator mode that is next to the gain center starts oscillating first. Since this mode has the largest net gain, so its intensity grows faster than the other laser modes. This causes partial saturation of the whole gain profile, mainly by the strongest mode. This saturation decreases the gain for the other modes and their amplification will be slowed down, which further increases the differences in amplification and favors the strongest mode even more. This mode competition of laser modes leads to a complete suppression of all weaker modes except the strongest mode. In fact, such ideal single mode operation without frequency selective elements inside the laser resonator can not be observed because there are several phenomena, such as spatial hole burning or time dependent gain fluctuations, that interfere with the mode competition [51].

- In case of a purely inhomogeneous gain profile, the mode competition phenomena does not occur because the different laser modes do not share the same transitions for their amplification. Therefore all laser modes can oscillate simultaneously above threshold.
  In reality, lasers do not belong to the two pure cases mentioned above, but exhibit a gain profile that is a convolution of homogeneous and inhomogeneous broadening. The strength of the mode competition is governed by the

ratio of mode spacing and the homogeneous linewidth and that is a crucial for resulting single or multimode operation.

3.1.1 Effect of Mode Competition in Intracavity Absorption Spectroscopy

ICLAS is a highly sensitive technique for the detection of a very weak absorption lines. ICLAS consists in placing the absorption cell inside the cavity of the laser with a broad homogeneous emission line. The sensitivity of ICLAS exceeds the conventional spectroscopic methods of order of 10^5. The reasons for the enhancement in the sensitivity are:

- The resonator effect i.e. multi pass effect through the absorption cell.
- The threshold character of the laser process (for cw laser operation) .
- The competition between the laser modes.

Therefore, maximum detection sensitivity is observed, when the mode competition mechanism is present. Only in this case the mode, which is distinguished by an additional loss (due to the absorption cell), will be (in cw operation) completely quenched as a consequence of the mode competition with the other modes, possessing the same lower loss. In this manner, the detection sensitivity will be maximum. However, in fact, several mechanisms which reduce the mode competition are present. These effects are:

- Spontaneous emission which prevents the modes from being completely extinguished.
- An inhomogeneous contribution to laser line broadening (this means, a given mode is coupled, with different strength, to different group of atoms).
- The spatially inhomogeneous intensity distribution of standing wave type modes, which implies that a given mode depletes the inversion mainly of such points in space where its anti nodes are located.
- Effects caused by spatial and temporal inhomogeneity of the laser medium.

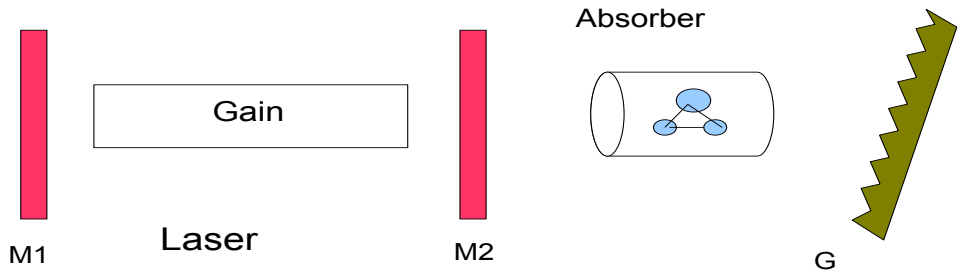

Figure 3.1: Schematic diagram for mode selection setup (where M1, M2 mirrors with reflectivity R_1 and R_2, respectively; G, grating with reflectivity R_G).

3.1.2 Rate Equations and Mode Competition

In order to describe the mode competition theoretically, a simple model introduced by [23] has been considered , where a multimode laser with m mode numbers labeled by subscript i have been considered. The loss by mode i is denoted by κ_i, and the mode i with photon number S_i interacts with N_i atoms excited by the pumping rate p_i and coupled only to this mode. On the other hand, with N_o atoms excited by pumping rate p_o and coupled to all modes. The following rate equations can be written:

$$\frac{dS_i}{dt} = -\kappa_i S_i + BS_i(N_o + N_i), \tag{3.1}$$

$$\frac{dN_i}{dt} = p_i - BN_iS_i - \gamma N_i, \tag{3.2}$$

$$\frac{dN_o}{dt} = p_o - BN_o\sum_k S_k - \gamma N_o, \tag{3.3}$$

where B is Einstein coefficient and γ is the inverse mean lifetime of the excited atoms due to relaxation processes. Here, for simplicity the effect of spontaneous emission has been neglected. The subscript s denotes the selected mode, and the subscript o denotes to the other modes (non-selected modes).
For steady state operation, the loss κ_i can be written as:

$$\kappa_i = B\left(\frac{p_o}{B\sum_k S_k + \gamma} + \frac{p_i}{BS_i + \gamma}\right). \tag{3.4}$$

For the simplicity, the pump power $p_i = p_s$ is assumed and it is independent of i. The single pass gain g_s is introduced as:

$$g_o = \frac{p_o B}{\gamma}\frac{L}{c} \qquad and \qquad g_s = \frac{p_s B}{\gamma}\frac{L}{c}, \tag{3.5}$$

and the loss per round trip is:

$$\eta_i = \kappa_i \frac{L}{c}, \tag{3.6}$$

where L is the cavity length and c is the velocity of light. The photon number S_i is normalized as $Q_i = \frac{B}{\gamma} S_i$.
Using the normalized photon number and the loss per round trip, the modified equation can be written as:

$$\frac{\eta_i}{p_o} = \frac{1}{1 + \sum_k Q_k} + \frac{p_s/p_o}{1 + Q_i}. \tag{3.7}$$

The fraction $\frac{p_s}{p_o}$ can be written as a new parameter ϵ, which is characterized the relative strength of the mode competition effect.
For

$$\epsilon >> 1 (\rightarrow \infty; \Rightarrow p_o = 0)$$

leads to complete independent of the modes (no mode competition) the mode oscillates independently from the other modes.

While

$$\epsilon \rightarrow 0 \Rightarrow p_s = 0$$

modes with different intensities can not exist at all (any mode discriminated by slightly increased loss become totally quenched, as a result of mode competition). Now the parameter ϵ is used to investigate the influence of the mode competition on the detection sensitivity in ICLAS.

In order to study the influence of the mode competition on the detection sensitivity in ICLAS, a simple intracavity configuration is assumed Fig. 3.1. For simplicity, the following assumptions have been considered. It is assumed that $m-1$ modes have the same losses $\eta_i = \eta (i \neq 1)$ and hence, also the same photon numbers ($Q_i = Q \quad for \quad i \neq 1$), while one mode, say $i = 1$, has a lower loss $\eta_1 < \eta$ (due to the grating) and therefore, is privileged.

If an absorption cell with absorption line matches the selected mode is placed inside the cavity Fig. 3.1. The loss η_1 of the selected mode is increased by $d\eta_1$. Therefore the selected mode intensity Q_1 is decreased by dQ_1.

Now the goal is to calculate $dQ_1/d\eta_1$. The coupled system of Eq. 3.7 for the selected and the other modes can be written in the following:

$$\frac{\eta_1}{p_o} = \frac{1}{1+Q_1+(m-1)Q} + \frac{\epsilon}{1+Q_1}, \tag{3.8}$$

$$\frac{\eta}{p_o} = \frac{1}{1+Q_1+(m-1)Q} + \frac{\epsilon}{1+Q}. \tag{3.9}$$

It is easy found that:

$$\frac{d\eta_1}{p_o} \cong \frac{dQ_1\epsilon}{(1+Q_1)^2} \qquad or \qquad \frac{dQ_1}{Q_1} \cong \frac{(1+Q_1)^2}{p_o\epsilon Q_1}d\eta_1, \tag{3.10}$$

where dQ_1/Q_1 is the relative difference in the photon number caused by the additional absorption cell, and it represents the quantity to be detect experimentally. From Eq. 3.10, the sensitivity enhancement factor $\zeta = \frac{(1+Q_1)^2}{p_o\epsilon Q_1}$ indicates an increase of the detection sensitivity of ICLAS in comparison with single pass detection outside the cavity. The sensitivity enhancement factor ζ can be introduced in the form:

$$\zeta = \frac{m+\epsilon}{\epsilon\eta} \ [\frac{p_o(1+\epsilon)}{\eta} - 1]^{-1}. \tag{3.11}$$

For the near threshold region, the term $\frac{p_o(1+\epsilon)}{\eta} - 1 << 1$, the sensitivity enhancement factor ζ is independent of mode competition effects for incompletely inhomogeneous laser line, which corresponds to $\zeta >> m$, and therefore, is only given by the resonator η^{-1} and threshold effects $[\frac{p_o(1+\epsilon)}{\eta} - 1]^{-1}$.
For strong mode competition $\epsilon << m$, the detection sensitivity is proportional to ϵ^{-1} and can reach a high value.
Therefore, the parameter ϵ should be very small to result a very strong mode competition, which increases the sensitivity of ICLAS.
Eqs 3.8, 3.9 allow for two types of solutions, crossponding to either (a) no mode competition (only the selected mode is oscillate and the other modes are completely quenched) or (b) mode competition.
When the loss η_1 is gradually increased, a critical point equal η_{1c} is reached

which marks the transition between two regimes (a) and (b) mentioned above i.e for $\eta_1 > \eta_{1c}$ the remaining modes will oscillate too (regime (b)), however at lower intensities.
Putting $Q = 0$ in Eqs. 3.8, 3.9, the intensity of the selected mode Q_1 is written as:

$$Q_1 = \frac{p_o(1+\epsilon)}{\eta_1} - 1 \quad for \quad \eta_1 \leq \eta_{1c}, \tag{3.12}$$

and the critical point η_{1c} is written as:

$$\eta_{1c} = (1+\epsilon)(\eta - p_o\epsilon). \tag{3.13}$$

The difference between η and η_{1c} is given by:

$$\eta - \eta_{1c} = \epsilon\eta \left[\frac{p_o}{\eta}(1+\epsilon) - 1\right]. \tag{3.14}$$

While in regime (b), where $\eta_1 > \eta_{1c}$ the intensity of the selected mode can be described by a cubic equation as follows:

$$\begin{aligned} &\Delta(1+Q_1)^3 + \left[1 + (m-1)(1-\Delta) - \frac{p_o\Delta}{\eta_1}(1+\epsilon)\right](1+Q_1)^2 \\ &- \left\{m - 1 + \frac{p_o}{\eta_1} + \frac{p_o\epsilon}{\eta_1}\left[1 + (m-1)(1-\Delta)\right]\right\}(1+Q_1) + (m-1)\frac{p_o\epsilon}{\eta_1} = 0 \end{aligned} \tag{3.15}$$

where $\Delta = \frac{\eta - \eta_1}{\epsilon p_o}$ for $\eta_1 > \eta_{1c}$.

A typical solution of Eqs. 3.12, 3.15 are presented in Fig. 3.2. It is obvious that the slope the regime (b) is much steeper than in the regime (a) near the critical point η_{1c}. The abrupt change in the slope from regime (a) to regime (b) gives information about the mode competition strength, and is proportional to the factor $\frac{1+\epsilon}{\epsilon}$.

In order to calculate the sensitivity enhancement factor of the existing sensor, liquid propofol has been measured. Fig. 3.3 shows the normalized intensity of the selected mode versus the propofol molarity . The sensitivity enhancement factor has been calculated from the abrupt change in the slope of the normalized intensity of the selected mode. The sensitivity enhancement factor has been found to be of the order of 10^3 in comparison to the conventional absorption spectroscopic methods.

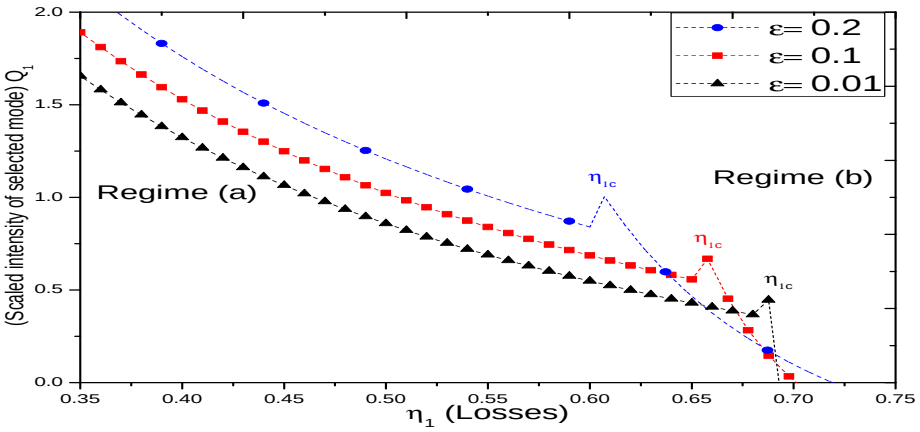

Figure 3.2: Simulation results for the intensity of the selected mode Q_1 versus its losses η_1 at different values of the parameter ϵ. The critical points η_{1c} mark the transition between the two regimes.

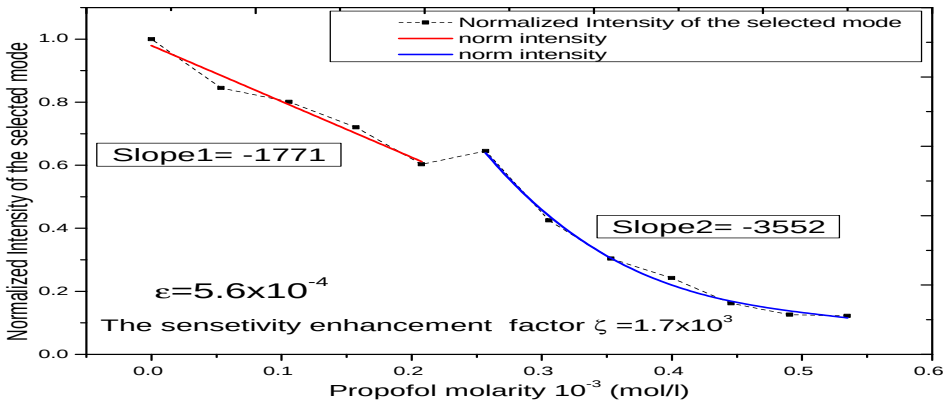

Figure 3.3: Experimental measurements of the intensity of the selected mode versus the propofol concentration (loss). Here the sample under consideration is liquid propofol. The sensitivity enhancement factor ζ has been calculated from the abrupt change of the slope between the two regimes. More details of the experimental measurements will be discussed in chapter 6

Chapter 4

Two Modes Sensor Design

In this chapter, the two modes fiber based ICLAS setup is demonstrated. In order to achieve this purpose, a short overview of the passive and the active components, which are used to implement two modes fiber based ICLAS sensor is introduced . One of the most important device in the existing setup is the SOA, which belongs to the active components, and it represents the gain medium in the existing setup [52]. Because of its interest, more details of its characterization is introduced. The fiber Bragg gratings (FBGs) represent the wavelength selective elements in the sensor setup, and it belongs to the passive components. Thus more effort is taken for its benefits and usages. In the existing setup, fiber loop reflector (mirror) is used in order to reflect 100% from one side of the gain medium. The operation principle of the fiber loop reflector is highlighted. The two modes fiber based ICLAS setup passed many stages to reach the final laboratory setup. The first stage is titled as "single mode operation". In this stage, one FBG is attached to the SOA, so one single mode is observed. The second stage is titled as "two modes operation non-equilibrium state", where two FBGs are attached in line with the gain medium SOA, therefore, two modes operation is observed. However the two modes intensities are not in equilibrium state due to the shape of the gain profile. The third stage is titled as "two modes operation equilibrium state". In this stage, variable couplers are used in order to balance the intensities of the two modes. The last laboratory stage titled as "final laboratory stage". In this final laboratory stage, the setup is opened in order to insert the sample

cell inside the cavity. For this purpose, free propagation fiber based collimator is inserted inside the setup.

4.1 Basic Elements of the Two Modes Sensor

4.1.1 Active Device: Semiconductor Optical Amplifier

The terms Semiconductor Optical Amplifier, Laser Diode Amplifier (LDA), Semiconductor Laser Amplifier (SLA), Traveling Wave Amplifier (TWA), and Fabry-Perot Amplifier (FPA) are different names used in the literatures for the same kind of device. A SOA is very similar to a semiconductor laser with negligible optical facet reflectivity. Fig. 4.1 shows schematic diagram of the SOA structure. An incoming signal is injected into the SOA propagates along its optical waveguide and is amplified by stimulated emission. The optical gain is achieved by inverting the carrier population in the active region via electrical pumping. Fig. 4.2 shows simulation of the SOA gain when two optical signal are propagated along the SOA. All the different SOA structures available today are based on a semiconductor pn double hetero- junction, providing electrons and photons confinement.

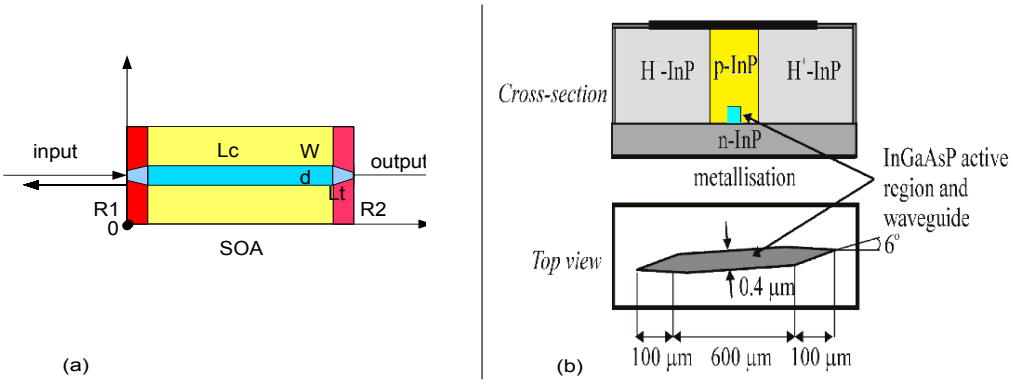

Figure 4.1: Schematic diagram of the SOA structure: (a) shows in-plane cross section of the SOA, and (b) shows cross section and top view of the SOA. Here R_1, R_2 represents the facets reflectivities. and W, d, L_c, L_t represents the width, thickness, active region length, and tapered length respectively.

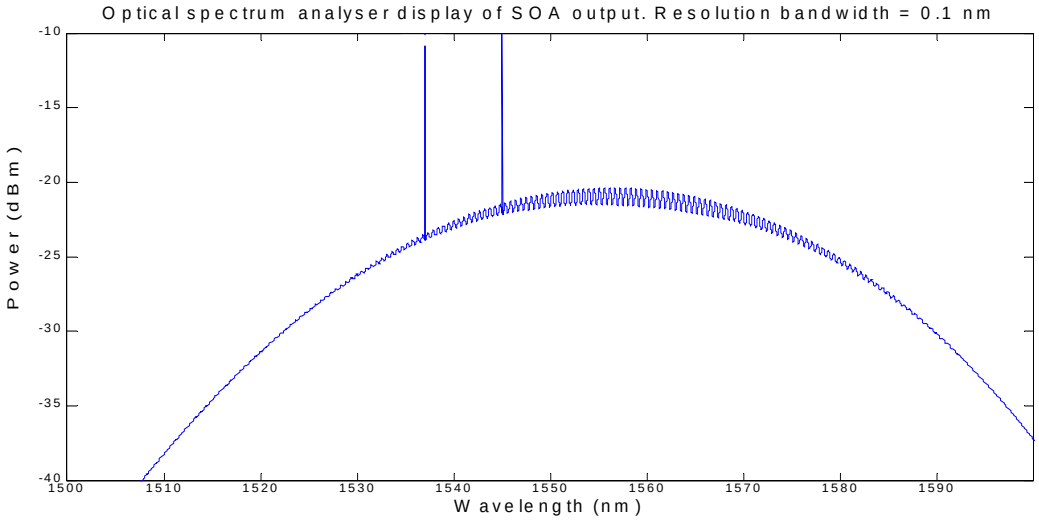

Figure 4.2: Simulated output power (dBm) of two input signals along SOA. This simulation have been done using wide-band steady-state model [53].

4.1.1.1 Facets Reflectivities

In order to reduce optical feedback into the active region, low facet reflectivity is required. If the reflectivity is not low enough,typically lower than 10^{-5}, ripples are observed in the gain spectra. When the ripple depth is larger than 3 dB the SOA is usually called a Fabry-Perot amplifier. Although the small signal gain can be enhanced by the cavity resonance, facet reflections generally affect the SOA performance in a bad way. Fluctuations or ripples at the signal wavelength cause variations in the signal gain. Moreover, too large facet reflectivities lower the carrier density, the gain bandwidth, the output saturation power, and enhance the noise figure [54, 55]. Different approaches have been used to reduce the SOA ripple, so ARCs are used together with one of the following concepts. One possibility is to tilt the active waveguide so that the light is reflected away from the active region. Angles are typically between 5 and 10 degree.

Another method is to taper the waveguide or to use a window region (i.e. to terminate the waveguide before the facet) in order to expand the mode profile. In this way only a small part of the optical signal is reflected back into the active region.

4.1.1.2 Types of Semiconductor Optical Amplifiers

In the simplest SOA structure, the device consists of a single mode active waveguide which can be either buried or ridge type. Additionally, in order to increase the fiber chip coupling efficiency and to reduce the facet reflectivity, tilted waveguides, with tapers is used. However, more elaborate structures also exist. The Gain-Clamped SOAs (GC-SOA) have been developed for linear applications, where the carrier density (and thus the gain) is clamped to a fixed value through a laser oscillation. This increases the dynamic range of the linear operation. The clamping beam can oscillate either along the waveguide (see [56] and references therein) or in the orthogonal direction. The latter is also called Linear Optical Amplifier (LOA).

Active MMI-SOAs have been developed to increase the output saturation power [57] by increasing the active waveguide area, while keeping the single mode operation. An active directional coupler structure (DC-SOA) has been used to perform wavelength conversion [58]. So far, all the listed structures are edge emitting devices. Vertical-Cavity SOAs (VCSOAs) have also been demonstrated. However, they must be used in the resonant mode to achieve appreciable gain, because of the very short active region length. In other words, they are narrow band SOAs with a typical optical bandwidth smaller than 1 nm. On the positive side they are intrinsically polarization independent. Also they have large coupling efficiency, low noise figure, and low production cost [59, 60].

4.1.2 Passive Devices: Fiber Bragg Grating

The discovery of photo sensitivity in optical fibers [61] has had a large impact on telecommunications and on sensor systems with the effect being used to develop devices for many applications [62].

The fabrication of a Fiber Bragg Grating (FBG) is generally based on the photo-sensitivity of silica fiber doped with germanium. When illuminated by UV radiation, the fiber exhibits a permanent change in the refractive index of the core. Meltz et al [63] demonstrated the first production of Bragg gratings by the side exposure method, in which a spatially modulated intensity interference pattern was used to photo-inscribe a periodic refractive index grating. The side exposure

of the fiber by the interference of two intersecting beams of UV radiation allows fabrication of FBGs with user defined central wavelength, which is independent of the wavelength of the writing laser Fig. 4.3. This UV exposure of the fiber

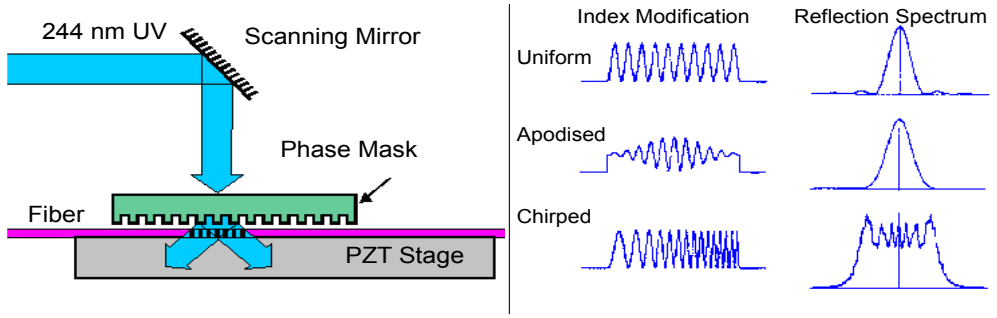

Figure 4.3: Schematic illustration of the fabrication of FBGs using a phase mask technique.

imprints a regular structure of periodicity half the required Bragg wavelength into the fiber core over lengths in the range of millimeters to centimeters. The flexibility of this method allows Bragg wavelengths from the visible region to well beyond the telecommunications wavelength of 1550 nm to be written [61].

FBG interacts with the propagating wave in the core creating the diffraction phenomena analogous to that of wave interaction with regular structures in crystals and bulk optical gratings. The interaction with the propagating wave allows the coupling of the forward mode to the backward mode with characteristics depending on the properties of the FBG. FBGs have found applications in routing [64], filtering control and amplification of optical signals [65], as the feedback element in fiber lasers [66], in dispersion compensation [67] and in sensing applications [68].

For a typical FBG of length of 5 mm and period of 0.5 μm, it comprises thousands of periods. These highly regular and partially reflective modulation planes reflect a set of waves, which then interfere. This interference is in general destructive, however, for the wavelength that satisfies the Bragg condition, the reflected light constructively interferes. So the FBG acts as a mode coupler,

coupling the forward propagating mode to a backward propagating mode only when the resonant condition is satisfied.

4.1.2.1 Uniform Fiber Bragg Grating

In a uniform FBG, the period remains constant through the length and the reflection is the strongest at the Bragg wavelength, λ_B. The Bragg resonant wavelength is a function of the period Λ, and the effective refractive index n_{eff}, which is given by [69];

$$\lambda_B = 2n_{eff}\Lambda. \tag{4.1}$$

Light at the Bragg wavelength propagating in the fiber undergoes reflection and the rest of the light is transmitted through the grating. The spectral characteristics depend on the grating's parameters such as the amplitude of the refractive modulations, grating length, the coupling strength and the overlap integral of the forward and backward propagating modes. A typical reflection spectrum of a uniform FBG is shown in Fig. 4.4.

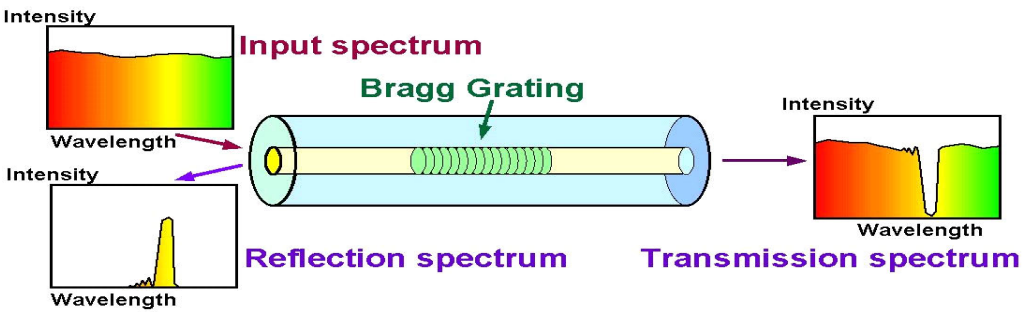

Figure 4.4: Schematic diagram of a FBG illustrating that only the wavelength of light, λ_B, that satisfies the Bragg condition, is reflected.

4.1.3 Passive Devices: Fiber Loop Reflector

Reflectors fabricated from optical fiber are interesting and potentially very useful components for use in optical devices and systems. Generally, the reflectors are

fabricated by forming a fiber loop between the output ports of a directional coupler. The use of fused coupler techniques to fabricate the coupler results in devices which are both low loss and stable. In addition, the reflectors are easily fabricated from a single length of fiber, thus reducing unwanted reflectors and additional loss caused by fiber splices. The reflectivity of a perfect device reaches 100%.

4.1.3.1 Fiber Loop Reflector: Operation Principle

Fig.4.5 shows schematic diagram of a fiber loop reflector. It consists of a loop of optical fiber formed between the output ports of a directional coupler. Assume that light propagates towards the coupler in port 1 and the coupler couples half of the power into port 3 and half into port 4. So fifty percent of the input light travels clockwise. Coupled light across the waveguide suffers a $\pi/2$ phase delay with respect to light which is traveling straight. The transmitted intensity in port 2 is therefore the sum of a clockwise filed of arbitrary phase ϕ and an anticlockwise field of relative phase $\phi - \pi$, both of equal amplitudes. This results in a zero transmitted intensity and by conservation of energy law all input light is reflected back along the input port 1 [70].

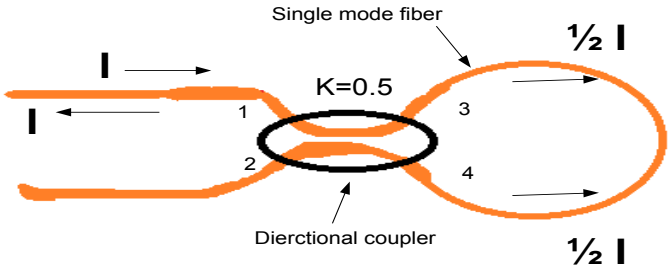

Figure 4.5: Schematic diagram of a fiber loop reflector.

4.2 Sensor Design: Demonstration Stages

To demonstrate two modes fiber based ICLAS sensor, the sensor setup passes many stages to reach the final laboratory setup. In this section, The different demonstration stages with the help of the active and passive optoelectronic components described above are described.

4.2.1 First Stage: Single Mode Operation

In order to achieve single mode oscillation, a SOA, and FBG are used. Fig. 4.6 shows the schematic diagram of the first stage (single mode operation), where the SOA serves as a gain media and the FBG serves as a wavelength selective

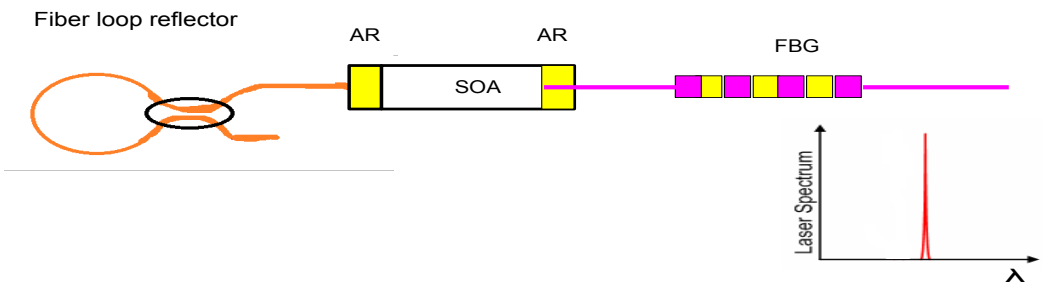

Figure 4.6: Schematic diagram of a single mode operation (first stage) and its output laser spectrum. Here SOA is a semiconductor optical amplifier and FBG is a fiber Bragg grating.

element. The fiber loop reflector is attached to one end of the SOA which enables 100 percent broadband reflection of the propagated light.

The SOA (InPhenix IPSAD1501-L213), an inhomogeneous gain medium, enables stable multi-wavelength amplification and thereby serves as an optical source. It has a high optical gain (20 dB chip level gain at 1550 nm) and low polarization sensitivity (less than 1 dB polarization dependent gain). Owing to the anti reflection (AR) coating design, the facets reflectivity has been reduced to below -40 dB. The FBG has 99.9% reflection with 3 dB bandwidth of 150 pm. To

reduce coupling loss and back reflections, all devices mentioned above are either spliced to each other or connected with measurement instruments by means of fiber connectors/ angle-polished connectors (FC/APC).

4.2.2 Second Stage: Two Modes Operation (Non-Equilibrium State)

In this stage, a second FBG_2 has been connected to the first FBG_1. Therefore two modes operation have been achieved. However, the intensities of the two modes are not equal. This behavior is due to two reasons.

The first reason is that, the gain media has a parabolic gain curve, where one mode has a lower gain as compared to the other. So the long wavelength mode begins to oscillate first and the short wavelength mode oscillates later.

The second reason is that the sensor setup consists of two main resonators, which have different physical lengths. Therefore non-equilibrium state of the two mode has been observed. Fig. 4.7 shows a schematic diagram of the two modes' operation setup and its output spectrum. Fig. 4.8 shows the experimental

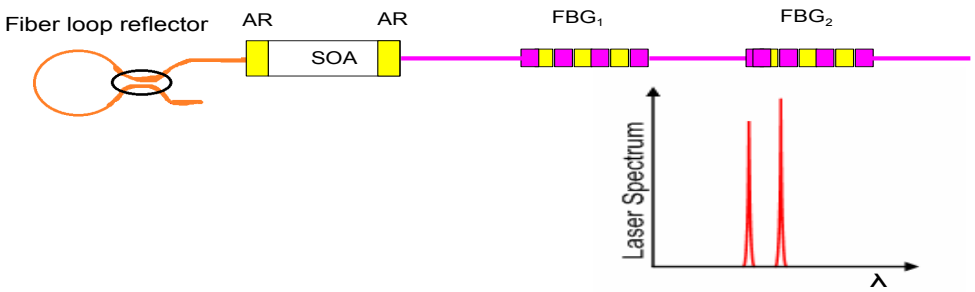

Figure 4.7: Schematic diagram of two modes operation (second stage non-equilibrium state) and its output laser spectrum. Here SOA is a semiconductor optical amplifier and FBG is a fiber Bragg grating.

measurements of the two modes' operation. It appears that the two modes are not in equilibrium state, where the longer wavelength mode experiences a higher

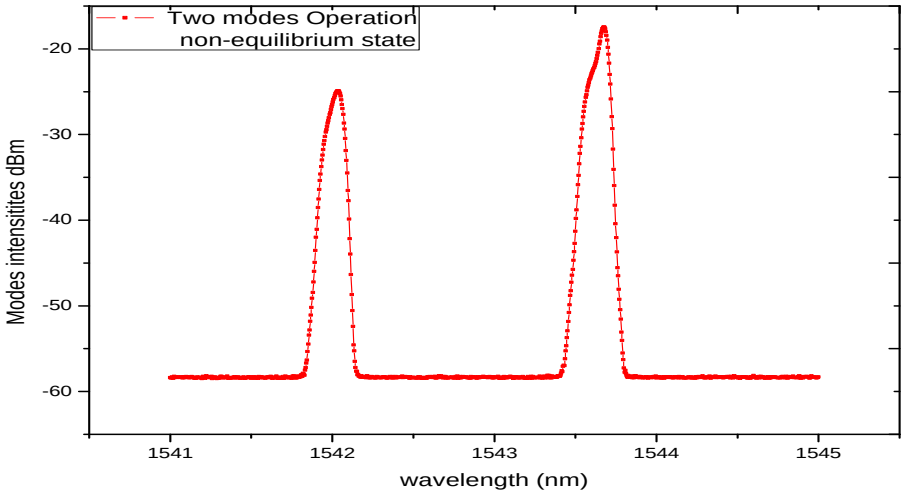

Figure 4.8: Experimental measurements of the two modes operation. It appears that the two modes are not in equilibrium state.

optical gain than the shorter wavelength mode. Therefore, the longer wavelength mode starts lasing at relatively low injection current while the shorter wavelength mode starts lasing at relatively high current. The gain difference prevents the two modes to lase at the same injection current. In order to balance the gain of the two modes, there are two possibilities.

The first possibility is to tune the FBG at nearly same gain values, however this solution takes the system out of its main goal (molecular detection needs high selectivity and tuneabilty).

The second possibility is to insert a variable loss inside the long wavelength cavity to prevent this mode to lase at low injection current.

4.2.3 Third Stage: Two Modes Operation (Equilibrium State)

In order to eliminate the problem resulting from the previous stage, insertions of suitable attenuators or variable losses before each FBGs are considered. The attenuators enable to adjust the intensities of the two modes by varying the loss inside the cavities, and subsequently adjusting the threshold current of the two modes .

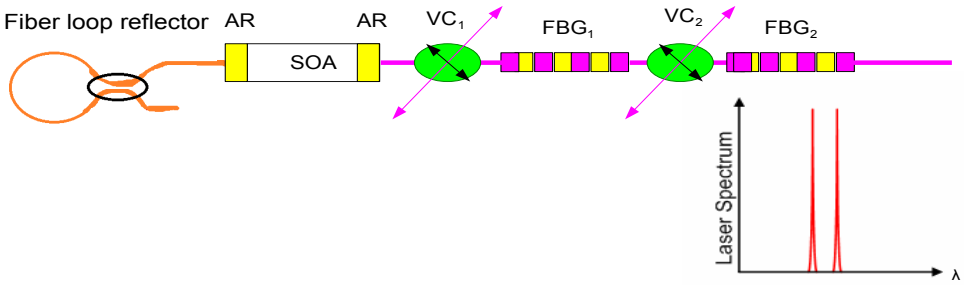

Figure 4.9: Schematic diagram of two modes operation (third stage-equilibrium states) and its output laser spectrum. Here SOA is a semiconductor optical amplifier FBG is a fiber Bragg grating, and VC is the variable coupler.

However the commercial attenuators have many technical problems such as high

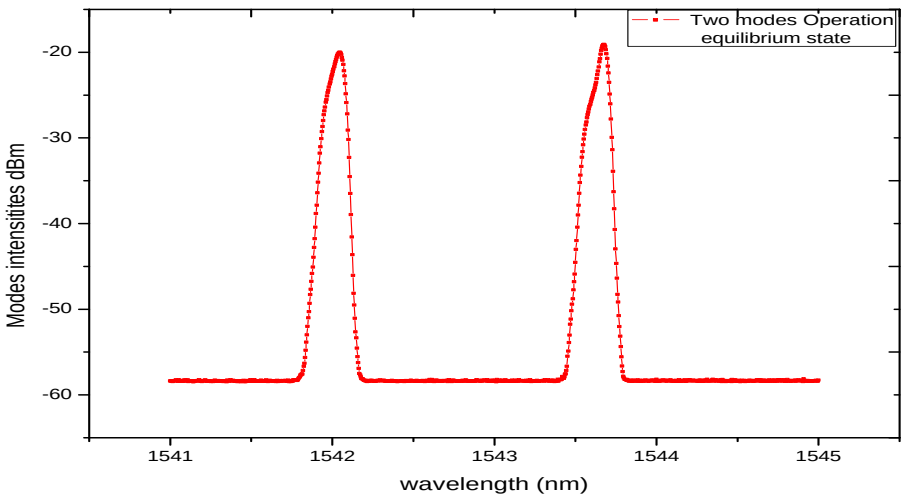

Figure 4.10: Experimental measurements of the two modes' operation. It appears that the two modes are in equilibrium state.

insertion losses. Instead of attenuators, variable couplers have been used. Variable couplers have the advantages of attenuators and couplers at the same time. The variable coupler has two functions. The first function is that it can attenuate

the entire intensities of the two modes, therefore the intensity adjustment can be achieved. The second function is that it can couple out the spectrum to the optical spectrum analyzer and/or electrical spectrum analyzer (ESA), which are used to view the output spectrum. Fig. 4.9 shows a schematic diagram of two modes setup in equilibrium state. Fig. 4.10 shows the experimental measurements of the two modes' output spectrum when the two modes are in the equilibrium state.

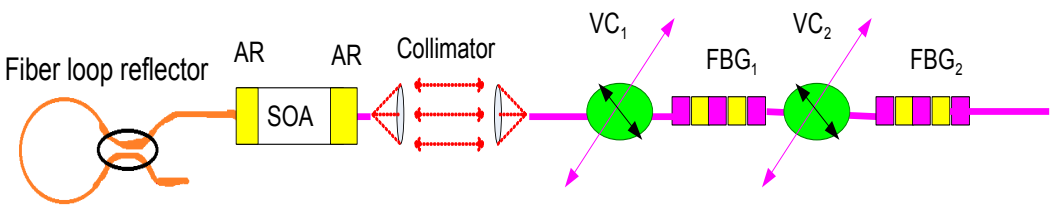

Figure 4.11: Schematic diagram of two modes operation (final laboratory stage). Here SOA is a semiconductor optical amplifier, FBG is a fiber Bragg grating and VC is the variable coupler.

4.2.4 Final Laboratory Stage

In this stage, the final laboratory sensor setup is presented. In order to use ICLAS method, the sample under consideration should be inserted inside the cavity. Therefore the fiber based sensor is opened in order to insert the cell inside the laser cavity. A free propagation two sided collimator is used, which enables coupling the light from the cell into the fiber and vice versa. Fig. 4.11 shows this final laboratory sensor design. Where a free fiber based two sided collimator have been inserted inside the cavity. More details about the collimator design and its working principle can be found in [71].

Chapter 5

RIN Measurements of the Two Modes Sensor

In this chapter, the experimental measurements of the two modes sensor by means of RIN are introduced. This experimental study has two main objectives. The first objective is to study the RIN spectrum behavior with the variation of the two modes' intensities. The second is to study RIN behavior with the variation of the two modes wavelength differences or the modes' positions.

In order to analyze and quantify these objectives, RIN setup is required. Therefore a simple introduction of the RIN setup is introduced. RIN setup consists of an optical receiver and an electronic spectrum analyzer. The optical receiver converts the optical signal to an electrical signal and it consists of fast photodiode, Bias-Tee, and low noise amplifier (LNA). The Bias-Tee is used to separate the direct component (DC) and the alternative component (AC) of the detected photocurrents. The AC component of the electrical signal accounts for the laser intensity fluctuations (noise) while the DC component is proportional to the mean optical intensity. The alternative component (AC) of the detected signal is amplified using the low noise amplifier (LNA) and it is viewed using the electronic spectrum analyzer (ESA).

In order to study the first objective, the intensity of the two modes is varied in expense of each other. This variations are done using the second variable coupler VC_2 within the sensor setup, where the variable coupler works as a variable loss inside the cavity. The intensity ratio of the two modes is considered. For each

intensity ratio, the RIN spectrum is measured. The optical spectrum and its related RIN spectrum are plotted versus the intensities ratio. From the RIN spectrum, a significant tendency between the two modes intensities ratio and the RIN spectrum are observed.

In order to study the second objective, the wavelength difference between the two modes is varied. This variation is achieved by tuning one of the two modes. The tuning procedure is achieved by means of thermal and strain effects of the FBGs. In order to quantify the results, the RIN spectrum is averaged over the frequency range up to 20 GHz. The averaged RIN values are plotted versus the two modes' intensities ratio and wavelength differences respectively. From the averaged RIN spectrum, the following results are achieved.

1. Wavelength tuning has no effect on the RIN spectrum which is very beneficial for the sensor principle.

2. RIN is found to be an excellent indicator for the two modes intensities ratio variations which strongly supports the sensor methodology.

RIN is chosen for monitoring the intensity difference between the two modes to considerably reduce the sensor cost in comparison with the optical read-out.

5.1 Relative Intensity Noise Setup

In order to measure RIN, an optical receiver is required. It is used to convert the optical signal to an electrical signal. In the scope of this work, an optical receiver has been demonstrated using a fast photodiode, a Bias-Tee and a low noise amplifier (LNA). Using this optical receiver and an ESA, RIN has been measured and analyzed.
Fig. 5.1 shows the RIN setup. The emitted light of the two modes sensor is propagated into the fast photodiode. The bandwidth of the fast photodiode is 30 GHz, and it has spectral response range from 950 to 1650 nm.
The detected photocurrents are separated into alternating current (AC) and direct current (DC) by the so-called "Bias-Tee". The AC part of the signal accounts for the fluctuations of the laser intensity (noise), which is amplified by low noise

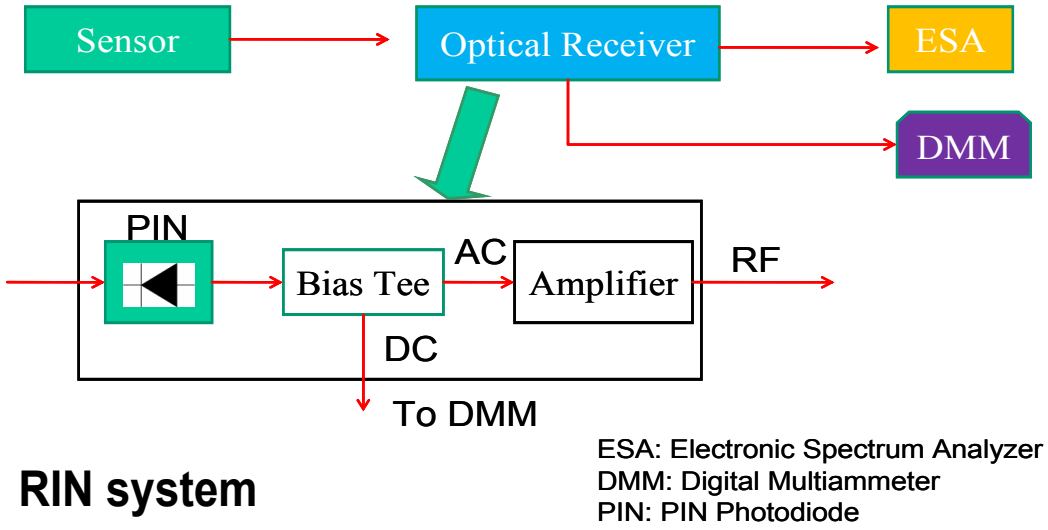

Figure 5.1: Schematic diagram of RIN system used for the measurements. Here, the optical receiver has been shown, which consists of fast photo diode, Bias-Tee, and low noise amplifier (LNA).

amplifier (LNA) and analyzed using ESA.
The DC part of the signal accounts for the photocurrent I_{ph}, which is proportional to the mean optical intensity. As mentioned before, the intensity fluctuations are characterized by RIN, which is defined as the ratio of the mean value of the optical intensity fluctuation δP squared to the mean optical power P_o squared at a specified frequency ω at a 1 Hz bandwidth. This ratio can be expressed as the ratio of the detected electrical powers, and the RIN can be written as:

$$RIN(\omega) = \frac{S_P(\omega)}{B_{res} G I_{ph}^2 R}, \tag{5.1}$$

where the spectral noise power $S_P(\omega)$ is the difference between the measured spectral noise power of the signal of the illuminated detector and the spectral dark noise power at the frequency ω. The mean electrical power of the detected signal is given by $I_{ph}^2 R$, where R is the impedance of the amplifier and I_{ph} is the photodiode current of the detected signal.
The resolution bandwidth B_{res} of the ESA gives the normalization to the 1 Hz

bandwidth, and G accounts for the gain of the LNA. More details of the optical receiver design and its demonstration stages have been presented by [72].

5.1.1 Experimental Measurements

Here, the experimental measurements of the two modes sensor using RIN as an indicator for the variation of the modes' intensities ratio I_1/I_2 and the wavelength difference $\lambda_2 - \lambda_1$ are devoted, where I and λ denote the intensity and the wavelength of the modes respectively. The main objectives in this section are:

1. How the RIN (indicator) is varied with the variation of the two modes' intensities?

2. How the RIN (indicator) is varied with the variation of the modes' wavelength difference or with the two modes' positions?

In order to analyze the answers of the two main objectives, the two modes intensities are varied by suppressing one mode at the expense of the other. This is done by varying the coupling ratio of the second variable coupler VC_2. Fig. 5.2 shows schematic diagram of the experimental setup used for RIN measurements. The two modes have been tuned in the wavelength domain by controlling the temperature of the two FBGs, where an aluminum block has been attached under neath the two FBGs as in Fig. B.1. More details about the tuning of the FBGs is found in appendix B.
The optical spectra has been viewed using an optical spectrum analyzer (OSA). Various optical views states and its related RIN spectra are shown in Figs. 5.3-5.9.
The injection current and the temperature of the SOA are 130 mA and $25C^{\circ}$ respectively. In Fig. 5.3, the FBGs have been tuned systematically resulting in 1.64 nm wavelength difference. The intensity of one mode has been varied at the other one's expense using the variable coupler VC_2. In Fig. 5.3(b), eight optical views for different intensities ratios are shown. It is seen from the related RIN spectrum, when the right mode (long wavelength) intensity decreases in favor of the left mode (short wavelength) RIN decreases rapidly and systematically until the two modes have equal intensities. With further suppression of the right

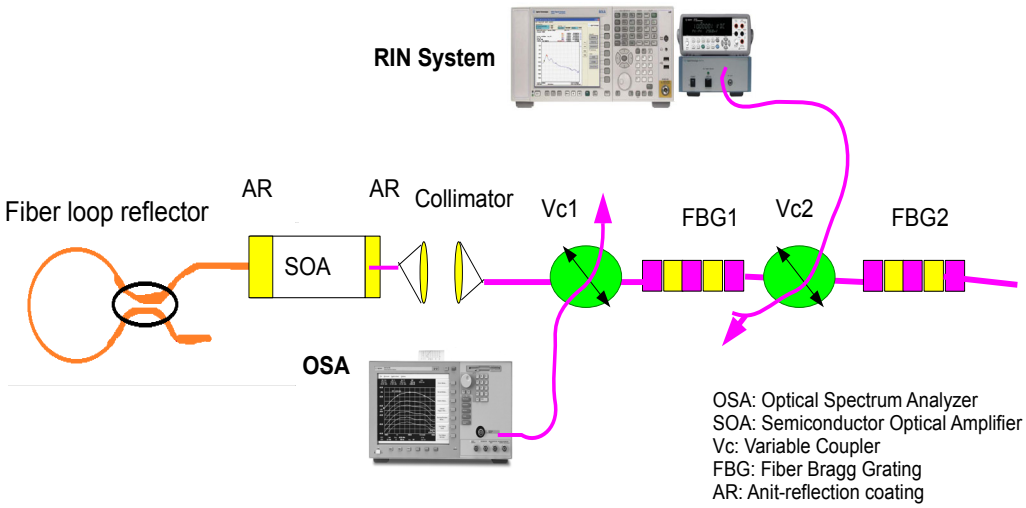

Figure 5.2: Schematic diagram of RIN measurements of two modes' sensor. Here, the two modes' intensities have been varied by varying the coupling ratio of the second variable coupler VC_2 and the two modes have been tuned in the wavelength domain.

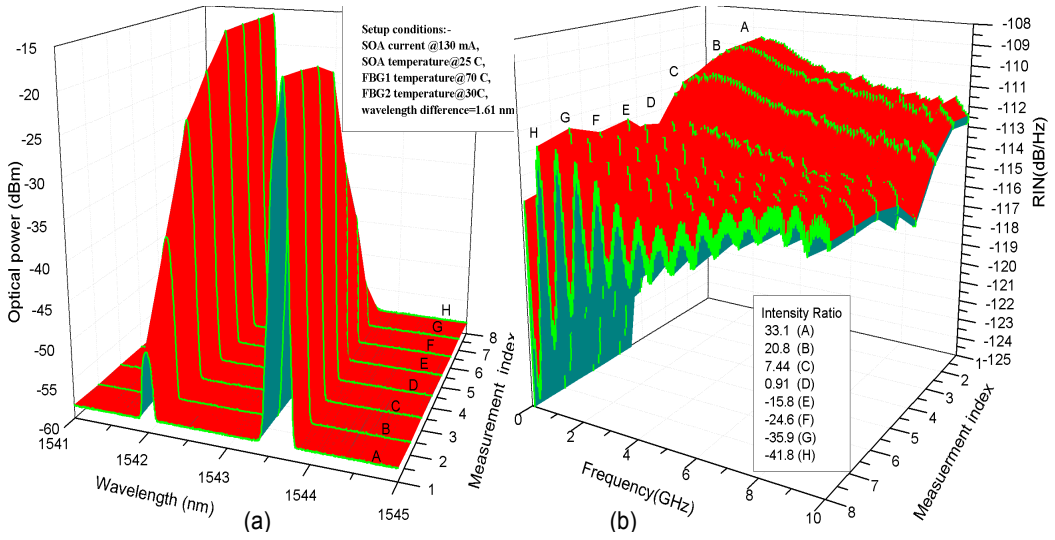

Figure 5.3: 3D plot of two modes sensor. (a) shows the optical spectrum of the two modes of 1.61 nm wavelength difference with different modes intensities. (b) shows the related RIN spectrum over frequency range up to 10 GHz.

mode, RIN decreases and fluctuates strongly in the low frequency region up to 5 GHz. This considerable change in the RIN spectrum shows that the relaxation oscillation frequency (ROF) becomes undamped. This behavior might be due to the laser system entering the unstable chaotic state. The initial RIN spectrum of the two modes' sensor shows that the noise intensity peak at 2.33 GHz, which is the relaxation oscillation frequency (ROF), and it indicates that the relaxation frequency in this curve is damped. While the peak at ROF becomes flat and shifted towards shorter frequencies by 220 MHz to be 2.11 GHz, when the two modes have equal intensities.
With further suppression of the right mode, sharp multiple peaks of ROF appear at 710MHz, 1.39 GHz, 2.13 GHz, 2.8 GHz and 3.5 GHz. The previous behavior has been noticed in Figs. 5.4-5.8 with different wavelength differences and without considerable change in RIN values.
In Fig. 5.9 the two FBGs have been operated at the same wavelengths, where the two modes of identical FWHM and reflectivity overlap perfectly. Therefore, the optical output behaves like a single mode laser. Thus a considerable change in RIN values have been observed. This change occurs due to that mode partition noise takes place in this case.

Now, the variation of the intensity ratio of the two modes and the two modes wavelength difference on the average RIN are studied. To analyze this variation, RIN values have been averaged over 20 GHz frequency range. Fig. 5.10(a) shows the average RIN versus the two modes' intensities ratio for different wavelength differences. It can be seen from Fig. 5.10(a) that the average RIN of the two modes sensor represents an excellent indicator for mode intensities ratio, and it remains constant with the change of modes positions. Therefore it is achieved that the wavelength tuning (position of the mode) has no effect on the average RIN. In Fig. 5.10(b), the average RIN has been plotted versus the two modes' wavelength differences for three different modes intensities states: namely 'equal modes', 'right mode suppressed' and 'left mode suppressed'. Fig. 5.10(b) shows these various states with different wavelength differences. From this figure it is confirmed that during the tuning process the averaged values of RIN remain unchanged. This result is very important for the sensor principle because it allow

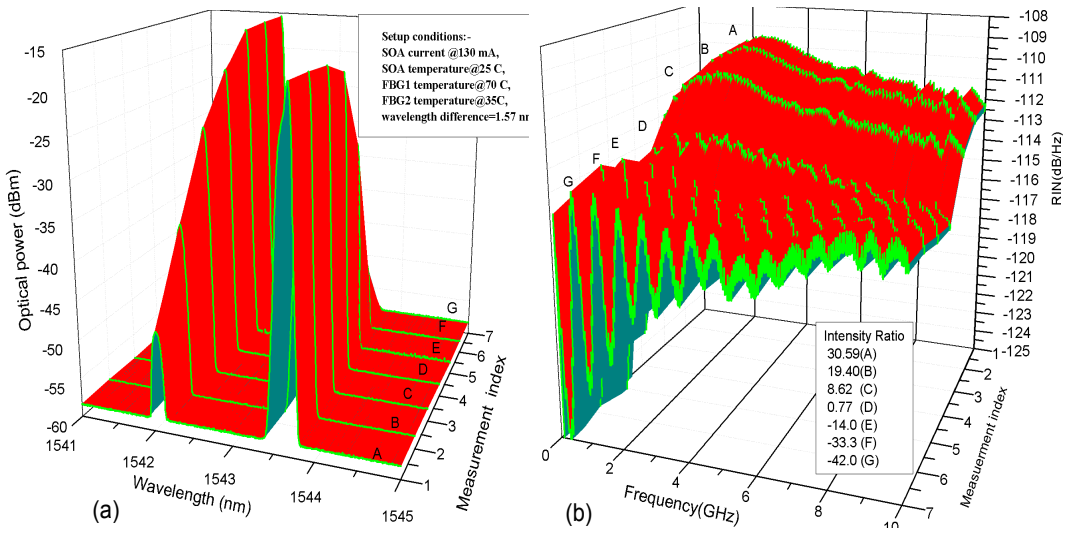

Figure 5.4: 3D plot of two modes sensor. (a) shows the optical spectrum of the two modes of 1.57 nm wavelength difference with different modes intensities.(b) shows the related RIN spectrum over frequency range up to 10 GHz.

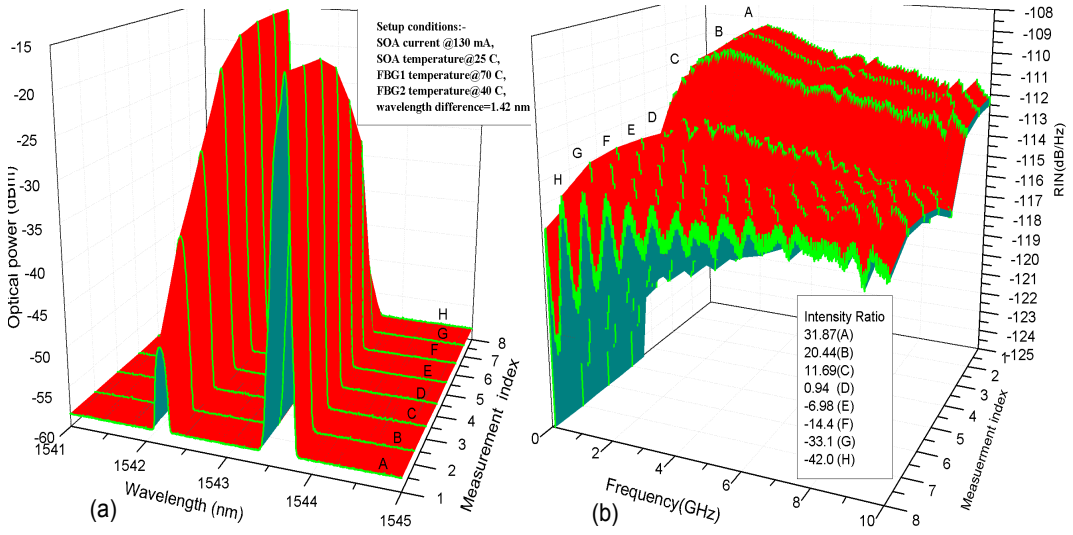

Figure 5.5: 3D plot of two modes sensor. (a) shows the optical spectrum of the two modes of 1.42 nm wavelength difference with different modes intensities. (b) shows the related RIN spectrum over frequency range up to 10 GHz.

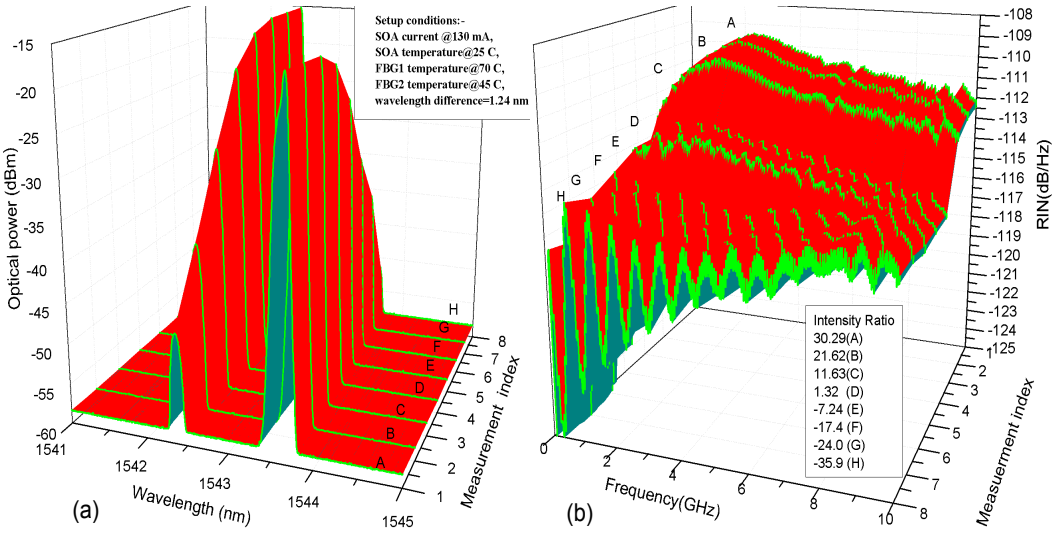

Figure 5.6: 3D plot of two modes sensor. (a) shows the optical spectrum of the two modes of 1.24 nm wavelength difference with different modes intensities. (b) shows the related RIN spectrum over frequency range up to 10 GHz.

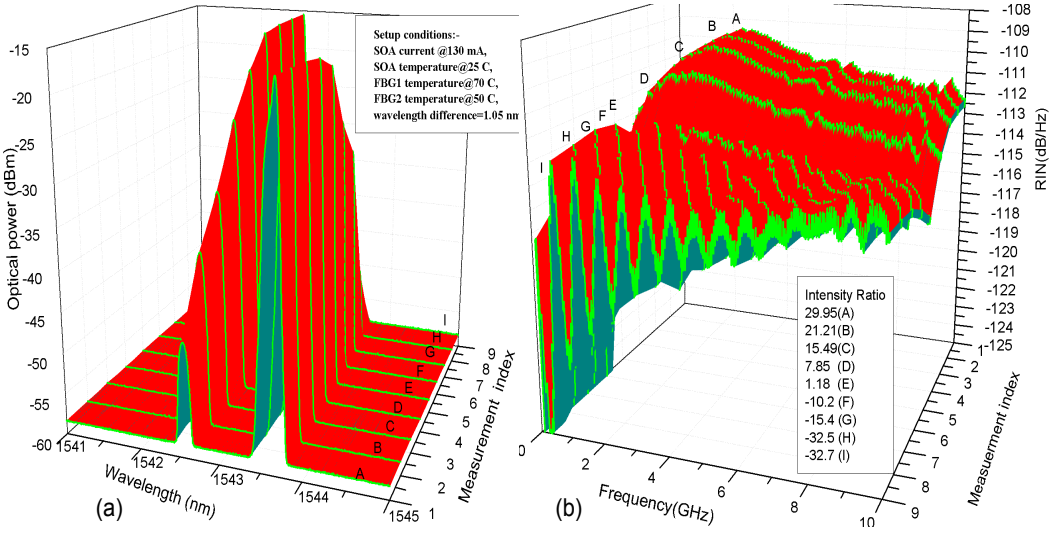

Figure 5.7: 3D plot of two modes sensor. (a) shows the optical spectrum of the two modes of 1.05 nm wavelength difference with different modes intensities. (b) shows the related RIN spectrum over frequency range up to 10 GHz.

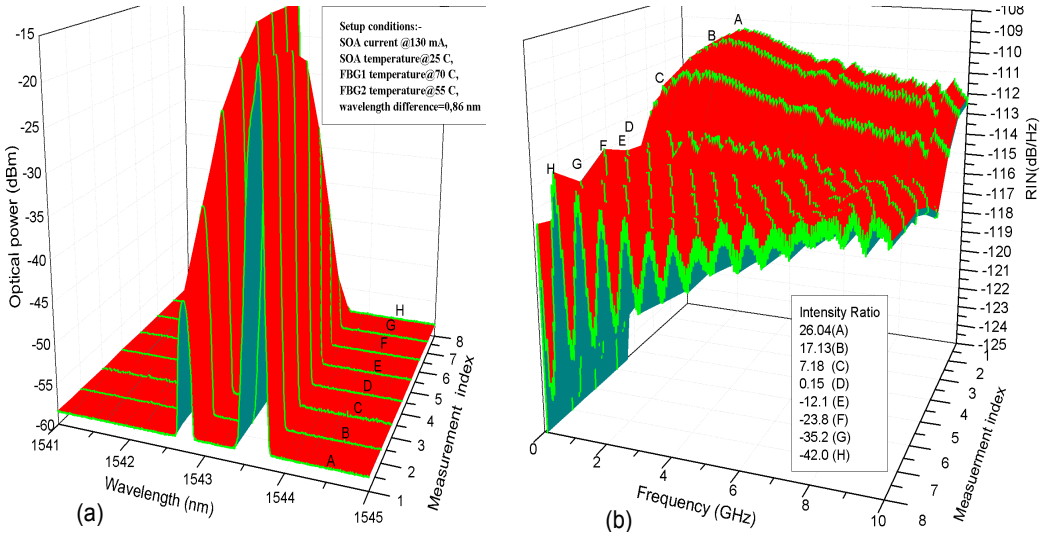

Figure 5.8: 3D plot of two modes sensor. (a) shows the optical spectrum of the two modes of 0.86 nm wavelength difference with different modes intensities. (b) shows the related RIN spectrum over frequency range up to 10 GHz.

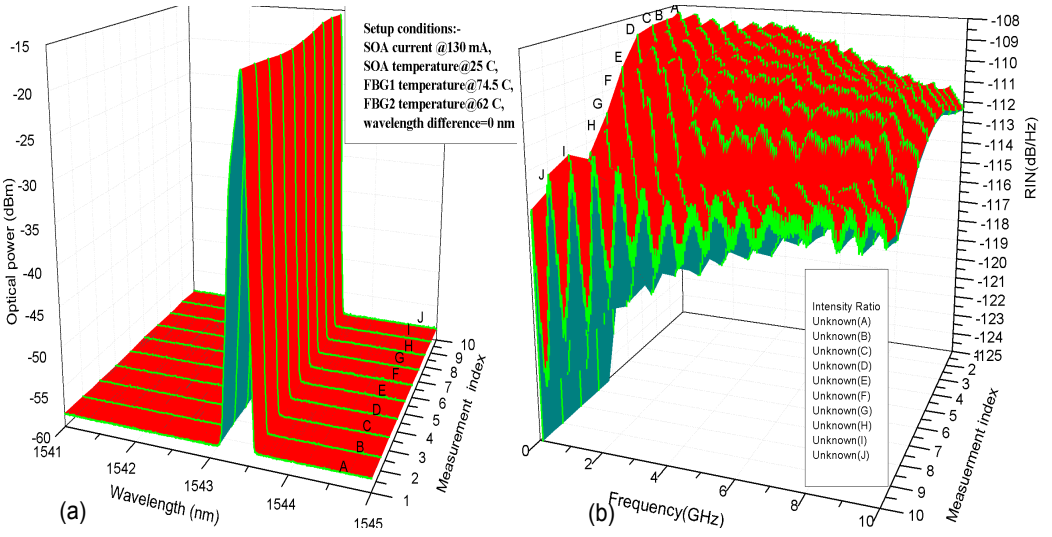

Figure 5.9: 3D plot of two modes sensor. (a) shows the optical spectrum of the two modes when two modes are completely overlapped. (b) shows the related RIN spectrum over frequency range up to 10 GHz.

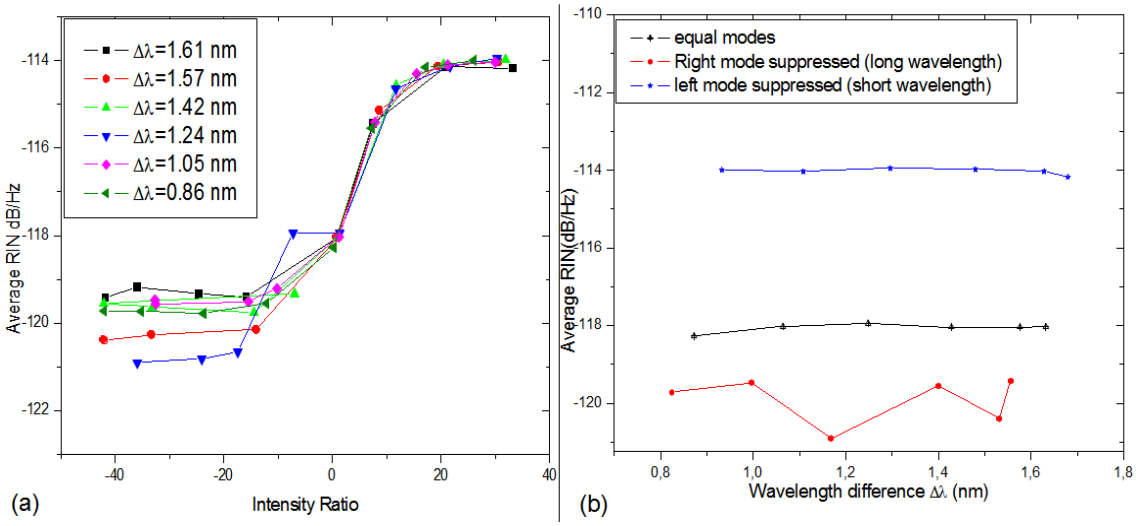

Figure 5.10: Average RIN versus (a) intensity ratio for different wavelength difference. (b) wavelength difference at 130 mA in three different states 'equal modes', 'left mode suppressed', and 'right mode suppressed'.

us to choose any wavelength position for lasing modes without effect on RIN spectrum. Now these results are concluded as follows:

1. The experimental results of RIN characteristics as well as the average RIN dependence of the two modes sensor on the two modes' intensities ratio and wavelength differences are reported. From the experimental results, it is found that wavelength tuning has no effect on average RIN and RIN has been found as an excellent indicator for intensity ratio variation.

2. The two modes' sensor response has been indicated using RIN value, an electrical parameter, which is significantly less expensive and easy interpolated in comparison to the optical readout.

3. Several units of this two modes'sensor can be combined to create large sensing systems or sensor arrays and thereby increase the detection range.

Chapter 6

Propofol Measurements Using the Two Modes Sensor

In this chapter, the two modes' sensor is used to measure propofol. The highly sensitive intracavity laser absorption spectroscopic method is considered, where propofol cell is inserted inside the sensor cavity. RIN is chosen to monitor the sensor response. Propofol is dissolved in various solvents and in cells of various sizes. In each measurement, the optical output and its related RIN spectrum are viewed and analyzed. The optical output spectrum is normalized and plotted versus propofol molarities. The normalized mode intensity shows that the intensity of the mode decreases with increasing of propofol molarity until a critical point is reached. The critical point is the point which distinguishes between 'no mode competition' and 'mode competition' regimes. With further increasing of propofol molarity, the slope of selected mode intensity becomes steeper. The sensor sensitivity is extracted from the optical view by calculating the abrupt change in the slope before and after the critical point. The maximum sensor sensitivity is achieved when the sensor operates beyond its critical point because of the mode competition effect. The related RIN is plotted versus propofol molarity. It is observed that RIN spectrum decreases with increasing the propofol molarities until the selected mode reaches the critical point. At this critical point the mode partition noise takes place, where the RIN value denoted by the critical point, is increased from its previous value. However the total RIN behavior shows a

systematic decrease with increasing propofol molarity. The RIN spectrum is averaged over the whole frequency range and plotted versus propofol molarity. It is achieved that RIN represents an excellent indicator for two modes' sensor and the sensor sensitivity reaches order of 10^3 in comparison with the conventional spectroscopic method due to the competition between the two modes.

6.1 Propofol

Propofol (2,6-diisopropylphenol) is a highly effective and commonly used injectable anesthetic for the creation and maintenance of sedation [73]. It is non-barbiturate and short-acting. Since it has minimal solubility in water, injectable formulations exist as emulsions. Propofol is an intravenous sedative that is administered continuously to a wide variety of critically ill patients, including those having coronary artery bypass grafts, adult respiratory distress syndrome, asthma, head trauma, status epileptics, pneumonia, and sepsis [74].

The current commercial propofol formulations are oil in H_2O emulsions consist-

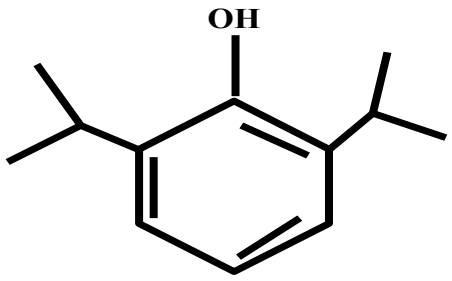

Figure 6.1: Structure of propofol.

ing of propofol (1%, 10 mg/mL), soybean oil (100 mg/mL), egg yolk lecithin (12 mg/mL), and glycerol (22.5 mg/mL) in H_2O.

Commercial formulations of propofol include emulsions which were introduced into the market under the name of Diprivan (AstraZeneca) and 1% propofol injectable emulsion (Baxter). Fig. 6.1 shows the chemical structure diagram of propofol. It has O-H fundamental stretching vibration of phenols unsubstituted or sometimes substituted by n-alkyl group solutions.

6.1.1 Propofol Preparations

As an alternative to an emulsion, propofol has been dissolved in 2-Propanol, Acetone, Dichloromethane (DCM) and soybean oil. Lists of these solvents with their structural diagram, refractive index and dielectric constant have been tabulated in [71].

Fig. 6.2 shows the absorption coefficient of propofol versus wavelength, measured

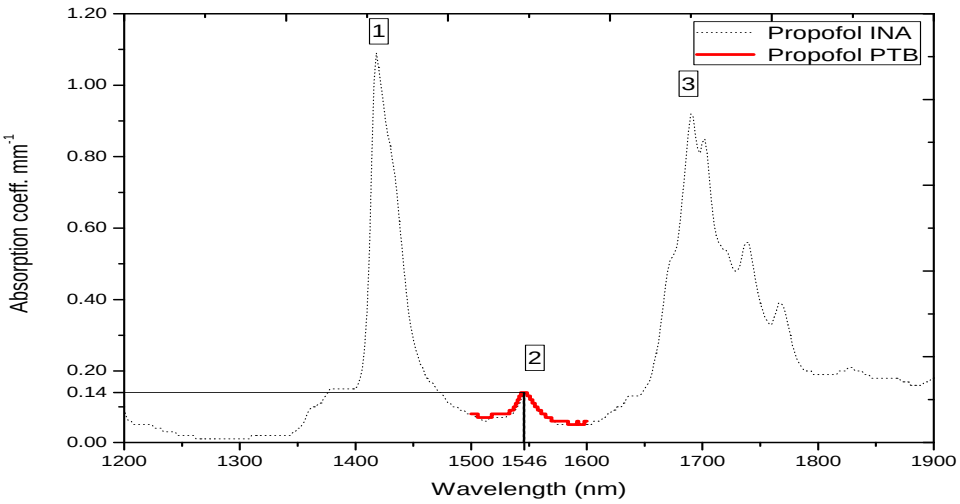

Figure 6.2: Absorption spectrum of propofol versus wavelength. Dot black line shows absorption lines measured at INA. Solid red line shows the absorption line measured at Die Physikalisch-Technische Bundesanstalt (PTB) between $1500-1600\ nm$. Here detection of the minor peak, which is marked in the figure as Nr. 2, is interested

by an NIR spectrophotometer (Perkin Elmer Lambda 900) [75, 71].

In Fig. 6.2, two major peaks around 1420 and 1700 nm and one minor peak around 1550 have been observed. For several reasons such as laser sources and water lines overlapping with the major peaks of propofol, Detection of the minor peak, which it lies around at C-band of telecommunication range is interested.

In Fig. 6.2 the absorption coefficient of the minor peak (peak 2)of propofol is highlighted, whose maximum lies at 1546 nm with absorption coefficient 0.14 (mm^{-1}) and FWHM of 20 nm.

6.2 Sample Cell Preparations

Propofol used for the measurements is delivered in a 100 ml bulk container. It is opened under nitrogen atmosphere and its contents split up, sealed and stored in many small containers holding about 2 ml each at $4°C$, where propofol is in a solid phase. Soybean oil is delivered in a sealed 50 ml container, in which it is kept at $4°C$ for about three days before the measurements.
2-Propanol, Acetone and Dichloromethane (DCM) are readily available in large quantities and high purities at our institute (INA). For the measurements presented in this section 100 ml bottles have been used. All substances are taken out of cooling and left to adjust to room temperature several hours before beginning of the measurements. The sample cell used is thoroughly rinsed with 2-Propanol and dried with gaseous nitrogen multiple times before each measurement to remove any remnants of the substances it previously contained.
More details about the preparation of chemical solvents and their absorption spectra have been introduced by [71].
The actual measurements are carried out at room temperature with stabilized FBG heating system. To initialize each measurement, the following steps have been involved:

1. The sample cell is cleaned as described above, introduced into the collimator at an angle of one degree towards normal incidence, filled with an initial amount of solvent and closed to avoid evaporation.

2. Current is applied to the SOA and the optical and electrical output spectra are observed using the OSA and ESA.

3. The two modes have been equalized by adjusting the variable couplers.

4. The initial output spectrum in this equalized state is saved as an initial point.

5. The laser source is turned off and the cell cover removed for propofol injection.

6. The propofol sample has been merged with the solvent many times to ensure a homogeneous solution in the cell.

7. The optical and electrical spectra are saved again.

Steps 5 through 7 are repeated for each increase of propofol concentration until the optical output spectra do not show any significant change anymore.

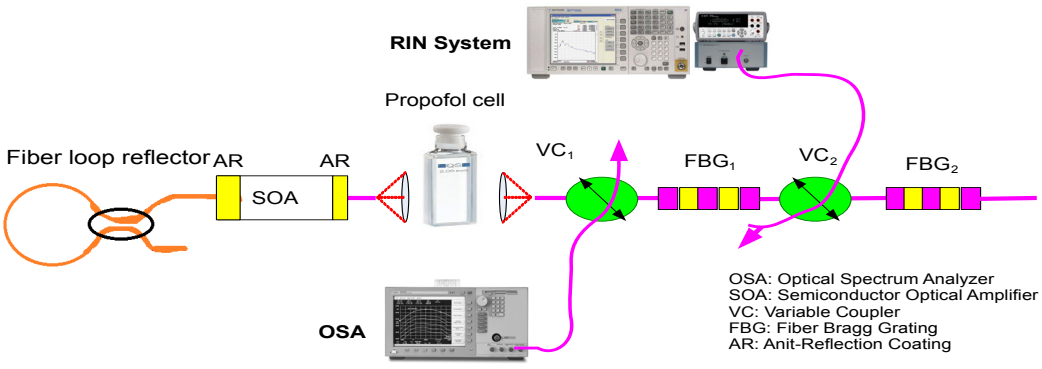

Figure 6.3: Schematic diagram of RIN measurements of two modes ICLAS sensor. Here, the propofol cell has been inserted inside the cavity. The propofol molarity has been increased for each measurements steps.

6.3 Results and Discussions

In this section, the experimental results of propofol, which have been measured using the two modes ICLAS sensor are shown.
In the following agenda an overview of the measurements procedure is given:

1. Propofol has been merged in various solvents and in cells of various sizes.

2. Propofol concentrations have been increased systematically until the optical output spectrum does not show any significant change anymore.

3. Propofol has been measured at two different wavelength differences between the two modes (1 nm and 0.5 nm).

4. The optical output spectrum has been measured using an OSA, and the related RIN has been measured using the RIN setup with an ESA described in chapter 5.

Fig. 6.3 shows schematic diagram of the RIN measurements of two modes ICLAS sensor, where propofol cell has been inserted inside the cavity, and the propofol concentration has been increased for each measurements step. Table 6.1 shows these measurements steps. Various optical spectrum of propofol measurements

Figure Index	**Solvent**	**Sol. Vol. /Cell Size**	**Laser Current**	$\Delta\ \lambda$
Fig.6.4	Acetone	0.75 ml/5 mm	110 mA	1 nm
Fig.6.5	Acetone	1.0 ml/5 mm	125 mA	1 nm
Fig.6.6	Dichloromethane	1.0 ml/5 mm	125 mA	1 nm
Fig.6.7	Acetone	2.0 ml/10 mm	125 mA	1 nm
Fig.6.8	Dichloromethane	2.0 ml/10 mm	160 mA	1 nm
Fig.6.9	Acetone	1.0 ml/5 mm	125 mA	0.5 nm
Fig.6.10	Dichloromethane	1.0 ml/5 mm	125 mA	0.5 nm
Fig.6.11	Acetone	2.0 ml/10 mm	125 mA	0.5 nm
Fig.6.12	Dichloromethane	2.0 ml/10 mm	125 mA	0.5 nm

Table 6.1: Overview of the propofol measurements taken in different conditions

in different conditions are plotted in Figs. 6.4-6.12. In each figure, the optical spectrum has been normalized to show the behavior of the selected mode which suffer from propofol absorption line.
An abrupt change in the slope of the selected mode intensity has been observed, and it is indicated by 'critical point'. This critical point distinguishes between two regimes. In the first regime, the selected mode oscillates independently and no mode competition exists. While in the second regime, the second laser mode begins to compete the selected mode. Therefore, the mode competition effect takes place, and the system sensitivity is increased due to this effect.
These results can be summarized as follows:

1. The intensity of the selected mode exhibits critical point which account for the mode competition effect.

2. The abrupt change in the slope of the intensity of the selected mode gives important information about the sensor sensitivity.

3. To achieve maximum sensitivity of the two modes' sensor, the sensor should be operated beyond the critical point where the mode competition exists.

More theoretical details and comparison between the experimental and theoretical results have been discussed in chapter 3.

Considering the RIN spectrum, it is observed that RIN spectrum decreases with increasing propofol molarity until the selected mode reaches its critical point. At this critical point the mode partition noise takes place, and the RIN value denoted by the critical point has been increased from its previous value, however the total RIN behavior shows a systematic decrease with increasing propofol molarity.
In some cases, multiple critical points have been observed, which results from that the side modes begin oscillate too.
To analyze these results in more details, the RIN spectrum has been averaged over the whole frequency range and plotted against the propofol molarity. Fig. 6.13(b) shows average RIN value versus propofol molarity, and in the same figure, the photodiode current has been plotted.
it can be seen that, the average RIN value decreases systematically with increasing the propofol concentration until a critical point is reached, which shows abrupt change in the slope.
In the same figure Fig. 6.13(a) the average RIN value has been plotted versus the two modes' intensities ratio, and the same behavior has been observed.
In order to calculate the sensor sensitivity, the normalized intensity of the selected mode has been plotted versus the propofol molarity in Fig. 6.14. The sensitivity enhancement factor has been calculated from the abrupt change in the slope of the normalized intensity of the selected mode. The sensitivity enhancement factor has been found to be in order of 10^4 in comparison to the conventional absorption

spectroscopic methods. In order to calculate the minimum measurable intracavity absorbance the following relation has been considered as [76],

$$A_{intra} = (N/S)/\zeta, \tag{6.1}$$

where A_{intra} is the intracavity absorbance (loss), S/N is the signal to noise ratio and ζ is the sensitivity enhancement factor. Substituting $\zeta = 0.17\text{x}10^{4}$, and for the determined signal to noise ratio $S/N = 50$, it is found that the minimum intracavity absorbance $A_{intra} = 8\text{x}10^{-5}$, which it is in a good agreement with the calculation done with Beer Lambert law by [71].

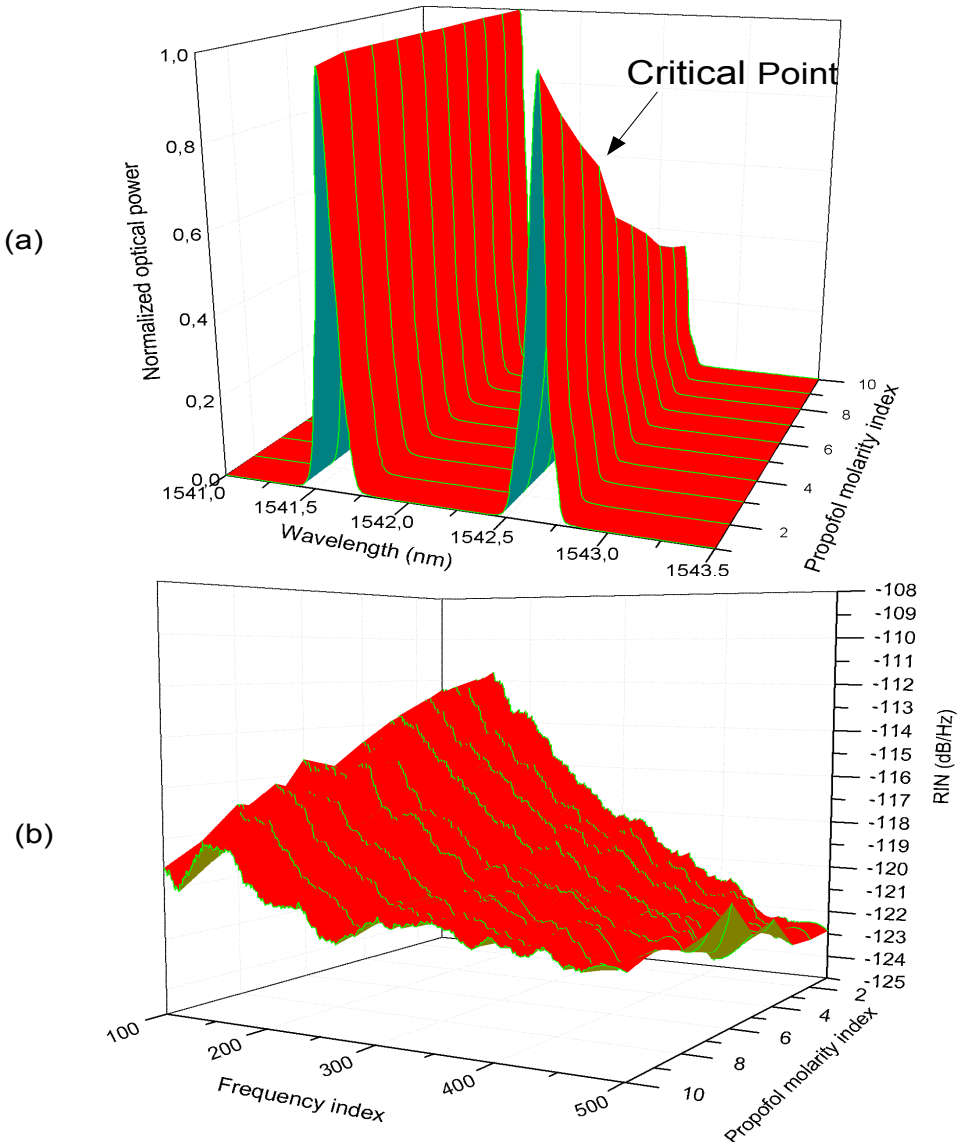

Figure 6.4: 3D plot of propofol measurements using two modes ICLAS sensor. (a) shows the normalized optical spectrum of the two modes ICLAS versus wavelength with increasing the propofol concentration (Molarity). (b) shows the related RIN (dB/Hz) spectrum versus frequency with increasing the propofol molarity. Here, Acetone is used as a solvent, the wavelength difference is 1 nm, the acetone volume is 0.75 ml, the cell size is 5 mm, and the laser current is 110 mA

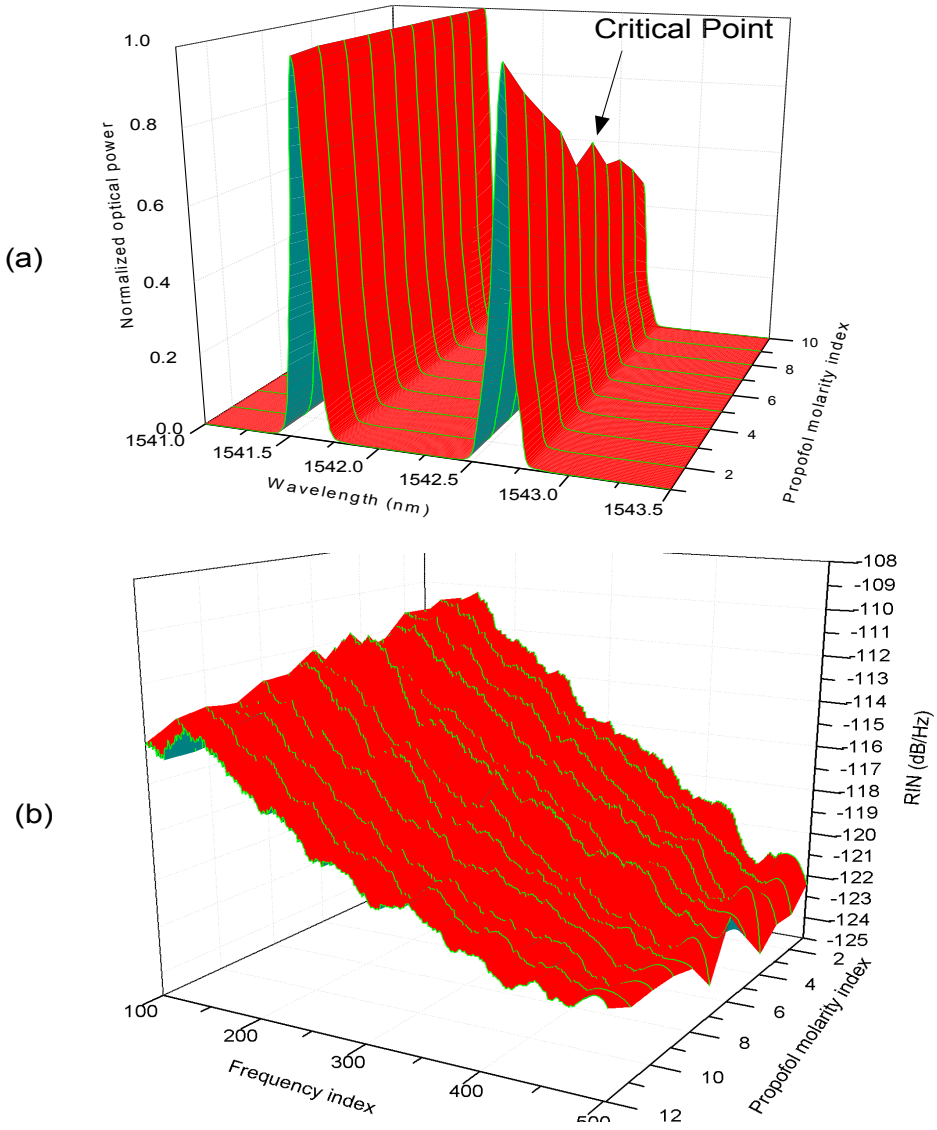

Figure 6.5: 3D plot of propofol measurements using two modes ICLAS sensor. (a) shows the normalized optical spectrum of the two modes ICLAS versus wavelength with increasing the propofol concentration (Molarity). (b) shows the related RIN (dB/Hz) spectrum versus frequency with increasing the propofol molarity. Here, Acetone is used as a solvent, the wavelength difference is 1 nm, the acetone volume is 1 ml, the cell size is 5 mm, and the laser current is 125 mA

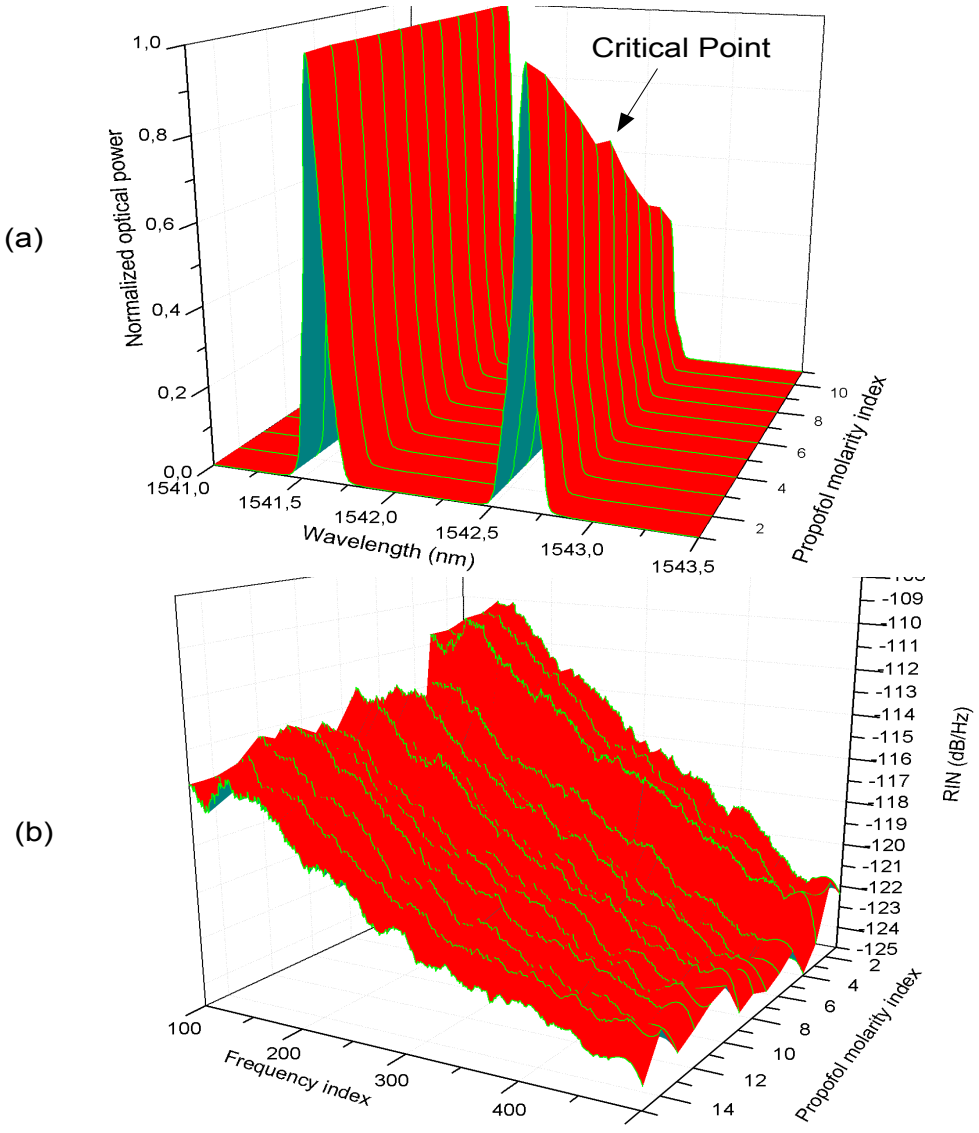

Figure 6.6: 3D plot of propofol measurements using two modes ICLAS sensor. (a) shows the normalized optical spectrum of the two modes ICLAS versus wavelength with increasing the propofol concentration (Molarity). (b) shows the related RIN (dB/Hz) spectrum versus frequency with increasing the propofol molarity. Here, Dichloromethane (DCM) is used as a solvent, the wavelength difference is 1 nm, the Dichloromethane (DCM) volume is 1 ml, the cell size is 5 mm, and the laser current is 125 mA

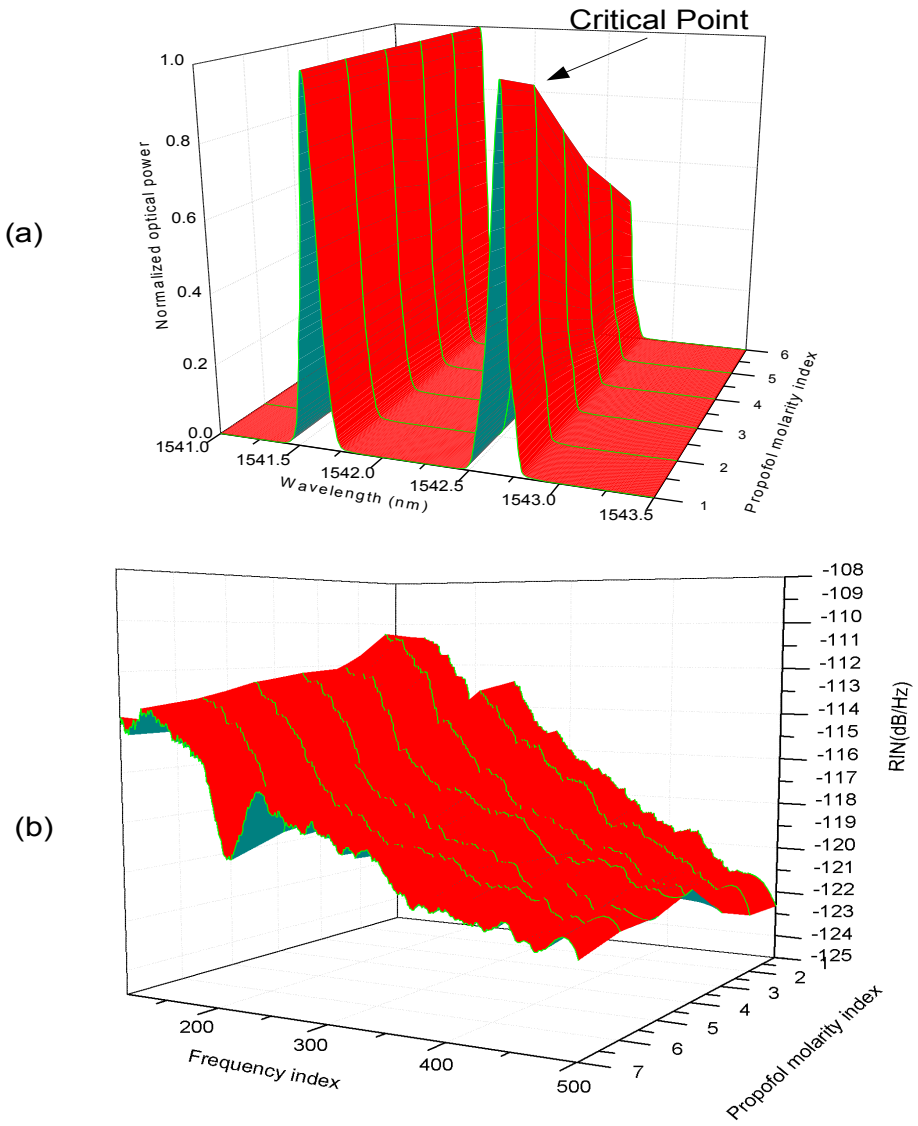

Figure 6.7: 3D plot of propofol measurements using two modes ICLAS sensor. (a) shows the normalized optical spectrum of the two modes ICLAS versus wavelength with increasing the propofol concentration (Molarity). (b) shows the related RIN (dB/Hz) spectrum versus frequency with increasing the propofol molarity. Here, Acetone is used as a solvent, the wavelength difference is 1 nm, the acetone volume is 2 ml, the cell size is 10 mm, and the laser current is 125 mA. Also, one can see a significant dip in the RIN spectrum which results from the cell size.

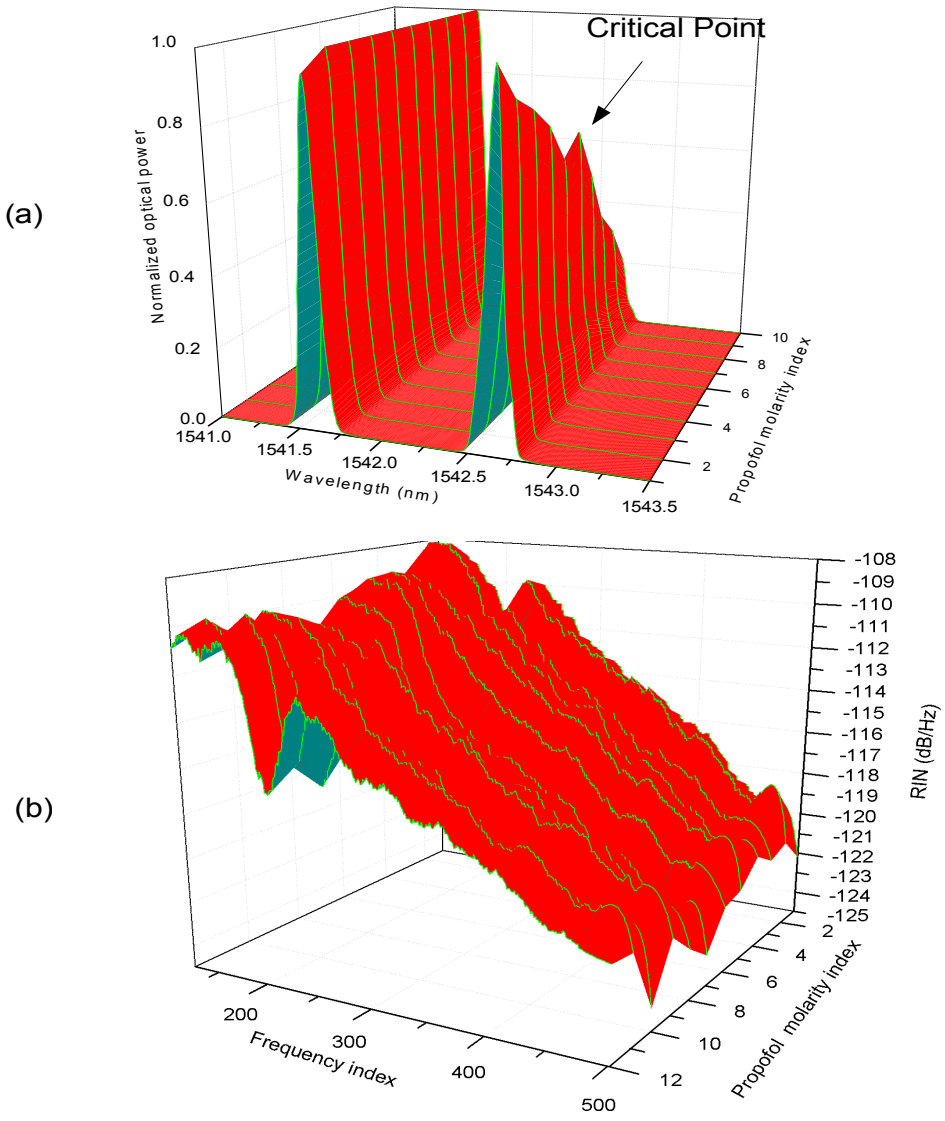

Figure 6.8: 3D plot of propofol measurements using two modes ICLAS sensor. (a) shows the normalized optical spectrum of the two modes ICLAS versus wavelength with increasing the propofol concentration (Molarity). (b) shows the related RIN (dB/Hz) spectrum versus frequency with increasing the propofol molarity. Here, Dichloromethane (DCM) is used as a solvent, the wavelength difference is 1 nm, the Dichloromethane (DCM) volume is 2 ml, the cell size is 10 mm, and the laser current is 160 mA. Also, one can see a significant dip in the RIN spectrum which results from the cell size.

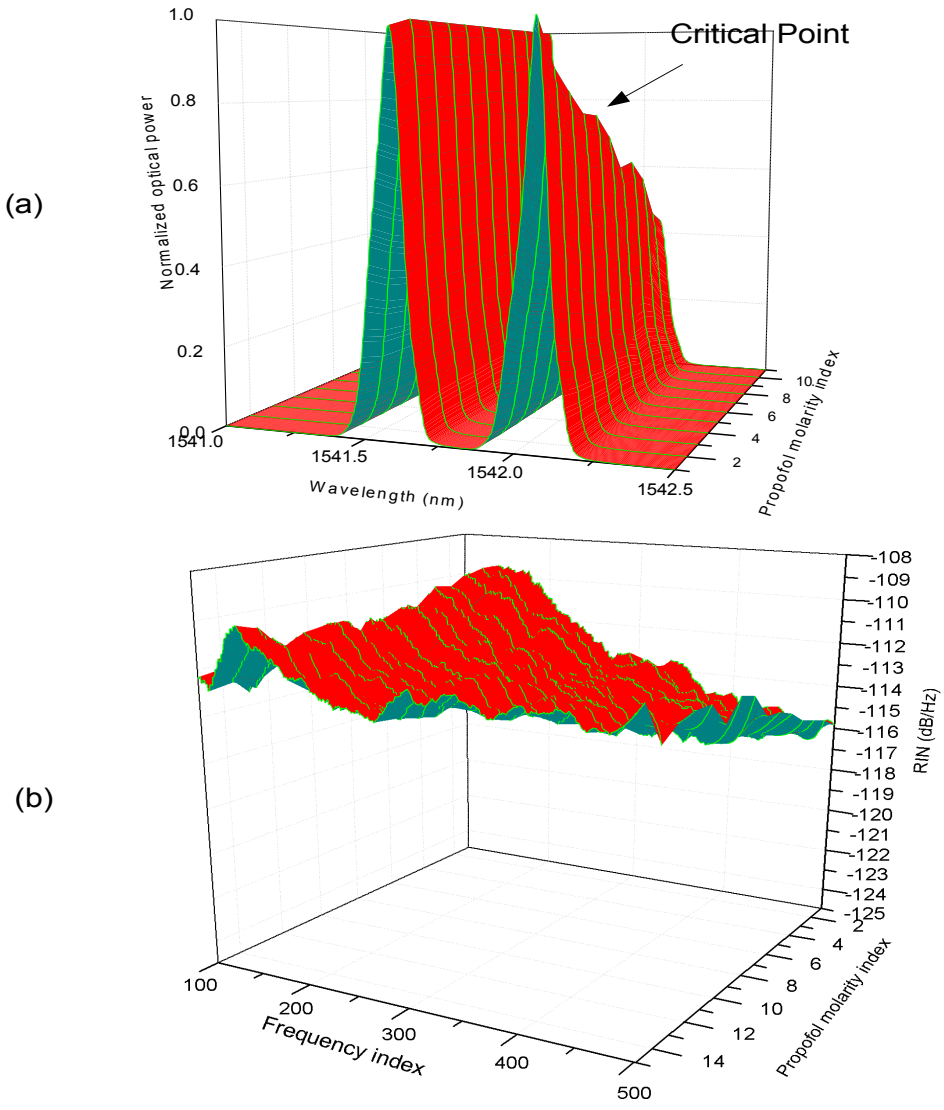

Figure 6.9: 3D plot of propofol measurements using two modes ICLAS sensor.(a) shows the normalized optical spectrum of the two modes ICLAS versus wavelength with increasing the propofol concentration (Molarity). (b) shows the related RIN (dB/Hz) spectrum versus frequency with increasing the propofol molarity. Here, Acetone is used as a solvent, the wavelength difference is 0.5 nm, the acetone volume is 1 ml, the cell size is 5 mm, and the laser current is 125 mA

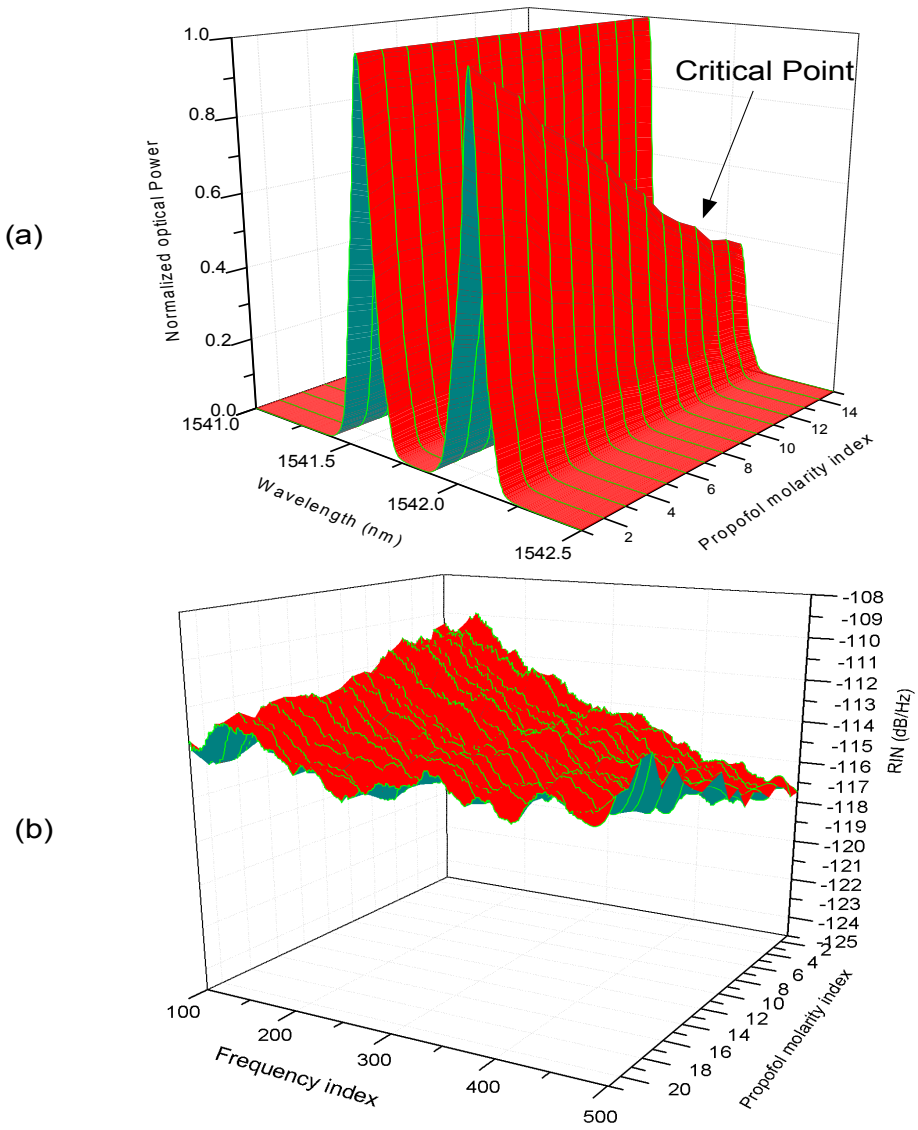

Figure 6.10: 3D plot of propofol measurements using two modes ICLAS sensor. (a) shows the normalized optical spectrum of the two modes ICLAS versus wavelength with increasing the propofol concentration (Molarity). (b) shows the related RIN (dB/Hz) spectrum versus frequency with increasing the propofol molarity. Here, Dichloromethane (DCM) is used as a solvent, the wavelength difference is 0.5 nm, the Dichloromethane (DCM) volume is 1 ml, the cell size is 5 mm, and the laser current is 125 mA

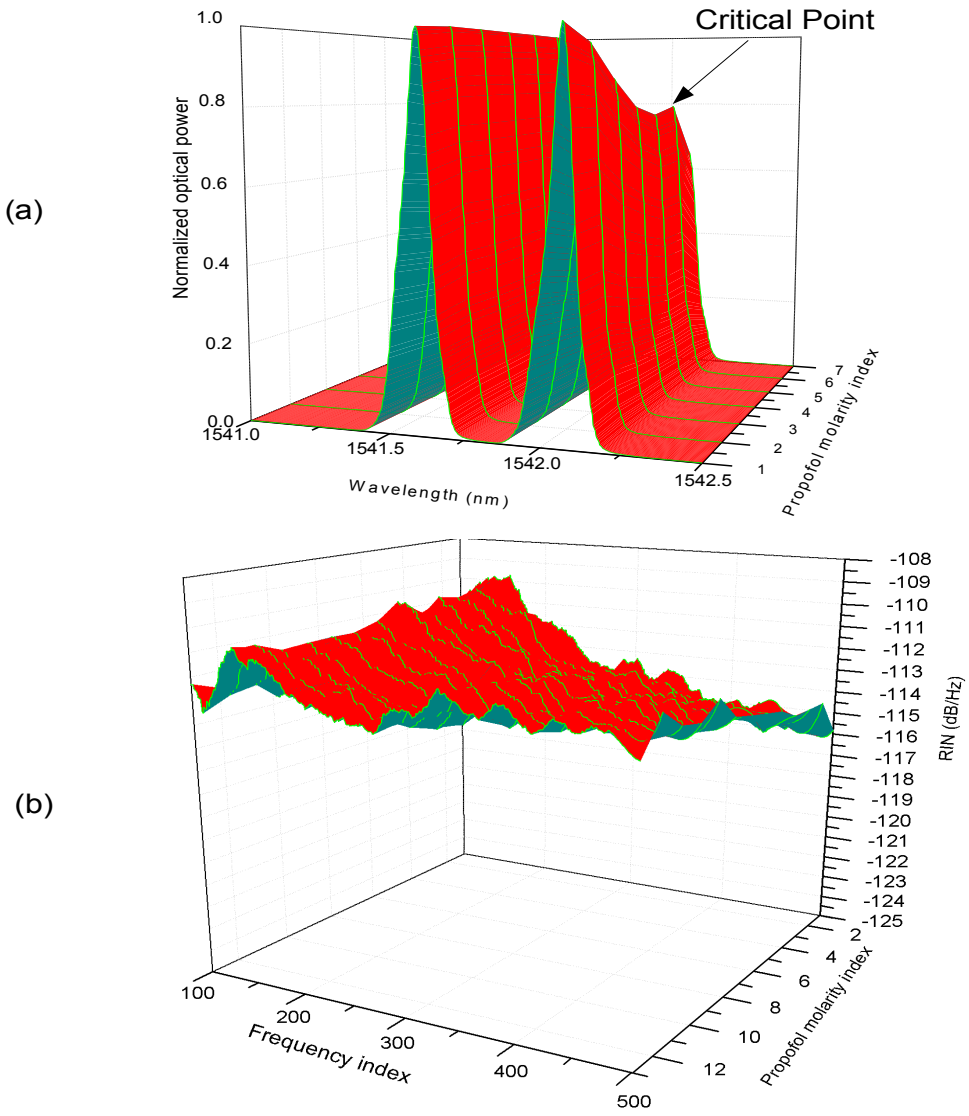

Figure 6.11: 3D plot of propofol measurements using two modes ICLAS sensor. (a) shows the normalized optical spectrum of the two modes ICLAS versus wavelength with increasing the propofol concentration (Molarity). (b) shows the related RIN (dB/Hz) spectrum versus frequency with increasing the propofol molarity. Here, Acetone is used as a solvent, the wavelength difference is 0.5 nm, the acetone volume is 2 ml, the cell size is 10 mm, and the laser current is 125 mA. Also, one can see a significant dip in the RIN spectrum which results from the cell size.

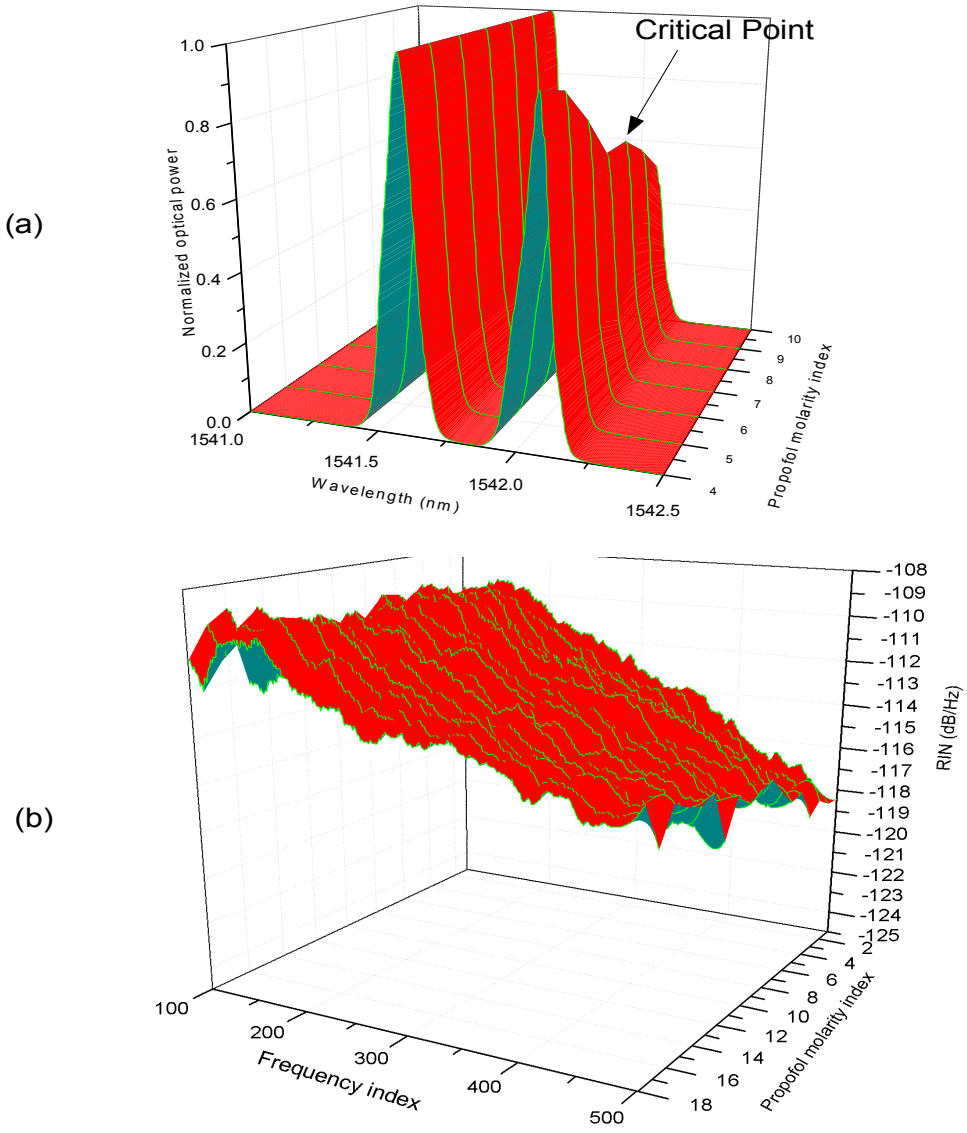

Figure 6.12: 3D plot of propofol measurements using two modes ICLAS sensor. (a) shows the normalized optical spectrum of the two modes ICLAS versus wavelength with increasing the propofol concentration (Molarity). (b) shows the related RIN (dB/Hz) spectrum versus frequency with increasing the propofol molarity. Here, Dichloromethane (DCM) is used as a solvent, the wavelength difference is 0.5 nm, the Dichloromethane (DCM) volume is 2 ml, the cell size is 10 mm, and the laser current is 125 mA.

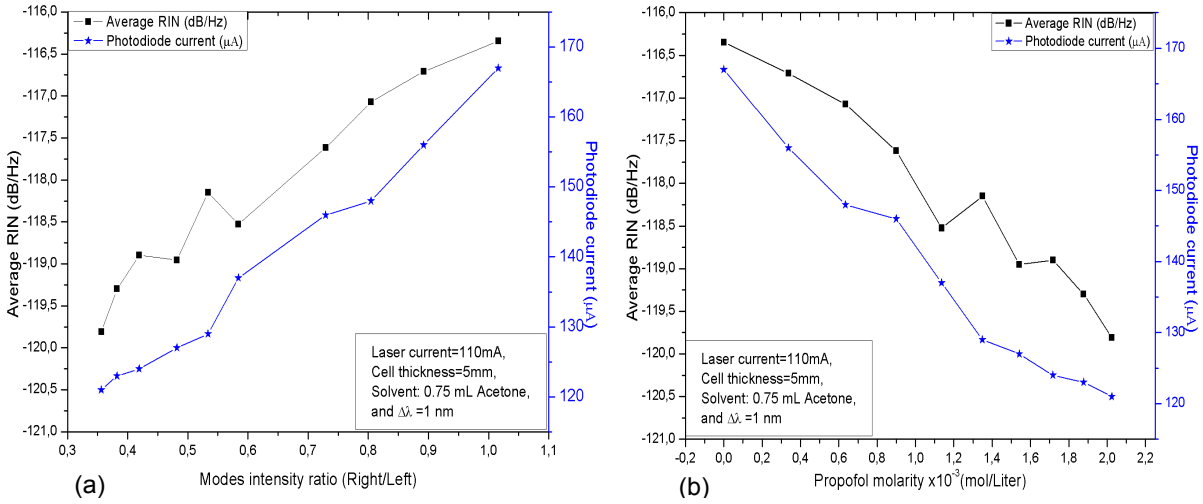

Figure 6.13: Average RIN values and photodiode currents versus (a) modes intensity ratios, and (b) Propofol molarities. The measurements conditions are written in the figure

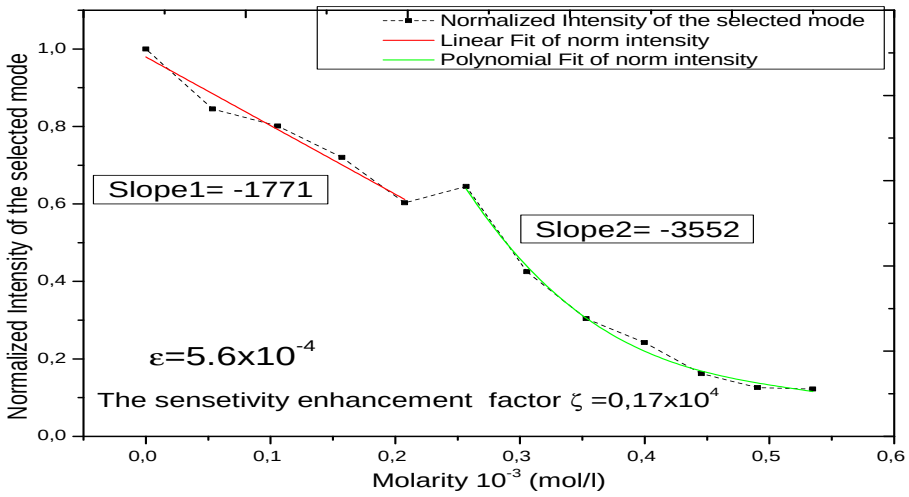

Figure 6.14: Experimental measurements of the intensity of the selected mode versus its loss. Here the sample under consideration is propofol. The sensitivity enhancement factor has been calculated from the abrupt change of the slope between the two regimes.

Chapter 7

Conclusions

In this thesis, a novel two mode semiconductor laser diode sensor based on ICLAS is designed and implemented. Competition between the two mode is used to enhance the sensor sensitivity. The effect of mode competition in ICLAS is discussed analytically. The analytical results show abrupt change in the slope of the selected mode intensity, which occurs due to the mode competition effect. From this abrupt change, the sensitivity enhancement factor is extracted and calculated. Comparison with the experimental measurements shows the same behavior, and the sensitivity enhancement factor is in the order of 10^3 times of the conventional laser spectroscopic methods.

To considerably reduce the sensor cost, RIN is chosen for monitoring the intensity ratio of the two modes instead of optical read-out. The effects of wavelength tunning and intensity of the two modes on RIN are investigated. From the RIN measurements, it is observed that wavelength tuning has no effect on RIN spectra which is very beneficial for the sensor principle. On the other hand, it is discovered that RIN is an excellent indicator for the two mode intensity ratio which strongly support the sensor methodology.

Combining spectral tuning of the two mode across the spectral finger prints of the molecules to be monitored with RIN read-out, it is found that the two mode sensor is highly sensitive and selective.

In order to test the sensor for medical application, the absorption line of an anesthetic sample, propofol, is measured. The optical and its related RIN spectrum are plotted versus propofol molarity. It is observed that the normalized

mode intensity decreases with increase in propofol molarity until its critical point is reached. The critical point is the point which distinguishes between 'no mode competition' and 'mode competition' regimes. The maximum sensitivity of the sensor is achieved when it is operated beyond its critical point because of the mode competition effect.

List of Figures

Appendix A

Relative Intensity Noise

A.1 Relative Intensity Noise of Diode Lasers

Diode laser RIN results from the random carrier and photon recombination and generation processes inherent in the laser. Diode laser RIN usually limits the best sensitivity that can be achieved with absorption spectroscopy but it can be used as an indicator for any system under consideration.

A.1.1 Definition

There are two commonly used definitions of RIN. The first definition is the total RIN over the whole detection bandwidth:

$$RIN = \frac{< \delta P(t)^2 >}{< P(t) >^2}, \tag{A.1}$$

or, expressed in dB,

$$RIN = 10\ log\left(\frac{< \delta P(t)^2 >}{< P(t) >^2}\right) \quad dB \tag{A.2}$$

where, $< \delta P(t)^2 >$ is the mean-square optical power fluctuation, and $< P(t) >$ is the average laser power P_{avg}.
The other definition is the RIN per unit bandwidth:

$$RIN = \frac{S_{sp}}{P_{avg}^2}, \tag{A.3}$$

or, expressed in dB,

$$RIN = 10\ log\left(\frac{S_{sp}}{P_{avg}^2}\right) \quad dB/Hz, \tag{A.4}$$

where S_{sp} is the single -sided spectral density of the total noise power. Mathematically, it is defined as:

$$< \delta P(t)^2 >= \int S_{sp}(f)df. \tag{A.5}$$

This second definition is more popular, and thus is used below. We will find later that there is actually a subtle difference between the actual measured RIN and this widely used definition.

A.1.2 Measurement setup

Fig. A.1 shows the block diagram of RIN setup. The laser diode is operated in cw mode. A broadband photodiode is used to detect the optical input. The AC (noise) and DC (average power) parts are separated, amplified and measured to give RIN.

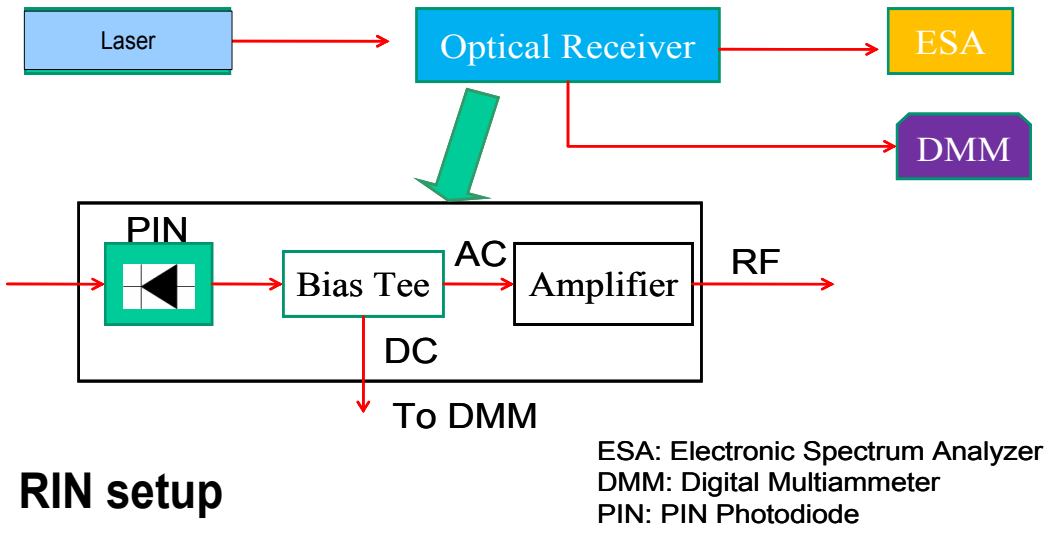

Figure A.1: RIN setup

A.1.3 Theoretical Background

The laser noise can be assumed to originate from the shot noise associated with the discrete random flow of particles into and out of the carrier and photon reservoirs. The Langevin shot noise model can be used to quantify the above shot noise. When we derive the laser dynamics, the current variation is the AC driving source (Eq. (3.18)). By introducing the Langevin noise to the differential rate equations as the AC driving sources for the photon and carrier densities. The laser RIN noise can be derived using standard Fourier analysis:

$$RIN = \frac{S_{sp}}{P_{avg}^2} = \frac{2h\nu}{P_{avg}} \left[\frac{a_1 + a_2\omega^2}{\omega_R^4} |H(\omega)|^2 \right] + \frac{2h\nu}{P_{avg}}, \tag{A.6}$$

where a_1 and a_2 are intrinsic parameters of each laser, ω_R is the laser relaxation oscillation frequency (ROF), and $H(\omega) = \frac{\omega_R^2}{\omega_R^2 - \omega + j\omega\gamma_d}$ is the transfer function. Here γ_d is the damping factor. The term $\frac{2h\nu}{P_{avg}}$ is the quantum noise or shot noise floor. During the detection process, some photons are detected and some are not. This random process generates some partition noise. The noise spectral density of the detected photocurrent with the partition noise contribution is:

$$\delta I_{det}^2(f) = \eta_{det}^2 \left(\frac{e}{h\nu}\right)^2 S_{sp} + 2(1 - \eta_{det}) e I_{det}. \tag{A.7}$$

Here all spectral densities are single -sided, and $I_{det} = \eta_{det}(\frac{e}{h\nu})P_{avg}$. Since the noise is usually measured with an electronic spectrum analyzer (ESA), which generally measures the electrical power of the input signal with dBm/Hz as unit, Eq. A.6 is converted to electrical power by multiplying the load resistance:

$$S_{det}^2(f) = \eta_{det}^2(\frac{e}{h\nu})^2 S_{sp}^2(f) R_{load} + 2(1 - \eta_{det}) q I_{det} R_{load} \tag{A.8}$$

The AC amplifier also adds noise. The performance of the amplifier is usually characterized by noise figure (NF), which is defined as the ratio of the total output noise of the amplifier caused by both the amplifier and the source to the output noise caused by the source alone. Because this ratio depends on the source noise, the source noise is specified to be the available output power ($K_B T$, K_B, is Boltzmann constant, T is absolute temperature) of a resistor at 290 $^\circ K$, i.e. 174 dBm/Hz or 4x10^{-18} mW/Hz. (Note: this definition of noise figure is

widely used, e.g., in commercial noise figure meters; however there are some other versions of definition in the literatures). Therefore, the total noise at the output of the amplifier is:

$$S^2_{total}(f) = G^2\left[\eta^2_{det}(\frac{e}{h\nu})^2 S^2_{sp}(f)R_{load} + 2(1-\eta_{det})qI_{det}R_{load} + NF\right], \quad \text{(A.9)}$$

where G is the amplifier gain. To measure this noise accurately, this total noise should be comparable to or larger than the detection sensitivity of the ESA. That is why the amplifier is used. The maximum amplification is limited by the maximum allowable input of the spectrum analyzer. The DC part of the measurement gives the amplified average signal:

$$P_{avg,elect} = G^2\left[I^2_{det}R_{load}\right]. \quad \text{(A.10)}$$

The ratio of Eqs A.9, and A.10 is defined as RIN_{system}:

$$RIN_{system} = \frac{S_{sp}}{P^2_{avg}} + (1+\eta_{det})\frac{2q}{I_{det}} + \frac{NF(4\times10^{-18})mW/Hz}{I^2_{det}R_{load}}. \quad \text{(A.11)}$$

Substituting Eq. A.6, one easy obtain:

$$RIN_{system} = RIN' + \frac{2h\nu}{P_{avg}} + (1+\eta_{det})\frac{2q}{I_{det}} + \frac{NF(4\times10^{-18})mW/Hz}{I^2_{det}R_{load}}, \quad \text{(A.12)}$$

$$\begin{aligned} RIN_{system} &= RIN' + \frac{2h\nu}{P_{avg}} + (1+\eta_{det})\frac{2q}{I_{det}} + \frac{NF(4\times10^{-18}mW/Hz)}{I^2_{det}R_{load}}, \\ RIN_{system} &= RIN' + \frac{2q}{I_{det}} + \frac{NF(4\times10^{-18}mW/Hz)}{I^2_{det}R_{load}}, \\ RIN_{system} &= RIN' + S_{shot} + S_{thermal}. \end{aligned} \quad \text{(A.13)}$$

Here, $\frac{2q}{I_{det}}$ is recognized as the shot noise of the detector current. The last term represents the amplifier thermal noise.

A.1.4 Measurement Procedure

The laser RIN is obtained by first measuring the RIN_{system} and then subtracting the shot and thermal noise terms:

$$RIN_{laser} = RIN_{system} - S_{shot} - S_{thermal} \quad \text{(A.14)}$$

The thermal noise is measured by blocking the laser beam to the detector (by this way, the noise of the spectrum analyzer is also eliminated in the final measured RIN_{laser}). The shot noise is calculated from its definition $\frac{2q}{I_{det}}$.
Here comes a subtle issue about the laser RIN. Comparing Eq. A.14 with Eq. A.13, we can find that the finally measured laser is actually RIN', i.e., the measured laser RIN is different from the widely used definition $RIN = \frac{S_{sp}}{P_{avg}^2}$. Indeed it is $\frac{S_{sp}}{P_{avg}^2} - \frac{2h\nu}{P_{avg}}$(see Eq. A.4]. Eq. A.14 gives the RIN definition for both RIN measurement and application. This definition is actually easier to use than that defined in Eq. A.4, since the optical shot noise $\frac{2h\nu}{P_{avg}}$ is already included in the electrical shot noise $\frac{2q}{I_{det}}$, which is the sum of the optical shot noise and the detection partition noise [77].

Appendix B

Fiber Bragg Grating Tuning Procedure

B.1 Thermal and Mechanical Effects

The output of the FBG can be tuned by heating the FBGs or/and stretching them uniformly. For this purpose, the FBGs are glued across the top of a U-profile aluminum block Fig. B.1, which are heated uniformly using thermoelectric heaters, creating a temperature distribution in the aluminum blocks. It is well known that the Bragg wavelength λ_B, corresponding to the pitch Λ, is expressed as $\lambda_B = 2n_{eff}\Lambda$, where n_{eff} is the effective refractive index of the fiber. In the case of a FBG mounted on an aluminum block, the shift $\Delta\lambda_B$ in Bragg wavelength with changing strain and temperature can be expressed as [78]:

$$\frac{\Delta\lambda_B}{\lambda_B} = \left(\frac{\Delta n}{n}\right)_m + \left(\frac{\Delta\Lambda}{\Lambda}\right)_m + \left(\frac{\Delta n}{n}\right)_T + \left(\frac{\Delta\Lambda}{\Lambda}\right)_T, \tag{B.1}$$

where,

$$\left(\frac{\Delta n}{n}\right)_m = -\frac{n^2}{2}\left[p_{12} - \nu(p_{11} + p_{12})\right](\alpha_A - \alpha_F)\Delta T, \tag{B.2}$$

$$\left(\frac{\Delta\Lambda}{\Lambda}\right)_m = (\alpha_A - \alpha_F)\Delta T, \tag{B.3}$$

$$\left(\frac{\Delta n}{n}\right)_T = -\frac{n^2}{2}\left[2p_{12}\alpha_F\Delta T + p_{12}\alpha_F\Delta T)\right] + \xi\Delta T, \tag{B.4}$$

$$\left(\frac{\Delta\Lambda}{\Lambda}\right)_T = \alpha_F\Delta T, \tag{B.5}$$

where α_F, α_A, and ξ are the thermal expansion coefficient of the optical fiber, the thermal expansion coefficient of the aluminum plate and the thermo-optic coefficient of the optical fiber, respectively. p_{12} and p_{11} are the components of the strain-optic tensor and ξ is the Poisson's ratio of the optical fiber. The first two terms in Eq. B.1 represent the effect of the mechanical strain on the Bragg grating fiber whereas the last two terms represent the effect of the temperature variations.

If there is a difference in the expansion between the aluminum plate and the FBG due to temperature change (that is, $(\alpha_F \neq \alpha_A)$, then the FBG subject to an additional mechanical strain $(\alpha_F - \alpha_A)\Delta T$, substitute these expression into the Eq. B.1 leads to:

$$\frac{\Delta\lambda_B}{\lambda_B} = (1 - p_e)(\alpha_F - \alpha_A)\Delta T + \left[\left(1 - \frac{n^2}{2}(2P_{11} + p_{12})\alpha_F + \xi\right)\right]\Delta T, \qquad \text{(B.6)}$$

where p_e is the strain-optic coefficient given by:

$$p_e = [p_{12} - \nu(p_{11} + p_{12})] \approx 0.22. \qquad \text{(B.7)}$$

Model calculations of the center wavelengths during the tuning process using Eq. B.1 are plotted in Fig. B.2. They return an expected tuning efficiency of 0.041 nm/°C, which is slightly higher than the response of 0.034 nm/°C observed in measurement. This difference results from that the elasticity of the glue used to attach the fiber to the aluminum profile is not considered.

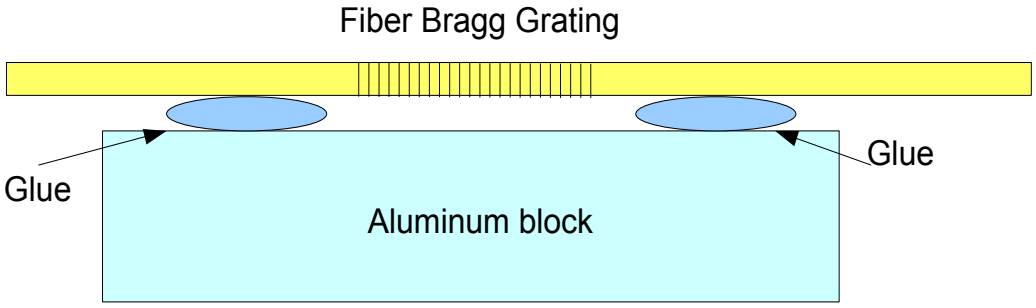

Figure B.1: Fiber Bragg grating tuning mechanism

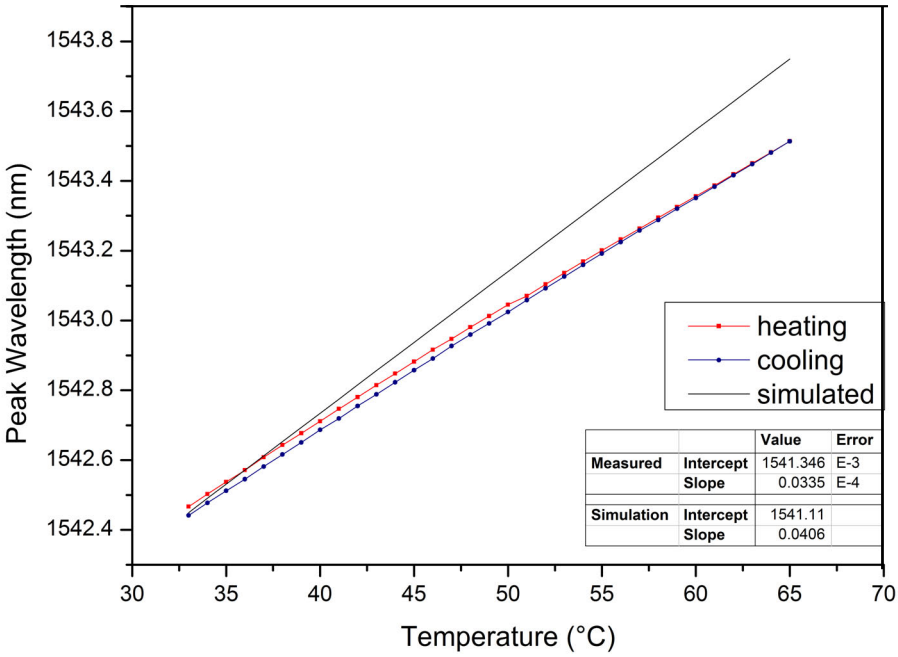

Figure B.2: Comparison between the experimental measurements and simulated results of the tuning of the fiber Bragg grating

Nomenclature

Abbreviation	Descriptions
AC	Alternative component
AO	Acousto-optic filter
AR	Antireflection coating
CW	Continuous wave
DBR	Distributed Bragg reflector
DC	Direct component
DCM	Dichloromethane
DFB	Distributed feedback
DMM	Digital multi-ammeter
ECDL	External cavity diode laser
EO	Electro-optic filter
ESA	Electronic spectrum Analyzer
FBG	Fiber Bragg grating
FC/APC	Fiber connectors/angle-polished connectors
FPA	Fabry-Perot Amplifier
FWHM	Full width at half maximum
GCSOA	Gain-Clamped SOAs
GEISA	Spectroscopic GEISA data bank
HITRAN	Spectroscopic databases HITRAN
HR	High reflection coating
HWHM	Half width at half maximum
ICLAS	Intracavity laser absorption spectroscopy
LDA	Laser Diode Amplifier
LED	Light-emitting diodes
LNA	Low noise amplifier
LOA	Linear Optical Amplifier
NF	Noise figure
NIR	Near infrared
NIST	NIST database
OSA	Optical spectrum analyzer
PIN	p-i-n doped
PNNL	PNNL spectroscopic database
RF	Radio frequency
RIN	Relative intensity noise
ROF	Relaxation of frequency
SLA	Semiconductor Laser Amplifier
SNR (S/N)	Signal to noise ratio
SOA	Semiconductor optical amplifier
TWA	Traveling wave amplifier
UV	Ultraviolet range
VC	Variable coupler
VCSEL	Vertical cavity surface emitting lasers

symbol	Descriptions
N, N_i	Number of atoms in excited states
ζ	The sensitivity enhancement factor
K_B	Boltzmann constant
ξ	Poisson ratio
A_{intra}	Intracavity absorbance
p_i, po, p_s	Pumping rates
γ	inverse lifetime
s_i	Photon number
κ_i	Loss per round trip
β	Propagation constant
t_1, t_2	Transmission amplitude at each facets
r_1, r_2	Reflection amplitude at each facets
γ_l, γ_D	Lorentzian and Doppler pressure coeff.
C_m	Mole fraction
γ_d	Damping factor
a_1, a_2	Intrinsic laser parameters
S_{sp}	Single side spectral density
$\Gamma(\nu)$	Line shape function
$H(\omega)$	Transfer function
$\sigma(\nu)$	Absorption cross section
$R(\nu)$	Relative intensity noise spectral density
$\rho(\tau)$	Autocorrelation function
$\alpha, \alpha_m, \alpha t$	Internal loss,mirror loss, total loss
p_{11}, p_{12}, p_e	The components of the strain-optic tensor
k	Complex propagation constant
q	Integer
pr	Gas pressure
κ_D	Peak Doppler cross section
B_{res}	The resolution bandwidth of ESA
η_{in}	Internal quantum efficiency
η_{det}	Detector efficiency
$I(x), I_o$	Light field intensities (Beer Lambert law)
I_1/I_2	The two modes intensity ratio
R, R_{load}	Impedance and load resistance
α_A, α_F	Thermal expansion coeff. of Aluminum and fiber

symbol	Descriptions
ν, ν_o, ω, f	Optical, resonance ,angular,linear frequencies
E, E_i, E_f	Energy states
h	Plank constant
j	Complex number $\sqrt{-1}$
λ, λ_B	The wavelength, Bragg wavelength
g, g_s, g_{th}	Laser gain, single pass gain,threshold gain
n, n_{eff}	Refractive index, effective refractive index
Γ	The confinement factor
$P_{in}, P_{out}, P(t), P_o, P_{avg}$	Inside,output,temporal, average optical powers
$I, I_{th}, I_{ph}, I_{det}$	Current,threshold current,photodiode,and-detector currents
e	Electron charge
L	Length
θ, ϕ	Phase shifts
c	Velocity of light
T	Temperature
W	Width
Λ	Grating period or pitch
m	Number of modes or number of species
i	Subscript
M	Molecular weight
B	Einstein coefficient
η_i	Loss per round trip
ϵ	Mode competition strength parameter
Q_i	Normalized photon number

Acknowledgements

During my stay here at the university of Kassel I interacted with many colleagues who contribute directly or indirectly to my thesis. I would like to thank all of them for their help.
In particular there are my advisor Prof. Dr. H. Hillmer. With the right combination of guidance and freedom you substantially contributed to the success of my work and I believe it was really productive time. I would like to thank all the members of reading committee. Thank you tacking the time for reading my thesis and providing me many helpful comments and suggestion.
Furthermore, I would like to thank "Nano-Nose" group. Discussion with you was always inspiring and helpful. Moreover, I would like to thank all member of the Institute of Nanostructure Technologies and Analytics (INA) for their sincere hospitality during my stay in Germany.
During my Ph.D. time I had the opportunity to contribute conferences inside Germany and visit other groups in UK. This was made possible by the supports from the Institute of Nanostructure Technologies and Analytics (INA) and from Prof. Dr. H. Hillmer.
Also, I would like thank the Egyptian Mission Department for their financial support during my Ph.D.. Finally, I would like to thank my family and all my friends for their supports and encouragements.

Publications

1. **M. Ahmad**, J. Sonksen, N. Storch, H. Krause, J. Shrestha, S. Blom, A. Pötzl, B. Khudhair, and H. Hillmer," Semiconductor laser based sensors for intelligently networking sensing systems" Seventh International Conference on Networked Sensing Systems(INSS2010) Kassel, Germany, Jun 2010, p. 101-106,. (ISBN 978-1-4244-7909-2).

2. Julian Sonksen, **Mahmoud Ahmad**, Nico Storch, Hubert Krause, Sven Blom, Alexander Potzl, Hartmut Hillmer," Controlling and Tuning the Emission of Semiconductor Optical Amplifier for Sensor Application by Means of Fiber Bragg Gratings" Proceedings of the 8th WSEAS International conference on Microelectronics, Nanoelectronics, Optoelectronics (MINO '09),59,2009.

3. H. Krause, J. Sonksen, **M. Ahmad**, V. Viereck, O. Mikami, and H. Hillmer, Aufbau eines faserbasierten Laserresonators mit zwei Fabry-Pérot Kavitäten und einer gemeinsamen aktiven Zone für Sensorikanwendungen, 109. DGaO Konferenz, B24+, 2008.

References

[1] Pauling, Robinson ; Cary: Quantitaive analysis of urin vapor and breath by gas liqiud chromatography. In: *Proc. Natl. Acad. Sci.* 68 (1971), S. 2374–2384 1

[2] Wang, Sahay: Breath Analysis Using Laser Spectroscopic Techniques: Breath Biomarkers, Spectral Fingerprints, and Detection Limits. In: *Sensors* 9 (2009), S. 8230–8262 1

[3] Buszewski, Ligor A. Kesy: Human exhaled air analytics: Biomarkers of diseases. In: *Biomed. chromatogr.: BMC* 21 (2007), S. 553–556 2

[4] Grote, Pawliszyn: Solid phase microextraction for the analysis of human breath. In: *Anal. Chem.* 69 (1997), S. 587–596 2

[5] Lord, Pawliszyn Segal: Breath analysis and monitoring by membrane extraction with sorbent interface. In: *Anal Chem* 74 (2002), S. 5650 2

[6] Moser, Eibl Lechner Rieder L. Bodrogi: Mass spectrometric profile of exhaled breath-field study by PTR-MS. In: *Respir. Physiol. Neurobiol* 145 (2005), S. 295–300 2

[7] Harrison, Mayhew T. Critchley: Real-time breath monitoring of propane and its volatile metabolites during surgery using a novel mass spectrometric technique a feasibility study. In: *Br. J. Anaesth.* 91 (2003), S. 797–799 2

[8] Yuan, Lord P. Mester: Automated in-tube solid phase microextraction coupled with liquid chromatography-electrospray ionization mass spectrometry for the determination of selected benzodiazepines. In: *J. Anal. Toxicol.* 24 (2000), S. 718–725 2

[9] Ruzsanyi, Litterst Westhoff F. Baumbach: Detection of human metabolites using multi-capillary columns coupled to ion mobility spectrometers. In: *J. Chromatogr. A* 1084 (2005), S. 145–151 2

[10] Turner, Smith Spanel: A longitudinal study of ammonia, acetone and propanol in the exhaled breath of 30 subjects using selected ion flow tube mass spectrometry SIFT-MS. In: *Physiol. Meas* 27 (2006), S. 321–337 2

[11] Smith, Spanel: Selected ion flow tube mass spectrometry (SIFT-MS) for on-line trace gas analysis. In: *Mass Spectrom. Rev.* 24 (2005), S. 661–700 2

[12] Natale, Amico Macagnano: Lung cancer identification by the analysis of breath by means of an array of non selective gas sensors. In: *Biosens Bioelectron* 18 (2003), S. 1209–1218 2

[13] Fleischer, Rumpel M. Simon: Detection of volatile compounds correlated to human diseases through breath analysis with chemical sensors. In: *Sens Actuat B* 83 (2002), S. 245–249 2

[14] Sigrist, Marinov Rey Vogler W. Bartlome: Trace gas monitoring with infrared laser-based detection schemes. In: *Appl. Phys. B: Lasers Opt.* 90 (2008), S. 289–300 2

[15] McCurdy, Wysocki Lewicki T. Bakhirkin: Recent advances of laser-spectroscopy-based techniques for applications in breath analysis. In: *J. Breath Res* 1 (2007), S. 1–12 2

[16] Keefe, Deacon: Cavity ring down optical spectrometer for absorption measurements using pulsed laser sources. In: *Rev Sci Instrum* 59 (1988), S. 2544–2551 2

[17] Berden, Meijer Peeters: Cavity ring down spectroscopy experimental schemes and applications. In: *Int Rev Phys Chem* 19 (2000), S. 596–607 2

[18] Mazurenka, Peverall R. OrrEwing: Cavity ring-down and cavity enhanced spectroscopy using diode lasers. In: *Annu. Rep. Prog. Chem. Sect. C. Phys. Chem.* 101 (2005), S. 100–142 2

[19] Hofstetter, Faist Nagele S. Beck: Photoacoustic spectroscopy with quantum cascade distributed feedback lasers. In: *Opt. Lett.* 26 (2001), S. 887–889 3

[20] Mihalcea, Hanson Baer: Tunable diode laser absorption measurements of NO_2 near 670 and 395 *nm*. In: *Appl. Opt.* 35 (1996), S. 4059–4064 3

[21] Sierks, Baev ; Toschek: Enhancement of the sensitivity of a multimode dye laser to intracavity absorption. In: *Optics Communications* 96 (1993), S. 81–86 3, 29

[22] Baev, Toschek Eschner: Intra cavity spectroscopy with diode lasers. In: *Appl. Phys. B.* 55 (1992), S. 463–477 3

[23] Brunner, Paul: Competition between selected and non-selected modes in a multimode laser. In: *Optics Communications* 24 (1978), S. 11–15 5, 36, 39

[24] Quist, Rediker ; Zeiger: In: *Appl. Phys. Lett.* 1 (1962), S. 91 8

[25] Ye, Cunyen: *Tunable External Cavity Diode Lasers*. London : World Scientific Publishing Co. Pte. Ltd., 2004 11

[26] Mroziewicz: External cavity wavelength tunable semiconductor lasers. In: *Opto-Electronics Rev.* 16(4) (2008), S. 347–366 15

[27] Hong, Shepard Rogers B. Kim ; Clements: Matrix-grating strongly gain-coupled (MG-SGC)DFB lasers with 4-nm continuous wavelength tuning range. In: *IEEE Photonic. Techn.* L11 (1999), S. 515–517 16

[28] Rigole, Baeckbom Stalnacke Berglind W. Nilsson ; Stoltz: Quasi-continuous tuning range from 1560 to 1520 nm in a GCSR laser, with high power and low tuning currents. In: *Electron. Lett.* 32 (1996), S. 2352–2345 16

[29] Tkach ; Chraplyvy: Regimes of feedback effects in 1.5μ m distributed feedback lasers. In: *J. Lightwave Technol.* LT-4 (1986), S. 1655–1661 18

[30] Henry: *Line broadening of semiconductor lasers*. New York : Y. Yamamoto (Ed) John Wiley and Sons. Inc., 1991 18

[31] Agrawal: Line narrowing in a single mode injection laser due to external optical feedback. In: *IEEE J. Quantum Electron.* QE-20 (1984), S. 468–471 18

[32] Petermann: External optical feedback phenomena in semiconductor lasers. In: *IEEE J. Sel. Top. Quantum Electron.* 1 (1995), S. 480–489 19

[33] Cohen ; Lenstra: Spectral properties of the coherence collapsed state of a semiconductor laser with delayed optical feedback. In: *IEEE J. Quantum Electron.* QE-25 (1989), S. 1143–1151 20

[34] Acket, Boef Lenstra ; Verbeek: The influence of feedback intensity on longitudinal mode properties and optical noise in index-guided semiconductor lasers. In: *IEEE J. Quantum Electron.* QE-20 (1984), S. 1163–1169 20

[35] Lenstra, Verbeek ; Boef: Coherence collapse in single-mode semiconductor lasers due to optical feedback. In: *IEEE J. Quantum Electron.* QE-21 (1985), S. 674–679 20

[36] Tittel, Richter ; Fried: Mid-Infrared Laser Applications in Spectroscopy. In: *Solid-State Mid-Infrared Laser Sources* 89 (2003), S. 448–529 21

[37] Rothman, Goldman Massie Edwards Flaud Perrin Camypeyret Dana Mandin Schroeder McCann Gamache Wattson Yoshino Chance Jucks Brown Nemtchinov V. Rinsland: The HITRAN 2008 molecularspectroscopic-database. In: *J. Quant. Spectrosc. Radiat. Transfer* 110 (2009), S. 533–572 23, 24

[38] Jacquinet-Husson, Ballard et a. Arie: The 1997 spectroscopic GEISA databank. In: *J. Quant. Spectrosc. Radiat. Transfer* 62 (1999), S. 205–254 24

[39] Humlicek: An efficient method of evaluation of the complex probability function: the Voigt function and its derivatives. In: *J. Quant. Spectrosc. Radiat. Transfer* 21 (1979), S. 305–309 25

[40] Scherer, Woellenstein Salzmann ; Weidemueller: Injection seeded single mode intra-cavity absorption spectroscopy. In: *Applied Physics B:Lasers and Optics* 33 (2009), S. 281–286 27

[41] Ovchinnikov, Evgency: *Influence of spectral and spatial inhomogeneities of the active medium on spectral dynamics of multimodes solid state lasers*, Hamburg university, Diss., 2003 28

[42] Toschek, Baev: One is not enough: intra-cavity spectroscopy with multimode lasers. In: *Optical Sciences* 54 (1987), S. 89–111 28

[43] Lacot, Romanini Stoeckel ; Kachanov: Spectrotemporal dynamics of a two-coupled-mode laser. In: *Physical Review A* 57 (1998), S. 4019–4025 28

[44] Hansch, Schawlow ; Toschek: Ultrasensitive response of a cw dye laser to selective extinction. In: *IEEE Journal of Quantum Electronics* 8 (1972), S. 802–804 29

[45] Boehm, Baev Stephani ; Toschek: Intracavity absorption spectroscopy with a Nd-doped fiber laser. In: *Opt. Lett.* 22 (1993), S. 1955–1957 29

[46] Hillmer, Hansmann: *Handbook of Lasers and Optics*. 695-726 : Springer Verlag, 2007 30

[47] Hillmer, H.: *Sensorvorrichtung und verfahren zur ermittlung einer physikalischen größe*. DE 102004037519 B4 Ep 000001771720 al, wo 002006012825 al patent, 2004 31

[48] Kallimani ; O'Mahony: Relative intensity noise for laser diodes with arbitrary amounts of optical feedback. In: *IEEE J. Quantum Electron.* 34 (1998), S. 1438–1446 31

[49] Petermann: *Laser Diode Modulation and Noise*. Boston, MA: Kluwer Academic, 1991 32, 34, 35

[50] Yamada: Theory of mode competition noise in semiconductor lasers. In: *IEEE J. Quantum Electron.* 22 (1986), S. 1052–1059 35

[51] Demtroeder, Wolfgang: *Laser Spectroscopy: Basic Concepts and Instrumentation*. Berlin : Springer-Verlag, 2003 37

[52] Ahmad, Storch Krause Shrestha Blom Pötzel K. Sonksen ; Hillmer: Semiconductor laser based sensors for intelligently networking sensing systems. In: *IEEE Technical Digest INSS2010* ISBN 978-1-4244-7910-8 (2010), S. 101–106 44

[53] Connelly: Wideband Semiconductor Optical Amplifier Steady-State Numerical Model. In: *IEEE J. Quantum Electron.* 37 (2001), S. 439–447 46, 88

[54] Ghafouri-Shiraz: *Fundamentals of Laser Diode Amplifiers*. Wiley, Chichester, 1996 46

[55] Boucher ; Sharaiha: Spectral properties of amplified spontaneous emission in semiconductor optical amplifiers. In: *IEEE J. Quantum Electron.* 36 (2000), S. 708–720 46

[56] Holtmann: Polarization Insensitive Semiconductor Optical Amplifiers in InGaAsP/InP for 1.3 nm Wavelengths Exploiting Bulk Ridge-Waveguide Structure. In: *Series in Quantum Electronics (ETH Diss. 12195), Hartung-Gorre* 2 (1997) 47

[57] Hamamoto, Holtmann Melchior Sudo Sasaki M. Gini ; Yamaguchi: Active multimode interferometer semiconductor optical amplifier. In: *Electron. Lett.* 36 (2000), S. 1218–1220 47

[58] Ma ; Nakano: Realization of all optical wavelength converter based on directionally coupled semiconductor optical amplifiers. In: *Technol. Lett.* 11 (1999), S. 188–190 47

[59] Bjoerlin ; Bowers: Noise figure of vertical cavity semiconductor optical amplifiers. In: *IEEE J. Quantum Electron.* 38 (2002), S. 61–66 47

[60] Piprek, Bjoerlin ; Bowers: Design and analysis of vertical-cavity semiconductor optical amplifiers. In: *IEEE J. Quantum Electron.* 37 (2001), S. 127–134 47

[61] Hill, Johnson Fujii ; Kawasaki: Photo-sensitivity in optical fiber waveguides: Application to reflection filter fabrication. In: *App. Phys. Lett.* 32 (1978), S. 647–649 47, 48

[62] Grattan ; Sun: Fiber sensor technology: an overview. In: *Sensors and Actuators* 82 (2000), S. 40–61 47

[63] Meltz, Morey ; Glen: Formation of Bragg gratings in optical fibers by a transverse holographic method. In: *Opt. Lett.* 14 (1998), S. 823–825 47

[64] Blair ; Cassidy: Wavelength Division multiplexed sensor Network using Bragg Fibre Reflection Gratings. In: *Elect. Lett.* 28 (1992), S. 1734–1735 48

[65] Giles: Lightwave Applications of fiber Bragg Gratings. In: *Journ. of Light. Tech.* 15 (1997), S. 1391–1404 48

[66] Koo ; Kersey: Bragg grating-based laser sensors systems with interferometric interrogation and wavelength division multiplexing. In: *Journ. of Light. Tech.* 13 (1995), S. 1243–1249 48

[67] Willians, Sugden Bennion ; Doran: Fibre dispersion compensation using a chirped in-fibre Bragg grating. In: *Elect. Lett.* 30 (1994), S. 985–987 48

[68] Willians, Sugden Bennion ; Doran: Recent progress in applications of in-fibre Bragg grating sensors. In: *Optics and Lasers in Engineering* 31 (1999), S. 297–324 48

[69] Kashyap: *Fiber Bragg Gratings*. Academic Press, 1999 49

[70] Mortimore: Fiber Loop Reflectors. In: *Journal of Lightwave Technology* 6 (1988), S. 1217–1224 50

[71] Sonksen, Julian: *Sensor Process and Device for Determining a physical value 'A proof of Concept'*, Kassel university, Diss., 2010 55, 68, 69, 73

[72] Shrestha, Jyoti: *Characterization of fiber based laser by means of relative intensity noise (RIN)*, Kassel university, Diplomarbeit, 2010 59

[73] Glenn, Hunter: In: *British J Anaesth* 56 (2003), S. 617–626 67

[74] Baker, Martin B. Gregerson: In: *Crit Care Med* 31 (2003), S. 787–792 67

[75] Krause, Hubert: *Entwicklung eines Gassensors auf Basis der Modenkonkurrenz bei Halbleiterlasern*, Kassel university, Diss., 2010 68

[76] Xiao Zhao, Janos F.: Simultaneous intracavity laser absorption spectroscopic and electrical measurements of bilayer lipid membranes. In: *J. Phys. Chem.* 90 (1986), S. 3886–3890 73

[77] Wang, Jian: *New strategies of diode laser absorption sensors.* 2001. – Report No. TSD 141- High Temperature Gasdynamics Laboratory 98

[78] Yu Lung, Han S.: Measurement of Thermal Expansion Using an In Fiber Bragg Grating Sensor. In: *Measurements Science and Technology* 9 (1998), S. 1543–1547 99